Faculty of Mathematics and
Computer Science

Sensitivity of Optimization in Transcranial Direct Current Stimulation to Electrode Modeling

Master's Thesis

Alexander Frank

Westfälische Wilhelms-Universität Münster

2022

Faculty of Mathematics and
Computer Science

Sensitivity of Optimization in Transcranial Direct Current Stimulation to Electrode Modeling

Master's thesis

for the degree of
Master of Science
in
Mathematics
at the
Westfälische Wilhelms-Universität Münster

by

Alexander Frank

Matric No.: 429766
E-mail: alexander.frank@wwu.de

1. Reviewer: Prof. Dr. Carsten Wolters
2. Reviewer: Prof. Dr. Benedikt Wirth

March 2022

Contents

Introduction

Transcranial direct current stimulation (tDCS) is a non-invasive brain stimulation technique, which modifies neural excitability by applying weak currents via two or more electrodes placed on the scalp (Nitsche and Paulus, 2000). It has been successfully used in the treatment of neurological and neuropsychiatric disorders such as epilepsy (Fregni et al., 2006), Parkinson disease (Boggio et al., 2006), depression (Boggio et al., 2007) and Alzheimer disease (Ferrucci et al., 2008). In order to overcome the limitations of conventional bipolar electrode montages, multichannel tDCS can be combined with algorithmic-based optimization approaches (Dmochowski et al., 2011).
To understand the effects of tDCS, it is necessary to consider the functionality of the brain. The brain mainly consists of neuronal tissue, which can basically be seen as a complex network of neurons. Neurons are electrically excitable cells that communicate among each other using electrochemical signaling. At each neuron the incoming information is given in form of postsynaptic potentials (PSP), which can be either excitatory or inhibitory. These potentials superimpose and if a threshold is exceeded, an action potential is triggered, which will then move towards the next neuron (Purves et al., 2004). The electric fields induced by tDCS in the brain are too weak to trigger action potentials, but may induce shifts in the membrane potential while stimulation and hence modify the intrinsic neuronal network activity (Karabanov et al., 2019).
Simply put, the question arising in tDCS is how to apply the current in order to achieve a desired effect in the brain. To answer this question one first has to understand the relation of applied current and electric field (the forward problem) and thereon, how to choose an optimal current. Therefore one needs a mathematical model of the involved processes. As usual, there is a trade-off between simplicity and accuracy of the model. The objective of this thesis is to investigate the effect of two different electrode models on the electric field and on the optimal electrode arrangements. The first model will be rich in detail, the so called complete electrode model, while the other one will be a simplistic point electrode model.
Therefore this thesis consists of two parts. The first chapter only deals with the forward problem. Understanding this problem is essential for further investigations. At the beginning of chapter 1 the partial differential equation (sec. 1.1) and the boundary conditions for each electrode model will be introduced (sec. 1.3). We will prove that with certain assumptions the potentials generated by both models converge to each other in the brain, when the electrodes decrease in size. Section 1.4 focuses on how to solve the boundary value problems numerically. Before we use these numerical solutions in the second chapter, we will try to compare them to analytical solutions. In section 1.5 we will therefore derive a series expression of the complete electrode model solution on a fairly simple domain. Afterwards, the different solutions are compared in order to reveal differences and similarities. The second chapter will deal with the optimization aspect, mainly with so called maximum intensity approaches, whose main goal is to generate as much intensity in the target area along some desired direction. With the results from chapter 1 we will be able to show that the optimal montages for both electrodes will also converge, if the electrode size decreases (or atleast there exists such a subsequence). The last section focuses on the numerical solutions again. Therein optimal current montages for different targets in the aforementioned simple domain and furthermore for a realistic head model are calculated.

1. The Forward Problem

This chapter deals with several aspects of the forward problem for transcranial direct current brain stimulation. As we have already mentioned in the introduction, neuronal activity is based on electric currents. Therefore we want to start with a brief look into the Maxwell's equations, a system of four coupled differential equations, which will allow us to model the electromagnetic effects.

1.1. Maxwell's Equations

Starting point are the macroscopic formulations of Maxwell's Equations, also known as Maxwell's equations in matter (cf. Nolting, 2001).

Definition 1 (Maxwell's Equations)**.** Let E be the electric field and B the magnetic field. Furthermore we denote the displacement field by D and the magnetizing field by H. Then Maxwell's equations can be stated as

$$\operatorname{div} D = \rho \tag{1.1}$$
$$\operatorname{div} B = 0 \tag{1.2}$$
$$\operatorname{rot} E = -\frac{\partial B}{\partial t} \tag{1.3}$$
$$\operatorname{rot} H = J + \frac{\partial D}{\partial t}. \tag{1.4}$$

Assuming that the tissue is linear dielectric and linear magnetic we can specify $D = \varepsilon E$ and $H = \mu B$ with ε, μ being electrical permittivity and magnetic permeability, respectively. In this thesis we will only focus on the special case of tDCS. If we ignore the ramping in and out at the beginning and at the end of a stimulation, the currents used will be constant, resulting in a static problem. Hence the time derivatives vanish and the problem simplifies. In other cases as e.g. tACS, where alternating currents are applied, one can use a quasi-static approximation if the used frequencies are low enough (Plonsey and Heppner, 1967). We can therefore replace (1.3) and (1.4) by

$$\operatorname{rot} E = 0 \tag{1.5}$$
$$\operatorname{rot} H = J \tag{1.6}$$

Thus E is a gradient field and we can express it by

$$E = -\nabla u.$$

Assuming that the tissue is linear conductive and that the current density caused by brain activity is negligible compared to the stimulation induced currents we get

$$J = \sigma E = -\sigma \nabla u, \tag{1.7}$$

where σ is the conductivity tensor of the tissue. Plugging (1.7) into (1.6) and noticing that the divergence of a curl is zero, yields

$$\operatorname{div}(\sigma \nabla u) = 0. \tag{1.8}$$

We have implicitly assumed that all fields and coefficients are sufficiently smooth and that the domain of E is simply connected. Equation (1.8) is the basis for our problem, as it describes the electrical potential in the head. Transcranial direct current stimulation tries to modulate this potential via the boundary conditions.

1.2. Mathematical Basics

We need to introduce some mathematical concepts in order to formulate the boundary conditions and give meaning to the PDE even in the case of non-smooth conductivities. This section is mainly based on Lions and Magenes (1972) and Rudin (1991), where most of the proofs can be found.

Let $\Omega \subseteq \mathbb{R}^n$ be an (non-empty) open subset. We denote the space of p-integrable functions on Ω by $L^p(\Omega)$ with the usual norm $\|\cdot\|_{L^p(\Omega)}$ and for $p = 2$ with the usual inner product $\langle \cdot, \cdot \rangle_{L^2(\Omega)}$. It is well known that $L^2(\Omega)$ is a Hilbert space. For $\alpha = (\alpha_1, \ldots, \alpha_n) \in \mathbb{N}_0^n$ we define

$$D^\alpha = \frac{\partial^{|\alpha|}}{\partial x_1^{\alpha_1} \ldots \partial x_n^{\alpha_n}} \quad \text{with} \quad |\alpha| = \alpha_1 + \cdots + \alpha_n.$$

Throughout this thesis, $0 < c < C$ will denote some generic constants that can change from one occasion to the next. We will denote the euclidean norm on $\mathbb{R}^n$ by $|x|$ or $\|x\|_2$ and other p-norms by $\|x\|_p$. The standard inner product is denoted $x \cdot y$.
The space of all infinetly differentiable functions on Ω with compact support is $\mathcal{D}(\Omega)$. Let $K \subset \Omega$ be a compact subset and denote $\mathcal{D}_K(\Omega) = \{\varphi \in \mathcal{D}(\Omega) : \operatorname{supp} \varphi \subseteq K\}$. We can define the seminorms

$$p_j(\varphi) = \max_{\substack{x \in K \\ |\alpha| \leq j}} |D^\alpha \varphi(x)|, \quad j \in \mathbb{N}_0.$$

With this system $D_K(\Omega)$ becomes a Fréchet-space. Let $(K_n)_n$ be an increasing sequence of compact sets in Ω with $\bigcup K_n = \Omega$. Then we have

$$\bigcup \mathcal{D}_{K_n}(\Omega) = \mathcal{D}(\Omega).$$

We provide $\mathcal{D}(\Omega)$ with the inductive limit topology. An explicit construction of this topology can be found in Rudin (1991). These definitions are independent of the choice of K_n. We'll denote the dual space of $\mathcal{D}(\Omega)$ by $\mathcal{D}'(\Omega)$ and call its elements distributions. For $T \in \mathcal{D}'(\Omega)$ we will write $\langle T, \varphi \rangle$ instead of $T(\varphi)$. Notice that we can identify $L^1_{\text{loc}}(\Omega)$, i.e. functions being integrable on compact subsets, with a subset of $\mathcal{D}'(\Omega)$ by $\varphi \mapsto \langle f, \varphi \rangle$ for $f \in L^1_{\text{loc}}(\Omega)$. We will mostly refer to weak differentiability, unless explicitly stated otherwise. Recall that if u, v are locally integrable, then v is the weak αth-derivative of u if

$$\int_\Omega u D^\alpha \varphi \, dx = (-1)^\alpha \int_\Omega v \varphi \, dx \qquad \forall \varphi \in \mathcal{D}(\Omega)$$

and we write $D^\alpha u = v$. This also gives rise to a definition of a distributional derivative by $\langle D^\alpha T, \varphi \rangle = (-1)^{|\alpha|} \langle T, D^\alpha \varphi \rangle$.
Let m be an integer ≥ 0. We define the Sobolev space $H^m(\Omega)$ of order m on Ω by

$$H^m(\Omega) = \{u \in L^1_{\text{loc}}(\Omega) \mid D^\alpha u \in L^2(\Omega) \; \forall |\alpha| \leq m\} \quad \text{with} \quad \|u\|^2_{H^m(\Omega)} = \sum_{|\alpha| \leq m} \|D^\alpha u\|^2_{L^2(\Omega)}. \tag{1.9}$$

Then $H^m(\Omega)$ is a Hilbert space with inner product

$$\langle u, v \rangle_{H^m(\Omega)} = \sum_{|\alpha| \leq m} \langle D^\alpha u, D^\alpha v \rangle_{L^2(\Omega)}.$$

It turns out that in the case of $\Omega = \mathbb{R}^n$ these spaces can also be defined via the Fourier transform $\mathcal{F} : L^1(\mathbb{R}^n) \to C_0(\mathbb{R}^n), u \mapsto \hat{u}$ defined by

$$\hat{u}(y) = (2\pi)^{-\frac{n}{2}} \int_{\mathbb{R}^n} u(x) e^{-ix\cdot y}\, dx.$$

This mapping is linear and bounded.
A function $u \in C^\infty(\mathbb{R}^n)$ is rapidly decreasing, if for all $\alpha, \beta \in \mathbb{N}_0^n$

$$p_{\alpha,\beta}(f) = \sup_{x\in\mathbb{R}^n} |x^\alpha D^\beta f(x)| < \infty, \quad \text{where} \quad x^\alpha = x_1^{\alpha_1} \dots x_n^{\alpha_n}.$$

We denote the space of all rapidly decreasing functions by $\mathcal{S}_n$. It is also known as the Schwartz space. Together with the collection of norms it forms a Fréchet-space. One can show that

$$\mathcal{F}(\mathcal{D}^\alpha \varphi) = (iy)^\alpha \mathcal{F}\varphi \quad \text{and} \quad D^\beta \mathcal{F}\varphi = \mathcal{F}((-ix)^\beta \varphi) \quad \forall \varphi \in \mathcal{S}_n. \tag{1.10}$$

Furthermore the Fourier transform is a continuous, linear, bijective mapping of $\mathcal{S}_n$ onto $\mathcal{S}_n$. If we define $\tilde{u}(x) = u(-x)$, then the continuous inverse is given by $\mathcal{F}^{-1}\varphi = \tilde{\mathcal{F}}\varphi$. Since $\mathcal{S}_n$ is dense in $L^2(\mathbb{R}^n)$ and $\mathcal{F}$ is isometric with respect to the L^2-norm, we can extend the Fourier transform uniquely and obtain an isometric isomorphism $\mathcal{F} : L^2(\mathbb{R}^n) \to L^2(\mathbb{R}^n)$, which we will also call Fourier transform. Let us denote the dual of $\mathcal{S}_n$ by $\mathcal{S}_n'$. Its elements are called tempered distributions. Indeed, one can show that $\mathcal{D}(\mathbb{R}^n) \hookrightarrow \mathcal{S}_n$ is continuous with dense image. Therefore elements of $\mathcal{S}_n'$ are unique continuous extensions of elements in $\mathcal{D}'(\mathbb{R}^n)$ and we can identify $\mathcal{S}_n'$ with a subspace of $\mathcal{D}'(\mathbb{R}^n)$.
By transposition we define the Fourier transform of tempered distributions $\mathcal{F} : \mathcal{S}_n' \to \mathcal{S}_n'$

$$\langle \mathcal{F}u, \varphi\rangle = \langle u, \mathcal{F}\varphi\rangle \quad \forall \varphi \in \mathcal{S}_n.$$

This map is also linear, continuous and bijective with its inverse given by transposition of $\mathcal{F}^{-1} : \mathcal{S}_n \to \mathcal{S}_n$. Note that the properties (1.10) hold true for tempered distributions. One can now show

$$H^m(\mathbb{R}^n) = \{u \in \mathcal{S}_n' : (1 + |y|^2)^{\frac{m}{2}} \mathcal{F}u \in L^2(\mathbb{R}^n)\}$$

and that the norm in (1.9) is equivalent to

$$|||u|||_{H^m(\mathbb{R}^n)} = \|(1 + |y|^2)^{\frac{m}{2}} \mathcal{F}u\|_{L^2(\mathbb{R}^n)}.$$

The inner product is given by

$$\langle u, v\rangle = \int_{\mathbb{R}^n} \hat{u}(y)\overline{\hat{v}(y)}(1 + |y|^2)^m\, dy.$$

We see that we can extend our definition of Sobolev spaces on $\mathbb{R}^n$ to real orders s. These spaces are again Hilbert spaces. One can show that $(H^s(\mathbb{R}^n))' = H^{-s}(\mathbb{R}^n)$ with dual pairing

$$\langle u, v\rangle = \int_{\mathbb{R}^n} \hat{u}\hat{v}\, dx.$$

The space $\mathcal{D}(\mathbb{R}^n)$ is dense in $H^s(\mathbb{R}^n)$ for $s \in \mathbb{R}$ (Wloka, 1987, Thm. 5.1).
For $s \geq 0$ we define the space $H^s(\Omega)$ as the restrictions of functions in $H^s(\mathbb{R}^n)$ to Ω, together with the norm

$$|||u|||_{H^s(\Omega)} = \inf \|U\|_{H^s(\mathbb{R}^n)}, \quad U = u \quad \text{a.e. on } \Omega. \tag{1.11}$$

There are other common definitions in the literature, which are equivalent if Ω has a Lipschitz boundary. In this case the new definition is also consistent with the one given earlier for integer orders. We will always assume that Ω has at least a Lipschitz boundary. We refer to Grisvard (1985, 1.3 & 1.4) for more information. Notice we will give a precise definition of the regularity

of a boundary later.
It follows that $\mathcal{D}(\bar{\Omega})$ is dense in $H^s(\Omega)$, where $\mathcal{D}(\bar{\Omega})$ are the restrictions of $\mathcal{D}(\mathbb{R}^n)$ to Ω (Wloka, 1987, Lemma 5.1). Furthermore we define $H_0^s(\Omega) = \overline{\mathcal{D}(\Omega)}^{H^s}$ and $H^{-s}(\Omega) = (H_0^s(\Omega))'$.
In later sections we will use results from Lions and Magenes (1972). In order to study boundary value problems in $H^s(\Omega)$ for arbitrary $s \in \mathbb{R}$, they impose strong regularity conditions on Ω and the boundary Γ. As they mention in remark 8.2, the hypothesis could be specified for each s separately. We won't further investigate this and impose these strong conditions in the relevant sections. Also notice that they define the spaces $H^s(\Omega)$ by using interpolation theory, but if Ω is sufficient regular, this definition is equivalent to the definition above.
We denote the Hölder spaces by $C^{k,l}(\Omega)$ and define $C^{k,0}(\Omega) = C^k(\Omega)$. From now on we'll always assume that Ω is bounded and denote it's boundary by Γ. We call a bounded set a domain if it is open, non-empty and connected. Following Grisvard (1985) we say that the boundary Γ is of class $C^{k,l}$, if for every $x \in \Gamma$ there exists a neighborhood V of x in $\mathbb{R}^n$ and new orthogonal coordinates $\{y_1, \dots, y_n\}$ such that

1. V is a hypercube in the new coordinates $V = \{(y_1, \dots, y_n) : |y_i| < a_i,\ i = 1, \dots, n\}$
2. there exists $\varphi \in C^{k,l}(V')$ with $V' = \{y' = (y_1, \dots, y_{n-1}) : |y_i| < a_i,\ i = 1, \dots, n-1\}$ such that
   a) $|\varphi(y')| \leq \frac{a_n}{2}\ \forall y' \in V'$
   b) $\Omega \cap V = \{y = (y', y_n) \in V : y_n < \varphi(y')\}$
   c) $\Gamma \cap V = \{y = (y', y_n) \in V : y_n = \varphi(y')\}$.

.

Lions and Magenes (1972) consider a different object: We say that $\bar{\Omega}$ is an n-dimensional submanifold of class $C^{k,l}$ with boundary in $\mathbb{R}^n$, if for every $x \in \Gamma$ there exists a neighborhood V of x in $\mathbb{R}^n$ and a mapping $\psi : V \to \psi(V) \subset \mathbb{R}^n$ such that

1. ψ is bijective
2. ψ and ψ^{-1} are of class $C^{k,l}$
3. $\Omega \cap V = \{y \in \Omega : \psi_n(y) < 0\}$

This implies that the boundary is of class $C^{k,l}$, according to the definition above. The converse is only true for $k \geq 1$, which follows from the implicit function theorem (cf. Grisvard, 1985; Wloka, 1987). Lions and Magenes (1972) require that Γ is infinitely differentiable, therefore it is irrelevant which one we choose. When we speak of Lipschitz domains we refer to a domain with a Lipschitz boundary.
Following Lions and Magenes (1972) we next define the spaces $H^s(\Gamma)$ for real s, when Γ is infinitely smooth. Let $\{O_1, \dots, O_k\}$ be a family of open bounded subsets of $\mathbb{R}^n$ covering Γ, such that for each $j = 1, \dots, k$ there exists an infinitely differentiable map

$$O_j \to W = \{(y', y_n) \in \mathbb{R}^n : |y'| < 1, |y_n| < 1\} \quad x \mapsto \varphi_j(x) = y,$$

such that φ_j has an infinitely differentiable inverse and satisfies

$$\varphi_j(O_j \cap \Omega) = W \cap \{y_n > 0\}, \quad \varphi_j(O_j \cap \Gamma) = W \cap \{y_n = 0\}, \quad \varphi_j(O_j \cap \Omega^c) = W \cap \{y_n > 0\}.$$

Basically this is a composition of an orthogonal coordinate transformation and φ from the above definition (together with a scaling). If we would assume less regularity on Γ, the functions φ_j would be less regular. Furthermore we assume that if $O_j \cap O_i \neq \emptyset$, then there exists an infinitely differentiable homeomorphism $\phi_{i,j} : \varphi_i(O_j \cap O_i) \to \varphi_j(O_j \cap O_i)$ with positive jacobian and

$\varphi_j(x) = \phi_{i,j}(\varphi_i(x))$ for $x \in O_m \cap O_i$. Let $\{\alpha_j\}$ be a partition of unity on Γ subordinate to $O_j \cap \Gamma$, i.e.

$$\alpha_j \in \mathcal{D}(\Gamma), \quad \alpha_j \text{ compact support in } O_j \cap \Gamma, \quad \sum_{j=1}^{k} \alpha_j = 1 \text{ on } \Gamma.$$

The space $\mathcal{D}(\Gamma)$ consists of restrictions of smooth functions to Γ. Now if u is a function on Γ we can decompose $u = \sum_{j=1}^{k}(\alpha_j u)$ and define functions $\varphi_j^*(\alpha_j u)$ by

$$\varphi_j^*(\alpha_j u)(y', 0) = (\alpha_j u)(\varphi^{-1}(y', 0)), \quad y \in W \cap \{y_n = 0\}.$$

Since α_j has compact support in $\Gamma \cap O_j$, the function $\varphi_m^*(\alpha_j u)$ has compact support in $W \cap \{y_n = 0\}$. We can therefore consider $\varphi_j^*(\alpha_j u)$ to be defined on $\mathbb{R}^{n-1}$, by extending it by 0. One can show that $u \mapsto \varphi_j^*(\alpha_j u)$ is a continuous mapping for $L^1(\Gamma) \to L^1(\mathbb{R}^{n-1})$, $\mathcal{D}(\Gamma) \to \mathcal{D}(\mathbb{R}^{n-1})$ and extends by continuity to a continuous linear mapping $\mathcal{D}'(\Gamma) \to \mathcal{D}'(\mathbb{R}^{n-1})$. We can finally define

$$H^s(\Gamma) = \{u \in \mathcal{D}'(\Gamma) : \varphi_j^*(\alpha_j u) \in H^s(\mathbb{R}^{n-1}) \ \forall j = 1 \dots k\}.$$

As $u \mapsto \psi u$ is a continuous linear mapping for $\psi \in \mathcal{D}(\mathbb{R}^n)$ from $H^s(\mathbb{R}^n)$ into itself, the definition of $H^s(\Gamma)$ is independent of the choice of local maps and partition of unity. Additionally we define the norm

$$\|u\|^2_{H^s(\Gamma)} = \sum_{j=1}^{k} \|\varphi_j^*(\alpha_j u)\|^2_{H^s(\mathbb{R}^{n-1})}$$

which of course depends on the choice made. A different choice of local maps and partition of unity yields an equivalent norm. Note that $H^s(\Gamma)$ is a Hilbert space. For $s \geq 0$ the space $\mathcal{D}(\Gamma)$ is dense in $H^s(\Gamma)$ and it holds $(H^s(\Gamma))' = H^{-s}(\Gamma)$. Denote the unit outward normal ν. Since $\mathcal{D}(\bar{\Omega})$ is dense in $H^s(\Omega)$ one can prove that

$$u \mapsto \left\{ \frac{\partial^j u}{\partial \nu^j} : j = 0 \dots \mu \right\}$$

extends by continuity from $\mathcal{D}(\bar{\Omega}) \to (\mathcal{D}(\Gamma))^\mu$ to a continuous linear mapping

$$H^s(\Omega) \to \prod_{j=0}^{\mu} H^{s-j-\frac{1}{2}}(\Gamma)$$

where μ is the greatest integer such that $\mu < s - \frac{1}{2}$. This map is surjective and has a continuous right inverse. As mentioned earlier we can prove weaker results with weaker assumptions. For a Lipschitz boundary one can also define the linear bounded surjective map $\gamma_0 : H^1(\Omega) \to H^{\frac{1}{2}}(\Gamma)$, which is uniquely determined by $\gamma_0 u = u|_\Gamma$ for $u \in C^{0,1}(\bar{\Omega})$, see e.g. Grisvard (1985, Thm. 1.5.1.2) or Wloka (1987, Thm. 8.7 & 8.8) . Note that we can also derive a trace theorem for negative order Sobolev Spaces by density arguments (cf. Lions and Magenes, 1972, Thm. 6.5) Let $v \in L^1_{\text{loc}}(\Omega)^n$ and $g \in L^1_{\text{loc}}(\Omega)$. Then g is the weak divergence of v if

$$\int_\Omega g\varphi \, dx = -\int_\Omega v \cdot \nabla\varphi \, dx \quad \forall \varphi \in \mathcal{D}(\Omega).$$

We write $\operatorname{div} v = g$. Further we define the space

$$H(\operatorname{div}; \Omega) = \{v \in L^2(\Omega)^3 : \operatorname{div} v \in L^2(\Omega)\} \quad \text{with} \quad \|v\|^2_{H(\operatorname{div};\Omega)} = \|v\|^2_{L^2(\Omega)} + \|\operatorname{div} v\|^2_{L^2(\Omega)}. \tag{1.12}$$

This is a Hilbert space. When Ω has a Lipschitz boundary, the space $\mathcal{D}(\bar{\Omega})^n$ is dense in $H(\operatorname{div}, \Omega)$. Therefore one can show that the mapping $\tilde{\gamma} : v \mapsto v \cdot \nu$ defined on $\mathcal{D}(\bar{\Omega})^n$ can be extended to a linear continuous mapping $\tilde{\gamma} : H(\operatorname{div}; \Omega) \to H^{-\frac{1}{2}}(\Gamma)$ (Girault and Raviart, 1986, Thm. 2.4

& 2.5). Usually we will write $v \cdot \nu$ instead of $\tilde{\gamma} v$. Note that $H^{\frac{1}{2}}(\Gamma)$ can be constructed similar in the case of Ω only having a Lipschitz boundary (Wloka, 1987). With these results one can extend Green's formula (Girault and Raviart, 1986, (2.17)) to

$$\int_\Omega v \cdot \nabla \phi \, dx + \int_\Omega \operatorname{div} v \, \phi \, dx = \langle v \cdot \nu, \phi \rangle_{H^{-\frac{1}{2}}(\Gamma) \times H^{\frac{1}{2}}(\Gamma)} \quad \forall v \in H(\operatorname{div}; \Omega),\ \phi \in H^1(\Omega). \tag{1.13}$$

So far we considered complex valued functions and distributions. Since we will assume that the conductivity σ and the applied current are real valued and the PDE is linear, we can always construct real solutions from complex solutions and their complex conjugates. Further the solutions will be unique, meaning that they will be real anyway. Hence we can restrict ourselves to the subspaces of real valued functions resp. distributions. It is reasonable to define real valued tempered distributions as tempered distributions, which take real values on real Schwartz functions. With $\mathcal{F}u(y) = \overline{\mathcal{F}u(-y)}$ (for real functions and distributions) one can show that the resulting spaces are real Hilbert spaces.
We will need two further theorems that we will often use:
The first one is the lemma of Lax-Milgram. Let V be a real Hilbert space and $a : V \times V \to \mathbb{R}$ bilinear, coercive and bounded, i.e.

$$|a(u, v)| \leq C \|u\| \, \|v\| \quad \text{and} \quad c\|v\|^2 \leq a(v, v) \quad \forall v, u \in V.$$

Further assume that $l : V \to \mathbb{R}$ is linear and bounded. Then the problem

$$\text{Find } u \in V \text{ with } a(u, v) = l(v) \quad \forall v \in V$$

has a unique solution $u \in V$ (Girault and Raviart, 1986, Thm 1.7). Note that a similar version holds for complex Hilbert spaces (Yosida, 1995, Section 3.7).
In order to prove coercivity we will use the Poincaré inequality. Let Ω be a Lipschitz domain and $E \subseteq \Omega$ have positive measure. We denote

$$u_E = \frac{1}{|E|} \int_E u \, dx.$$

Then there exists $C > 0$, only depending on Ω and E, such that for all $u \in H^1(\Omega)$

$$\int_\Omega |u - u_E|^2 \, dx \leq C \int_\Omega |\nabla u|^2 \, dx. \tag{1.14}$$

A proof can be found in Leoni (2009, Thm. 12.23).

1.3. The Boundary Value Problem

Although there are different electrode models, we will mainly focus on on very simplistic one, the point electrode model, and a very detailed one, the complete electrode model. Together with the PDE (1.8) from section 1.1

$$\operatorname{div} \sigma \nabla u = 0 \quad \text{on } \Omega, \tag{1.15}$$

they each form a boundary value problem. We want to impose only weak regularity conditions on σ. Therefore we can't understand this equation in the classical sense, at most in the weak sense of (1.12). From now on we will assume that $\Omega \subset \mathbb{R}^3$ is a Lipschitz domain.
In transcranial direct current stimulation the user controls the current (resp. current density) applied to the skin. Therefore it is natural to define the boundary conditions of the problem as

$$\sigma \nabla u \cdot \nu = f \quad \text{on } \Gamma. \tag{1.16}$$

We assume that the conductivity tensor is bounded, i.e. $\sigma \in L^\infty(\Omega, \mathbb{R}^{3\times 3})$, and that $\sigma(x)$ is symmetric positive definite for $x \in \Omega$. Furthermore assume there exists $c > 0$ with $\xi^T \sigma(x)\xi \geq c|\xi|^2$ for all $x \in \Omega$ and $\xi \in \mathbb{R}^3$, or short $\sigma(x) \geq c \; \forall x \in \Omega$.
So far we didn't specify f yet. We will start with a model that would probably best be described as a continuum model, as one can control the current injection in every point on the skin. We could assume e.g. $f \in L^2(\Gamma)$ with $\int_\Gamma f \, d\mathcal{H}^2 = 0$, where $\mathcal{H}^2$ is the 2-dimensional Hausdorff measure, but we will start with a more general case.

Definition 2. Define $H_\diamond^{-\frac{1}{2}}(\Gamma) = \{g \in H^{-\frac{1}{2}}(\Gamma) : \langle g, 1\rangle = 0\}$. These are the permissible current injections.

Assume $f \in H_\diamond^{-\frac{1}{2}}(\Gamma)$. If $u \in H^1(\Omega)$ and $\operatorname{div} \sigma\nabla u = 0$, we can use Green's formula (1.13) and get

$$\int_\Omega \operatorname{div}(\sigma\nabla u) v \, dx + \int_\Omega \sigma\nabla u \cdot \nabla v \, dx = \langle \sigma\nabla u \cdot \nu, v\rangle_{H^{-\frac{1}{2}}(\Gamma)\times H^{\frac{1}{2}}(\Gamma)} \tag{1.17}$$

for $v \in H^1(\Omega)$. From (1.15) and (1.16) we therefore derive

$$\int_\Omega \sigma\nabla u \cdot \nabla v \, dx = \langle f, v\rangle_{H^{-\frac{1}{2}}(\Gamma)\times H^{\frac{1}{2}}(\Gamma)} \quad \forall v \in H^1(\Omega). \tag{1.18}$$

If (1.18) holds, we can choose $v \in \mathcal{D}(\Omega)$, thus yielding $\operatorname{div} \sigma\nabla u = 0$ in the weak sense and with equation (1.17) we obtain $f = \sigma\nabla u \cdot \nu$.

Problem 3. For $f \in H_\diamond^{-\frac{1}{2}}(\Gamma)$ the weak formulation of the continuum model (CM) forward problem is given by:

$$\text{Find } u \in H^1(\Omega) \text{ with } \int_\Omega \sigma\nabla u \cdot \nabla v \, dx = \langle f, v\rangle_{H^{-\frac{1}{2}}(\Gamma)\times H^{\frac{1}{2}}(\Gamma)} \quad \forall v \in H^1(\Omega).$$

Lemma 4. The bilinear form $a : H^1(\Omega)/\mathbb{R} \times H^1(\Omega)/\mathbb{R} \to \mathbb{R}$ defined by

$$a(u, v) = \int_\Omega \sigma\nabla u \cdot \nabla v \, dx$$

is bilinear, bounded and coercive, i.e. it exists $c > 0$ with $a(v, v) \geq c\|v\|^2_{H^1(\Omega)/\mathbb{R}}$.

It is well known that if H is a Banach space and $V \subseteq H$ is a closed subspace, then the quotient space is a Banach space with the usual quotient norm. Furthermore if H is a Hilbert space, then so is H/V.

Proof. Obviously a is well defined and bilinear. Let $u, v \in H^1(\Omega)/\mathbb{R}$. It follows

$$|a(u, v)| \leq \int_\Omega |\sigma\nabla u \cdot \nabla v| \, dx \leq \int_\Omega \|\sigma\|_\infty |\nabla u||\nabla v| \, dx \leq \|\sigma\|_\infty \|u - c_1\|_{H^1(\Omega)} \|v - c_2\|_{H^1(\Omega)},$$

for $c_1, c_2 \in \mathbb{R}$, where we used the Cauchy-Schwarz and Hölder inequality. Hence $|a(u, v)| \leq C\|u\|_{H^1(\Omega)/\mathbb{R}}\|v\|_{H^1(\Omega)/\mathbb{R}}$. Furthermore using the Poincaré inequality we get

$$a(v, v) = \int_\Omega \sigma\nabla v \cdot \nabla v \, dx \geq \int_\Omega c|\nabla v|^2 \, dx \geq c\|v\|^2_{H^1(\Omega)/\mathbb{R}}. \tag{1.19}$$

□

Notice that the condition $\langle g, 1\rangle_{H^{-\frac{1}{2}}(\Gamma)\times H^{\frac{1}{2}}(\Gamma)} = 0$ implies, that g is well defined and continuous on $H^1(\Gamma)/\mathbb{R}$. Therefore we can apply the lemma of Lax-Milgram and conclude:

Theorem 5. For $f \in H^{-\frac{1}{2}} \diamond (\Gamma)$ problem 3 has a unique solution $u \in H^1(\Omega)/\mathbb{R}$, meaning that the solution in $H^1(\Omega)$ is only unique up to an additive constant. Furthermore there is $C > 0$ with $\|u\|_{H^1(\Omega)/\mathbb{R}} \leq C\|f\|_{H^{-\frac{1}{2}}(\Gamma)}$.

Proof. Only the inequality remains to be proven. This easily follows from (1.19) and the trace theorem, since for $\tilde{c} \in \mathbb{R}$

$$c\|u\|^2_{H^1(\Omega)/\mathbb{R}} \leq a(u,u) = \langle f, u\rangle = \langle f, u - \tilde{c}\rangle \leq \|f\|_{H^{-\frac{1}{2}}(\Gamma)}\|u - \tilde{c}\|_{H^{\frac{1}{2}}(\Gamma)} \leq C\|u - \tilde{c}\|_{H^1(\Omega)}.$$

□

The fact that the bilinearform is only coercive on the quotient space emphasizes that the electromagnetic potential is only unique up to the choice of the ground level, i.e. up to an additive constant.
Even tough the continuum model is good to handle mathematically, it is unrealistic as one cannot control the current at every point on the head but only through electrodes.

1.3.1. Point Electrode Model

When using small electrodes, a naive approach is to model them as having an infinitesimal small surface, meaning that they are only points. In order to still let current flow through the electrodes, we have to interpret the injected currents, or to be more precise, the current density, as delta distributions. We assume that Ω has a smooth boundary. Let there be L electrodes, denoted by $x_m \in \Gamma$, $m = 1, \ldots, L$. The corresponding delta distributions are denoted δ_{x_m}. Then we define

$$f = \sum_{m=1}^{L} I_m \delta_{x_m}.$$

Similar to problem 3 we assume $I = (I_1, \ldots, I_L) \in \mathbb{R}^L_\diamond$.

Definition 6. The elements of $\mathbb{R}^L_\diamond = \left\{ I \in \mathbb{R}^L : \sum_{m=1}^{L} I_m = 0 \right\}$ are called current patterns.

Since f is very singular, $v \in H^{\frac{1}{2}}(\Gamma)$ isn't enough for $f(v)$ to be well defined. As $\Omega \subset \mathbb{R}^3$, we only have $f \in H^{-(1+\varepsilon)}(\Gamma)$ for $\varepsilon > 0$, i.e. we require $v \in H^{(1+\varepsilon)}(\Gamma)$.
In this section we want to impose stronger conditions on σ near the boundary. This is necessary because of the strong irregularity of the boundary condition. We assume there exists a compact set $K \subset \Omega$ such that σ is smooth on $\bar{\Omega} \setminus K^\circ$. Therefore we can decompose the conductivity $\sigma = \sigma_{\mathrm{s}}\chi_{\bar{\Omega}\setminus K} + \sigma_{\mathrm{ns}}\chi_K$ into a smooth part $\sigma_{\mathrm{s}} \in C^\infty(\bar{\Omega}, \mathbb{R}^{3\times 3})$ and a possibly non-smooth part $\sigma_{\mathrm{ns}} \in L^\infty(\Omega, \mathbb{R}^{3\times 3})$. We define $H^s_\diamond(\Gamma)$ for $s \in \mathbb{R}$ similar to the case of $s = -\frac{1}{2}$. Furthermore we denote

$$H^1_{\mathrm{loc}}(\Omega) = \{v \in \mathcal{D}'(\Omega) : v|_U \in H^1(U) \text{ for every open } U \text{ with } \bar{U} \subset \Omega\}.$$

We'll write $U \Subset \Omega$, if U is open and $\bar{U} \subset \Omega$. Now if $u \notin H^1(\Omega)$, then either ∇u does not exist or $\nabla u \notin L^2(\Omega)$ and we can't interpret $\operatorname{div}\sigma\nabla u = 0$ in the weak sense. But if $u \in H^1_{\mathrm{loc}}(\Omega)$, then for $\varphi \in \mathcal{D}(\Omega)$ we can consider

$$\int_\Omega \sigma\nabla u \cdot \nabla\varphi \, dx$$

and therefore interpret $\operatorname{div}\sigma\nabla u = 0$ in the distributional sense and the boundary condition in the appropriate trace sense.

Problem 7. For $f = \sum I_m \delta_m$ with $I \in \mathbb{R}^k_\diamond$ the distributional formulation of the point electrode model (PEM) forward problem is given by

$$\text{Find } u \in H^{\frac{1}{2}-\varepsilon}(\Omega) \cap H^1_{\text{loc}}(\Omega) \text{ with } \int_\Omega \sigma \nabla u \cdot \nabla \varphi \, dx = 0 \quad \forall \varphi \in \mathcal{D}(\Omega) \tag{1.20}$$

$$\text{and } \sigma \nabla u \cdot \nu = f \text{ in the trace sense in } H^{-(1+\varepsilon)}(\Gamma). \tag{1.21}$$

In section 1.2 we stated that one can extend the operator, which takes the normal jth-order derivative on Γ to negative order Sobolev spaces. The same is true for more general boundary operators with smooth coefficients under additional assumptions. We refer to Lions and Magenes (1972, Ch. 2 Sec. 1.4 & 6.5). Since σ is smooth near the boundary we can therefore define the needed trace operator for (1.21).

Theorem 8. For $f \in H^s_\diamond(\Gamma)$ there exists a unique solution $u \in (H^{\min\{1,s+\frac{3}{2}\}}(\Omega) \cap H^1_{\text{loc}}(\Omega))/\mathbb{R}$ solving $\operatorname{div} \sigma \nabla u = 0$ on Ω and $\sigma \nabla u \cdot \nu = f$ on Γ in the above sense. Moreover there is $C > 0$ with $\|u\|_{H^{\min\{1,s+\frac{3}{2}\}}(\Omega)/\mathbb{R}} \leq C \|f\|_{H^s(\Gamma)}$.

The proof is based on Hanke et al. (2011b), where the statement is proven for the two dimensional unit disc and σ equal to 1 near the boundary. We will abbreviate $\mathcal{W}^s(\Omega) = H^{\min\{1,s+\frac{3}{2}\}}(\Omega) \cap H^1_{\text{loc}}(\Omega)$. In order to prove the existence, we require the following lemma.

Lemma 9. Let $U, U_0 \subset \mathbb{R}^3$ be two bounded C^∞ domains with $U \Subset U_0$. Assume σ is smooth in $\bar{U_0}$ and that $v \in H^s(U_0)/\mathbb{R}$ solves $\operatorname{div} \sigma \nabla v = 0$ for $s \in \mathbb{R}$ in the sense of distributions. Then $\|v\|_{H^r(U)/\mathbb{R}} \leq C(r) \|v\|_{H^s(U_0)/\mathbb{R}}$ for $r \in \mathbb{R}$ and in particular we get $v|_U \in C^\infty(U)/\mathbb{R}$.

Proof. Basically the proof can be found in Hanke et al. (2011b, Lemma A.1.). Note, however, the statement is only shown for the two dimensional case with $\sigma = 1$, but since σ is smooth the proof follows analogously. □

Proof of theorem 8. According to Lions and Magenes (1972, Remark 7.2.) the problem $\operatorname{div}(\sigma_{\text{s}} \nabla u) = 0$ on Ω, $\sigma_{\text{s}} \nabla u \cdot \nu = f$ on Γ has a unique solution $u_0 \in H^{s+\frac{3}{2}}(\Omega)/\mathbb{R}$ with

$$\|u_0\|_{H^{s+\frac{3}{2}}(\Omega)/\mathbb{R}} \leq C \|f\|_{H^s(\Gamma)}. \tag{1.22}$$

The previous lemma shows that u_0 is smooth on Ω and therefore $u_0 \in (H^{s+\frac{3}{2}}(\Omega) \cap H^1_{\text{loc}}(\Omega))/\mathbb{R}$. Recall that we could split the conductivity in a smooth and a non-smooth part $\sigma = \sigma_{\text{s}} \chi_{\bar{\Omega} \setminus K} + \sigma_{\text{ns}} \chi_K$. We choose two C^∞-domains $V \Subset V_0 \Subset \Omega$ with $K \subset V$ and a cut-off function $\varphi \in \mathcal{D}(V_0)$ with $\varphi|_V \equiv 1$. Let us consider the variational problem

$$\int_\Omega \sigma \nabla w \cdot \nabla v \, dx = \int_\Omega \sigma \nabla u_0 \cdot \nabla(\varphi v) \, dx \quad \text{for} \quad v \in H^1(\Omega)/\mathbb{R}. \tag{1.23}$$

We will show that this problem has a unique solution $w \in H^1(\Omega)/\mathbb{R}$ and that $u_0 - w$ is our desired solution. First define $a : H^1(\Omega)/\mathbb{R} \times H^1(\Omega)/\mathbb{R} \to \mathbb{R}$ and $l : H^1(\Omega)/\mathbb{R} \to \mathbb{R}$ by

$$a(w, v) = \int_\Omega \sigma \nabla w \cdot \nabla v \, dx \quad \text{and} \quad l(v) = \int_\Omega \sigma \nabla u_0 \cdot \nabla(\varphi v) \, dx.$$

Obviously a is bilinear, bounded and coercive as we showed in lemma 4. It's not directly clear why l should be well defined. Therefore consider $v \equiv 1$. Then

$$l(1) = \int_\Omega \sigma \nabla u_0 \cdot \nabla \varphi \, dx = \int_{V_0} \sigma \nabla u_0 \cdot \nabla \varphi \, dx = \int_{V_0 \setminus K} \sigma \nabla u_0 \cdot \nabla \varphi \, dx + \int_K \sigma \nabla u_0 \cdot \nabla \varphi \, dx.$$

Since $\varphi = 1$ on K, the second integral vanishes. Furthermore we have $\sigma = \sigma_s$ on $V_0 \setminus K$. This yields

$$l(1) = -\int_{V_0\setminus K} \operatorname{div}(\sigma_s \nabla u_0)\varphi \, dx + \int_{\partial V_0 \cup \partial K} \sigma_s \nabla u_0 \cdot \nu \varphi \, d\mathcal{H}^2.$$

The first integral drops out as u_0 is (locally) smooth and solves $\operatorname{div}(\sigma_s \nabla u) = 0$ on Ω in the distributional sense. Since $\varphi \in \mathcal{D}(V_0)$ and $\varphi|_V \equiv 1$ we obtain,

$$l(1) = \int_{\partial K} \sigma_s \nabla u_0 \cdot \nu \, d\mathcal{H}^2 = \int_K \operatorname{div}(\sigma_s \nabla u_0) \, dx = 0.$$

Therefore l is well defined on $H^1(\Omega)/\mathbb{R}$. Furthermore it is bounded in the quotient norm,

$$|l(v)| \leq \|\sigma \nabla (u_0 - c_1)\|_{L^2(V_0)} \|\nabla(\varphi(v - c_2))\|_{L^2(V_0)} \leq C \|u_0 - c_1\|_{H^1(V_0)} \|v - c_2\|_{H^1(V_0)}$$

for $c_1, c_2 \in \mathbb{R}$, where $C > 0$ is depended on Ω and φ. With (1.22) and lemma 9 we derive

$$|l(v)| \leq C \|f\|_{H^s(\Gamma)} \|v\|_{H^1(\Omega)/\mathbb{R}}.$$

Notice that l is independent of the choice of φ. Indeed, let φ_2 be a second function with similar properties and denote $\varphi_1 = \varphi$. With the same reasoning as above and (1.13) we obtain

$$\begin{aligned}\int_\Omega \sigma \nabla u_0 \cdot \nabla(\varphi_i v) \, dx &= \int_{V_0\setminus K} \sigma_s \nabla u_0 \cdot \nabla(\varphi_i v) \, dx + \int_K \sigma_{ns} \nabla u_0 \cdot \nabla(\varphi_i v) \, dx \\ &= -\int_{V_0\setminus K} \operatorname{div}(\sigma_s \nabla u_0)\varphi_i v \, dx + \int_{\partial K} \sigma_s \nabla u_0 \cdot \eta \varphi_i v \, d\mathcal{H}^2 + \int_K \sigma_{ns} \nabla u_0 \cdot \nabla(\varphi_i v) \, dx.\end{aligned}$$

The first integral vanishes and the second and third one are independent of φ_i as both functions are equal to 1 on V. Obviously l is linear. Hence we can apply the lemma of Lax-Milgram, which yields existence and uniqueness of a solution $w \in H^1(\Omega)/\mathbb{R}$ to the problem (1.23). We directly see

$$c\|w\|^2_{H^1(\Omega)} \leq a(w, w) = l(w) \leq C \|f\|_{H^s(\Gamma)} \|w\|_{H^1(\Omega)/\mathbb{R}}. \tag{1.24}$$

Since l is independent of φ, the same is true for w. We now want to show, that $u = u_0 - w$ is the desired solution. Therefore let $v \in \mathcal{D}(\Omega)$. Starting with the distributional derivative we deduce

$$\langle \operatorname{div}(\sigma \nabla w), v\rangle = -\int_\Omega \sigma \nabla w \cdot \nabla v \, dx = -\int_\Omega \sigma \nabla u_0 \cdot \nabla(\varphi v) \, dx = \int_\Omega \sigma \nabla u_0 \cdot \nabla \left[(1-\varphi)v\right] dx - \int_\Omega \sigma \nabla u_0 \cdot \nabla v \, dx.$$

The first integral vanishes since $\operatorname{supp}(1 - \varphi) \subseteq \Omega \setminus K$, $\sigma = \sigma_s$ on $\Omega \setminus K$, $(1 - \varphi)v \in \mathcal{D}(\Omega)$ and $\operatorname{div}(\sigma_s \nabla u_0) = 0$ on Ω in the distributional sense,

$$\int_{\Omega\setminus K} \sigma_s \nabla u_0 \cdot \nabla((1-\varphi)v) \, dx = \int_{\partial K \cup \partial\Omega} \sigma_s \nabla u_0 \cdot \nu(1-\varphi)v \, d\mathcal{H}^2 - \int_{\Omega\setminus K} \operatorname{div}(\sigma_s \nabla u_0)(1-\varphi)v \, dx = 0.$$

Thus we arrive at

$$\langle \operatorname{div}(\sigma \nabla w), v\rangle = \langle \operatorname{div}(\sigma \nabla u_0), v\rangle \quad \forall v \in \mathcal{D}(\Omega).$$

Notice that $\operatorname{div}(\sigma \nabla w) = \operatorname{div}(\sigma \nabla u_0)$ only in the distributional sense and not in the weak sense, as in general $\nabla u_0 \notin L^2(\Omega)$. By choosing test functions only supported away from K equation (1.23) yields $\operatorname{div}(\sigma \nabla w) = 0$ (a.e.) away from K. For $\psi \in C^\infty(\bar{\Omega})$ with $\operatorname{supp} \psi \subset \bar{\Omega} \setminus \bar{V}_0$ we get

$$0 = \int_{\Omega\setminus V_0} \operatorname{div}(\sigma \nabla w)\psi \, dx = \int_{\partial\Omega} \sigma \nabla w \cdot \nu \psi \, d\mathcal{H}^2 - \int_{\Omega\setminus V_0} \sigma \nabla w \cdot \nabla \psi \, dx.$$

The second integral vanishes since w solves (1.23) and the supports of φ and ψ are disjoint. Thus $\sigma \nabla w \cdot \nu = 0$ on Γ. Hence $u = u_0 - w$ is a solution of $\operatorname{div}(\sigma \nabla u) = 0$ on Ω, $\sigma \nabla u \cdot \nu = f$ on Γ, resp. in $H^s(\Gamma)$. Combining (1.22) and (1.24) we obtain

$$\|u\|_{\mathcal{H}^s(\Omega)/\mathbb{R}} \leq \|u_0\|_{\mathcal{H}^s(\Omega)/\mathbb{R}} + \|w\|_{\mathcal{H}^s(\Omega)/\mathbb{R}} \leq C\left(\|w\|_{H^1(\Omega)/\mathbb{R}} + \|u_0\|_{H^{s+\frac{3}{2}}(\Omega)/\mathbb{R}}\right) \leq C\|f\|_{H^s(\Gamma)}. \tag{1.25}$$

It remains to prove uniqueness. Assume $\tilde{u}$ is a second solution in $\mathcal{W}^s(\Omega)$. Then $h = u - \tilde{u} \in \mathcal{W}^s(\Omega)$ is a solution of $\operatorname{div}(\sigma\nabla h) = 0$ on $\Omega \setminus K$ with $\sigma\nabla \cdot \nu = 0$ on Γ and $h = g$ on ∂K with $g \in H^{\frac{1}{2}}(\Gamma)/\mathbb{R}$. Because σ is smooth on $\Omega \setminus K$ we can apply remark 7.2 from Lions and Magenes (1972) and therefore $h|_{\Omega\setminus K} \in H^1(\Omega \setminus K)$. Since $h|_{K^\circ} \in H^1(K^\circ)$ and since $h|_K$ and $h|_{\Omega\setminus K}$ are identical on ∂K, we derive $h \in H^1(\Omega)$. Hence h satisfies $\operatorname{div}(\sigma\nabla h) = 0$ on Ω and $\sigma\nabla h \cdot \nu = 0$ on Γ. We can now apply Green's formula and derive

$$\int_\Omega \sigma\nabla h \cdot \nabla v \, dx = 0 \quad \forall v \in H^1(\Omega)/\mathbb{R}.$$

The lemma of Lax-Milgram tells us that the solution of this variational problem is unique in $H^1(\Omega)/\mathbb{R}$. Obviously 0 solves this problem as well, hence h must be constant. Therefore u is unique in $\mathcal{W}^s(\Omega)/\mathbb{R}$. □

Theorem 10. For $I \in \mathbb{R}^L_\diamond$ problem 7 has a unique solution $u \in H^{\frac{1}{2}-\varepsilon}(\Omega)/\mathbb{R}$, $\varepsilon > 0$. Furthermore there is $C > 0$ with $\|u\|_{H^{\frac{1}{2}-\varepsilon}(\Omega)/\mathbb{R}} \leq C|I|$.

Proof. Note that we can bound $\|\sum_{m=1}^L I_m \delta_{x_m}\|_{H^{-(1+\varepsilon)}(\Gamma)}$ by $|I|$. Hence the theorem follows directly from the previous one. □

Theorem 11. Under the assumptions of this section the Neumann-to-Dirichlet map $\Lambda : H^s_\diamond(\Gamma) \to H^{s+1}(\Gamma)/\mathbb{R}, f \mapsto u|_\Gamma$ is well defined and continuous.

Proof. This proof is based on Hanke et al. (2011b, Thm. A.3.).
Let $f \in H^s_\diamond(\Gamma)$. Further let $u \in \mathcal{W}^s(\Omega)$ and $u_0 \in H^{s+\frac{3}{2}}(\Omega)$ be defined as in the previous proof of theorem 8. Recall the splitting of the conductivity in a smooth and non-smooth part and in this context the definition of K. We choose a C^∞-domain $V \Subset \Omega$ with $K \subset V$ and another two C^∞-domains $U \Subset U_0 \Subset \Omega \setminus K$ with $\partial V \subset U$. Now u solves $\operatorname{div}(\sigma\nabla u) = 0$ in $\Omega \setminus V$ in the distributional sense. With the appropriate trace theorem and the continuous dependence on the boundary data (Lions and Magenes, 1972, Remark 7.2), we obtain

$$\|u\|_{H^{s+1}(\Gamma)/\mathbb{R}} \leq C\|u\|_{H^{s+\frac{3}{2}}(\Omega\setminus V)/\mathbb{R}} \leq C(\|f\|_{H^s(\Gamma)} + \|\sigma\nabla u \cdot \nu\|_{H^s(\partial V)}). \tag{1.26}$$

According to lemma 9, there is $C > 0$ with $\|u\|_{H^{s+\frac{3}{2}}(U)/\mathbb{R}} \leq C\|u\|_{H^{\min\{s+\frac{3}{2},1\}}(U_0)/\mathbb{R}}$. Using the trace theorem, the inequality form theorem 8 and the fact, that σ is bounded, we conclude

$$\|\sigma\nabla u \cdot \nu\|_{H^s(\partial V)} \leq C\|u\|_{H^{s+\frac{3}{2}}(U\setminus V)/\mathbb{R}} \leq C\|u\|_{H^{s+\frac{3}{2}}(U)/\mathbb{R}} \leq C\|u\|_{H^{\min\{s+\frac{3}{2},1\}}(U_0)/\mathbb{R}} \leq C\|f\|_{H^s(\Gamma)}$$

and hence the proof is finished. □

1.3.2. Complete Electrode Model

Although the PEM offers some advantages for the FEM discretization, as we will see later, this is a fairly unrealistic model. In order to incorporate size and shape of the electrodes, one could go back to the CM and try to specify the current density injection on each electrode $e_m \subset \Gamma$ by

$$\sigma\nabla u \cdot \nu = J_m \quad \text{on } e_m, \quad m = 1, \ldots, L \tag{1.27}$$

and

$$\sigma\nabla u \cdot \nu = 0 \quad \text{on } \Gamma \setminus \bigcup e_m. \tag{1.28}$$

Unfortunately in practice we are not able to control the current density on the electrode, only the total current. Therefore it is reasonable to replace the condition (1.27) by

$$\int_{e_m} \sigma \nabla u \cdot \nu \, d\mathcal{H}^2 = I_m, \quad m = 1, \dots, L. \tag{1.29}$$

Since electrodes are highly conductive, current will shunt through the electrode, causing the potential to be nearly constant at the electrode. Naively we can make the assumption of perfect conducting electrodes and therefore additionally impose the condition

$$u|_{e_m} = U_m \in \mathbb{R}, \quad m = 1, \dots, L.$$

Notice that U_m is unknown as well and becomes part of the problem. We can see that this effect is compatible with (1.29), as current can freely flow in and out of the electrode, as long as the overall current on the electrode is equal to I_m. These boundary conditions are called the shunt model. According to Holder (2004) it predicts that the current density has a singularity of the form $O(r^{-\frac{1}{2}})$, where r is the distance to the edge of the electrode. The potential, while still continuous, has the asymptotics $O(r^{\frac{1}{2}})$. Cheng et al. (1989) investigated different modeling approaches in electrical impedance tomography (EIT) and compared these to real measurements. The forward problem of EIT is closely related to the tDCS problem. They found out, that there is still a discrepancy between the predictions of the shunt model and the measurements. In medical applications a contact impedance layer between skin and electrode exists. Somersalo et al. (1992) assume this is due to a electrochemical effect at the saline-electrode interface, where a thin, highly resistive layer forms, which we will characterize by the effective contact impedance $z_m \geq 0$, $m = 1, \dots, L$. Therefore the shunting effect is modified and the potential is no longer constant underneath the electrode. The voltage drop is given by $z_m \sigma \nabla u \cdot \nu$, thus

$$u + z_m \sigma \nabla u \cdot \nu = U_m \quad \text{on } e_m, \quad m = 1 \dots L. \tag{1.30}$$

According to Holder (2004) a nonzero contact impedance removes the singularity in the current density, however there still occur high current densities at the edges of the electrodes. The new boundary conditions (1.28), (1.29) and (1.30) are called the complete electrode model (CEM). We will mostly follow Somersalo et al. (1992) in this section. Further we will only assume that Ω is a Lipschitz domain and drop the additional regularity assumption of σ near the boundary. We identify each electrode with some subset $e_m \subset \Gamma$. Furthermore we assume that $e_1, \dots, e_L$ are open connected subsets of Γ whose closures are disjoint. For simplicity we assume that the boundaries of the electrodes are smooth curves in Γ. Furthermore we impose $z_m > 0$ for $m = 1, \dots, L$ and assume the contact impedance to be constant on each electrode. With the new unknowns, our solution space is given by $\mathcal{H} = H^1(\Omega) \oplus \mathbb{R}^L$.
The CEM forward problem for $I \in \mathbb{R}^L_\diamond$ is given by

$$\operatorname{div}(\sigma \nabla u) = 0 \quad \text{on } \Omega \tag{1.31}$$

in the weak sense with

$$u + z_m \sigma \nabla u \cdot \nu = U_m \quad \text{on } e_m, \quad m = 1, \dots, L, \quad \text{and} \quad \sigma \nabla u \cdot \nu = 0 \quad \text{on } \Gamma \setminus \bigcup e_m \tag{1.32}$$

in the trace sense, i.e. in $H^{-\frac{1}{2}}(\Gamma)$, and

$$\int_{e_m} \sigma \nabla u \cdot \nu \, d\mathcal{H}^2 = I_m, \quad m = 1 \dots L, \tag{1.33}$$

where $(u, U) \in \mathcal{H}$. Since $\sigma \nabla u \cdot \nu \in H^{-\frac{1}{2}}(\Gamma)$, it's not immediately clear how to understand (1.33). But (1.32) yields

$$\sigma \nabla u \cdot \nu = \sum_{m=1}^{L} \frac{1}{z_m} (U_m - u) \chi_{e_m} \tag{1.34}$$

with the equality holding in $H^{-\frac{1}{2}}(\Gamma)$ and therefore $\sigma\nabla u\cdot\nu\in L^2(\Gamma)$. Actually one gets $\sigma\nabla u\cdot\nu\in H^s(\Gamma)$ for $-\frac{1}{2}\leq s<\frac{1}{2}$, since the boundaries of the electrodes are smooth (Khor and Rodrigo, 2020). Therefore the integral can be understood in the classical sense. We define $a:\mathcal{H}\times\mathcal{H}\to\mathbb{R}$ and $l:\mathcal{H}\to\mathbb{R}$ by

$$a((u,U),(v,V))=\int_\Omega\sigma\nabla u\cdot\nabla v\,dx+\sum_{m=1}^{L}\frac{1}{z_m}\int_{e_m}(u-U_m)(v-V_m)\,d\mathcal{H}^2,\quad l((v,V))=\sum_{m=1}^{L}I_mV_m.$$

Now let I be a current pattern and $(u,U)\in H$ a solution of the CEM. Let $(v,V)\in\mathcal{H}$ be arbitrary. We can use Green's formula (1.13) and derive

$$0=\int_\Omega\operatorname{div}(\sigma\nabla u)v\,dx=\langle\sigma\nabla u\cdot\nu,v\rangle_{H^{-\frac{1}{2}}(\Gamma)\times H^{\frac{1}{2}}(\Gamma)}-\int_\Omega\sigma\nabla u\cdot\nabla v\,dx.$$

Plugging in (1.34) yields

$$0=\sum_{m=1}^{L}\frac{1}{z_m}\int_{e_m}(U_m-u)v\,d\mathcal{H}^2-\int_\Omega\sigma\nabla u\nabla v\,dx. \tag{1.35}$$

Since $\sigma\nabla u\cdot\nu\in L^2(\Gamma)$ we can write

$$\frac{1}{z_m}\int_{e_m}u-U_m\,d\mathcal{H}^2=-\int_{e_m}\sigma\nabla u\cdot\nu\,d\mathcal{H}^2=-I_m-$$

Thus

$$\sum_{m=1}^{L}\frac{1}{z_m}\int_{e_m}-(u-U_m)V_m\,d\mathcal{H}^2=\sum_{m=1}^{L}I_mV_m.$$

Adding this to (1.35) we obtain

$$\int_\Omega\sigma\nabla u\cdot\nabla v\,dx+\sum_{m=1}^{L}\frac{1}{z_m}(u-U_m)(v-V_m)=\sum_{m=1}^{L}I_mV_m.$$

Now conversely let $(u,U)\in\mathcal{H}$ satisfy

$$a((u,U),(v,V))=l((v,V))\quad\forall(v,V)\in\mathcal{H}.$$

With choosing $\varphi\in\mathcal{D}(\Omega)$ and $V=0$ we see that $\operatorname{div}(\sigma\nabla u)=0$ in the weak sense. Next we choose $v\in H^1(\Omega)$ and $V=0$, thus

$$\int_\Omega\sigma\nabla u\cdot\nabla v\,dx+\sum_{m=1}^{L}\frac{1}{z_m}\int_{e_m}(u-U_m)v\,d\mathcal{H}^2=0.$$

Since $\sigma\nabla u\in H(\operatorname{div};\Omega)$, we can use Green's formula and derive

$$\langle\sigma\nabla u\cdot\nu,v\rangle=\sum_{m=1}^{L}\frac{1}{z_m}\int_{e_m}(u-U_m)v\,d\mathcal{H}^2.$$

Since $H^{\frac{1}{2}}(\Gamma)$ are the traces of $H^1(\Omega)$ functions, we obtain $\sigma\nabla u\cdot\nu=\sum_{m=1}^{L}\frac{1}{z_m}(u-U_m)\chi_{e_m}$ in $H^{-\frac{1}{2}}(\Gamma)$. Hence $\sigma\nabla u\cdot\nu\in L^2(\Gamma)$ and

$$\int_{e_m}\sigma\nabla u\cdot\nu\,d\mathcal{H}^2=\frac{1}{z_m}\int_{e_m}(U_m-u)\,d\mathcal{H}^2,$$

which is equal to I_m. Indeed, we can choose $v=0$ and V equal to the lth standard unit vector

$$-\frac{1}{z_m}\int_{e_m}(u-U_m)\,d\mathcal{H}^2=I_m.$$

Problem 12. For a current pattern $I \in \mathbb{R}^l_\diamond$ the weak formulation of the CEM forward problem is given by

$$\text{Find } (u,U) \in H^1(\Omega)\oplus\mathbb{R}^L \text{ with } a((u,U),(v,V)) = l((v,V)) \quad \forall (v,V)\in H^1(\Omega)\oplus\mathbb{R}^L. \tag{1.36}$$

As we have already encountered earlier, the potential is only unique up to an additive constant. Therefore the bilinearform a isn't coercive. $a((v,V),(v,V)) = 0$ only implies $v = V_1 = \cdots = V_L = \text{const}$. As we want to use the lemma of Lax-Milgram in order to prove existence, we need to show that a is coercive on $\mathcal{H}/\mathbb{R}$. To be precise by $\mathbb{R}\in\mathcal{H}$ we mean the subspace $\mathbb{R}\cdot(1,1)$ where $1\in H^1(\Omega)$ is the constant function of value 1 and $1\in\mathbb{R}^L$ with 1 in each component. Therefore we want to define a norm which is equivalent to the quotient norm by

$$\|(u,U)\|_*^2 = \|\nabla u\|^2_{L^2(\Omega)} + \sum_{m=1}^L \int_{e_m} |u-U_m|^2\, d\mathcal{H}^2.$$

Lemma 13. $\|\cdot\|_*$ is a norm on $(H^1(\Omega)\oplus\mathbb{R}^L)/\mathbb{R}$ and equivalent to the quotient norm.

Proof. We can see that $\|\cdot\|_*$ is well defined on $\mathcal{H}/\mathbb{R}$, absolute homogeneous, non-negative and that it satisfies the triangle inequality. Furthermore $\|(u,U)\|_* = 0$ implies that u is constant by the Poincaré inequality (1.14), thus $U_1 = \cdots = U_L = u = \text{const}$. Hence $(u,U) = 0$ in $\mathcal{H}/\mathbb{R}$. Next we will show that the norms are equivalent. Let $(u,U)\in\mathcal{H}/\mathbb{R}$ and further be $c\in\mathbb{R}$ arbitrary. First note the elementary inequality $(a+b)^2 \le 2a^2+2b^2$, which we'll use quite frequently. Hence

$$\begin{aligned}\|(u,U)\|_*^2 &\le \|\nabla(u-c)\|^2_{L^2(\Omega)} + \sum_{m=1}^L \int_{e_m} \left(|u-c| + |U_m - c|\right)^2 d\mathcal{H}^2 \\ &\le \|\nabla(u-c)\|^2_{L^2(\Omega)} + 2\sum_{m=1}^L \int_{e_m} |u-c|^2\, d\mathcal{H}^2 + 2\sum_{m=1}^L |U_m-c|^2 |e_m|.\end{aligned}$$

Using the trace theorem we can further derive

$$\sum_{m=1}^L \int_{e_m} |u-c|^2\, d\mathcal{H}^2 \le \|u-c\|^2_{L^2(\Gamma)} \le C\|u-c\|^2_{H^1(\Omega)}.$$

Combining this yields

$$\|(u,U)\|_*^2 \le C(\|\nabla(u-c)\|^2_{L^2(\Omega))} + \|u-c\|^2_{H^1(\Omega)} + \sum_{m=1}^L |U_m-c|^2) \le C(\|u-c\|^2_{H^1(\Omega)} + |U-c|^2).$$

Note that C can be choose independent of the electrode set up, as $|e_m| \le |\Gamma|$. Since $c\in\mathbb{R}$ was arbitrary we deduce $\|(u,U)\|_*^2 \le C\|(u,U)\|^2_{\mathcal{H}/\mathbb{R}}$.
We want to show the opposite estimate. Let $(u,U)\in\mathcal{H}/\mathbb{R}$. Then it follows

$$\begin{aligned}\|(u,U)\|^2_{\mathcal{H}/\mathbb{R}} &= \inf_{c\in\mathbb{R}} \|u-c\|^2_{H^1(\Omega)} + \sum_{m=1}^L |U_m-c|^2 = \inf_{c\in\mathbb{R}} \|u-c\|^2_{H^1(\Omega)} + \sum_{m=1}^L \frac{1}{|e_m|}\|U_m-c\|^2_{L^2(e_m)} \\ &\le \inf_{c\in\mathbb{R}} \|u-c\|^2_{H^1(\Omega)} + \sum_{m=1}^L \frac{2}{|e_m|}\left(\|u-c\|^2_{L^2(e_m)} + \|u-U_m\|^2_{L^2(e_m)}\right).\end{aligned}$$

Since the electrode set up is fixed, we can bound $|e_m|^{-1}$. Applying the trace theorem yields

$$\begin{aligned}\|(u,U)\|^2_{\mathcal{H}/\mathbb{R}} &\le C\left[\inf_{c\in\mathbb{R}} \|u-c\|^2_{H^1(\Omega)} + \|u-c\|^2_{L^2(\Gamma)} + \sum_{m=1}^L \|u-U_m\|^2_{L^2(e_m)}\right] \\ &\le C\left[\inf_{c\in\mathbb{R}} \|u-c\|^2_{H^1(\Omega)} + \sum_{m=1}^L \|u-U_m\|^2_{L^2(e_m)}\right].\end{aligned}$$

We can now apply the Poincaré inequality (1.14), thus

$$\|(u,U)\|^2_{\mathcal{H}/\mathbb{R}} \leq C\left[\|\nabla u\|^2_{H^1(\Omega)} + \sum_{m=1}^{L}\|u-U_m\|^2_{L^2(e_m)}\right] = C\|(u,U)\|^2_*.$$

□

Theorem 14. Assume $z_m > 0$ for $m = 1 \dots L$, then for $I \in \mathbb{R}^L_\diamond$ the CEM forward problem has a unique solution $(u,U) \in (H^1(\Omega)\oplus\mathbb{R}^L)/\mathbb{R}$. Furthermore there is $C > 0$ with

$$\|(u,U)\|_{\mathcal{H}/\mathbb{R}} \leq C|I|.$$

Proof. Obviously a is symmetric, bilinear and satisfies

$$a((u,U),(u,U)) \geq \int_\Omega c|\nabla u|^2\,dx + \frac{1}{\max_m z_m}\sum_{m=1}^{L}\int_{e_m}(u-U_m)^2\,d\mathcal{H}^2 \geq c\|(u,U)\|^2_*. \tag{1.37}$$

Furthermore with the Cauchy-Schwarz inequality we can derive

$$\begin{aligned}|a((u,U),(v,V))| &\leq \|\sigma\|_{L^\infty(\Omega)}\|\nabla u\|_{L^2(\Omega)}\|\nabla v\|_{L^2(\Omega)} + \sum_{m=1}^{L}\frac{1}{z_m}\int_{e_m}(u-U_m)^2\,d\mathcal{H}^2\int_{e_m}(v-V_m)^2\,d\mathcal{H}^2\\ &\leq C\|(u,U)\|_*\|(v,V)\|_*.\end{aligned} \tag{1.38}$$

Since the norms are equivalent, a is coercive and bounded w.r.t the quotient space norm. The map $l : \mathcal{H}/\mathbb{R} \to \mathbb{R}$ is well defined since $I \in \mathbb{R}^L_\diamond$, i.e. $l((1,1)) = 0$, and it is clearly linear. Now assume $(v,V) \in \mathcal{H}/\mathbb{R}$. Let us choose $c \in \mathbb{R}$ such that

$$(\|v-c\|^2_{H^1(\Omega)} + \|V-c\|^2_{\mathbb{R}^L})^{\frac{1}{2}} \leq \|(v,V)\|_{\mathcal{H}/\mathbb{R}} + \varepsilon.$$

Using Cauchy-Schwarz inequaltiy we get

$$|l((v,V))| = |\sum_{m=1}^{L} I_m V_m| = |\sum_{m=1}^{L} I_m(V_m - c)| \leq |I|\|V-c\|_{\mathbb{R}^L} \leq |I|(\|(v,V)\|_{\mathcal{H}/\mathbb{R}} + \varepsilon).$$

Since $\varepsilon > 0$ was arbitrary, we deduce that l is continuous. Applying the lemma of Lax-Milgram completes the proof. □

Corollary 15. Under the above assumptions there exists a unique solution $(u,U) \in H^1(\Omega)\oplus\mathbb{R}^L$ satisfying $\sum_{m=1}^{L} U_m = 0$.

1.3.3. Convergence of CEM towards PEM solution for small electrodes

So far we have introduced the point electrode model and the complete electrode model as two separate models, which at first sight have little in common. We want to prove that under realistic assumptions the solutions of the CEM locally converges towards the solution of the PEM, when the diameter of the electrodes decreases. The whole section will guide us to this main theorem 18. We follow Hanke et al. (2011a). Let the assumptions of section 1.3.1 hold, even though we could probably relax the regularity assumptions on Ω, as we only need the results for small s. Let us further assume that the electrodes $e_m \subset \Gamma$ are simply connected and that $0 < Z < z_m < \tilde{Z},\ m = 1,\dots,L$. In the previous section we showed that the norms $\|\cdot\|_*$ and $\|\cdot\|_{\mathcal{H}/\mathbb{R}}$ are equivalent, i.e. there exist constants $C_1, C_2 > 0$ with

$$C_1\|(u,U)\|_* \leq \|(u,U)\|_{\mathcal{H}/\mathbb{R}} \leq C_2\|(u,U)\|_*$$

for all $(u,U) \in \mathcal{H}/\mathbb{R}$. Unfortunately, with this norm C_2 cannot be independent of e_m. Since we are interested in the behavior as $|e_m| \to 0$, this should not be the case. Therefore we define a quite similar norm on $\mathcal{H}^1 \oplus \mathbb{R}^L$ by

$$\|(u,U)\|^2 = \|u\|^2_{H^1(\Omega)} + \sum_{m=1}^{L} \|U_m\|^2_{L^2(e_m)} = \|u\|^2_{H^1(\Omega)} + \sum_{m=1}^{L} |U_m|^2 |e_m|$$

and denote the resulting quotient norm by $\|\cdot\|_\diamond$. Notice that this norm clearly is equivalent to $\|\cdot\|_{\mathcal{H}/\mathbb{R}}$ for a fixed electrode set-up. The new norm has the advantage that there exists $C_1, C_2 > 0$, now independent of e_m, $m = 1, \dots, L$, with

$$C_1 \|(u,U)\|_* \le \|(u,U)\|_\diamond \le C_2 \|(u,U)\|_*.$$

Let us denote $\Gamma_e = \bigcup e_m$ and identify $U = \sum_{m=1}^{L} U_m \chi_{e_m}$. The proof is very similar to the one we have done before.

Proof. We can derive

$$\|(u,U)\|^2_\diamond = \inf_{c\in\mathbb{R}} (\|u-c\|^2_{H^1(\Omega)} + \|U-c\|^2_{L^2(\Gamma_e)}) \le \inf_{c\in\mathbb{R}} (\|u-c\|^2_{H^1(\Omega)} + 2\|U-u\|^2_{L^2(\Gamma_e)} + 2\|u-c\|^2_{L^2(\Gamma_e)}).$$

We can continue

$$\begin{aligned}
\|(u,U)\|^2_\diamond &\le \inf_{c\in\mathbb{R}} (\|u-c\|^2_{H^1(\Omega)} + 2\|u-c\|^2_{L^2(\Gamma)}) + 2\|U-u\|^2_{L^2(\Gamma_e)} \\
&\le C \inf_{c\in\mathbb{R}} (\|u-c\|^2_{H^1(\Omega)} + 2\|u-c\|^2_{H^1(\Omega)}) + 2\|U-u\|^2_{L^2(\Gamma_e)} \\
&\le C\|\nabla u\|^2_{L^2(\Omega)} + 2\|U-u\|^2_{L^2(\Gamma_e)} \le C\|(u,U)\|^2_*
\end{aligned}$$

where we used the trace theorem and Poincaré inequality. Conversely for $c \in \mathbb{R}$

$$\begin{aligned}
\|(u,U)\|^2_* &= \|\nabla u\|^2_{L^2(\Omega)} + \|U-u\|^2_{L^2(\Gamma_e)} \le \|u-c\|_{H^1(\Omega)} + 2\|u-c\|^2_{L^2(\Gamma_e)} + 2\|U-c\|^2_{L^2(\Gamma_e)} \\
&\le C(\|u-c\|_{H^1(\Omega)} + \|U-c\|^2_{L^2(\Gamma_e)}).
\end{aligned}$$

We used the trace theorem and Poincaré inequality again. Hence

$$\|(u,U)\|^2_* \le C\|(u,U)\|^2_\diamond.$$

Notice that in both cases $C > 0$ can be chosen independent of e_m. □

When we showed that a is coercive and bounded w.r.t. $\|\cdot\|_*$ in (1.37) and (1.38) the constants were independent of e_m, $m = 1, \dots, L$, as well. Next we consider $l : \mathcal{H}/\mathbb{R} \to \mathbb{R}$. It remains continuous w.r.t. $\|\cdot\|_\diamond$. For $c \in \mathbb{R}$ it follows

$$\begin{aligned}
|l((v,V))| &= |\sum_{m=1}^{L} I_m(V_m - c)| \le \sum_{m=1}^{L} \int_{e_m} \frac{|I_m|}{|e_m|} |V_m - c| \, d\mathcal{H}^2 \le \Big\| \sum_{m=1}^{L} \frac{|I_m|}{|e_m|} \chi_{e_m} \Big\|_{L^2(\Gamma)} \Big\| \sum_{m=1}^{L} |V_m - c| \chi_{e_m} \Big\|_{L^2(\Gamma)} \\
&= \left(\int_\Gamma \sum_{m=1}^{L} \frac{|I_m|^2}{|e_m|^2} \chi_{e_m} \, d\mathcal{H}^2 \right)^{\frac{1}{2}} \left(\int_\Gamma \sum_{m=1}^{L} |V_m - c|^2 \chi_{e_m} \, d\mathcal{H}^2 \right)^{\frac{1}{2}} = \left(\sum_{m=1}^{L} \frac{I_m^2}{|e_m|} \right)^{\frac{1}{2}} \|V - c\|_{L^2(\Gamma_e)}.
\end{aligned}$$

Hence for the solution of the CEM we get

$$\|(u,U)\|^2_\diamond \le C\|(u,U)\|^2_* \le Ca((u,U),(u,U)) = Cl((u,U)) \le C \left(\sum_{m=1}^{L} \frac{I_m^2}{|e_m|} \right)^{\frac{1}{2}} \|(u,U)\|_\diamond.$$

Thus there is $C > 0$ independent of the electrode set up with

$$\|(u, U)\|_\diamond^2 \leq C \sum_{m=1}^{L} \frac{I_m^2}{|e_m|}. \tag{1.39}$$

We can derive a similar estimate for $\sigma \nabla u \cdot \nu \in L^2(\Gamma)$. For $c \in \mathbb{R}$ we see

$$\begin{aligned}\|\sigma \nabla u \cdot \nu\|_{L^2(\Gamma)}^2 &= \Big\| \sum_{m=1}^{L} \frac{1}{z_m}(U_m - u)\chi_{e_m} \Big\|_{L^2(\Gamma)}^2 \leq \frac{2}{Z}\left[\Big\| \sum_{m=1}^{L}(U_m - c)\chi_{e_m} \Big\|_{L^2(\Gamma)}^2 + \Big\| \sum_{m=1}^{L}(u-c)\chi_{e_m} \Big\|_{L^2(\Gamma)}^2 \right] \\ &\leq C\Big(\|U - c\|_{L^2(\Gamma_e)}^2 + \|u - c\|_{H^1(\Omega)}^2 \Big),\end{aligned}$$

where we once again used Young's inequality and the trace theorem. Combining this with the inequality (1.39) we obtained before, we can derive

$$\|\sigma \nabla u \cdot \nu\|_{L^2(\Gamma)}^2 \leq C\|(u, U)\|_\diamond^2 \leq C \sum_{m=1}^{L} \frac{I_m^2}{|e_m|}. \tag{1.40}$$

We see that the constant is independent of the electrode setup as well.
At the beginning of this section we mentioned that we want to shrink the electrodes. We will make this more precise now. We will denote the electrodes by e_m^h, $m = 1 \dots L$, where $h > 0$ can be interpreted as the size of the electrodes. We assume that $h > 0$ is bounded above by h_0. Let $x_m \in \Gamma$ be the position of the mth point electrode. We assume there is a fixed convex open bounded reference domain

$$Q \subset \mathbb{R}^2 \quad \text{with} \quad |Q| = 1,\ 0 \in Q,$$

such that for $h \in (0, h_0)$ each electrode $e_m^h \subset \Gamma$, $m = 1, \dots, L$, is given by the parametrization

$$e_m^h = X_m^h(Q^h) \quad \text{with} \quad Q^h = hQ,$$

where $\tilde{X}_m^h : U^h \to \tilde{X}_m^h(U^h)$ is a C^∞-diffeomorphism, $Q^h \times \{0\} \subset U^h$ and $X_m^h = \tilde{X}_m^h \circ \iota$ for the embedding $\iota : \mathbb{R}^2 \to \mathbb{R}^3$. The Hausdorff measure on e_m^h is given by

$$\mathcal{H}^2(A) = \int_{{X_m^h}^{-1}(A)} \sqrt{\det\left({DX_m^h}^T DX_m^h \right)}\, dx.$$

We denote $\sigma_m^h = \sqrt{{DX_m^h}^T DX_m^h}$, which can be interpreted as a local stretching factor. We have

$$\int_{e_m^h} g\, d\mathcal{H}^2 = \int_{Q^h} (g \circ X_m^h)\sigma_m^h\, dx$$

for every integrable function g on e_m^h. We assume that the stretching factor is bounded $c \leq \sigma_m^h \leq C$ by constants $c, C > 0$ independent of m and h, e.g. the parametrizations X_m^h could remain the same for $h \to 0$ and only Q^h could shrink. Further we require that

$$\|X_m^h\|_{C^2(\overline{Q^h})} \leq C \tag{1.41}$$

for all $h \in (0, h_0)$ and $m = 1, \dots, L$. We can derive

$$\|\psi \circ X_m^h\|_{H^1(Q^h)} \leq C\|\psi\|_{H^1(e_m^h)} \quad \forall \psi \in H^1(e_m^h), \tag{1.42}$$

where $H^1(e_m^h)$ consists of restrictions of functions from $H^1(\Gamma)$ with the appropriate norm, similar to (1.11). Indeed, let $\psi \in H^1(e_m^h)$. Then for every $\tilde{\psi} \in H^1(\Gamma)$ with $\tilde{\psi}|_{e_m^h} = \psi$ it follows

$$\|\psi \circ X_m^h\|_{H^1(Q^h)} = \|\sum_{j=1}^{k}(\alpha_j \tilde{\psi}) \circ \varphi_j^{-1} \circ \varphi_j \circ X_m^h\|_{H^1(Q^h)} = \|\sum_{j=1}^{k} \varphi_j^*(\alpha_j \tilde{\psi}) \circ \varphi_j \circ X_m^h\|_{H^1(Q^h)},$$

where the notation of section 1.2 for the local charts was used. Note, when $X_m^h(x) \notin O_j$, then $\alpha_j(x) = 0$. Since the α_j have a compact support and φ_m, X_m^h are smooth, with (Ziemer, 1989, Sec. 2.2) and (1.41) we obtain

$$\|\psi \circ X_m^h\|_{H^1(Q^h)} \leq C \sum_{j=1}^{k} \|\varphi_j^*(\alpha_j \tilde{\psi})\|_{H^1(\mathbb{R}^2)} = C\|\tilde{\psi}\|_{H^1(\Gamma)}.$$

for $C > 0$ (independent of h). Additionally, we can derive for every smooth curve $\gamma \subset e_m^h$

$$|\gamma| \leq C|{X_m^h}^{-1}(\gamma)|.$$

Let $\gamma : [0,1] \to e_m^h$ be a smooth curve, then

$$|\gamma| = \int_{[0,1]} |D\gamma|\,dx = \int_{[0,1]} |D(X_m^h \circ {X_m^h}^{-1} \circ \gamma)|\,dx \leq \int_{[0,1]} \|DX_m^h\|_{L^\infty(Q^h)} |D({X_m^h}^{-1} \circ \gamma)|\,dx \leq C|{X_m^h}^{-1}(\gamma)|.$$

Further we can obtain

$$|e_m^h| = \int_{Q^h} \sigma_m^h(x)\,dx = h^2 \int_Q \sigma_m^h(hx)\,dx,$$

meaning that we can bound

$$ch^2 \leq |e_m^h| \leq Ch^2. \tag{1.43}$$

We assume that $x_m = X_m^h(0)$ and in order to derive $O(h^2)$ convergence results, we impose

$$\frac{1}{|Q^h|} \int_{Q^h} x\sigma_m^h(x)\,dx = 0. \tag{1.44}$$

Notice that the preimage of x_m can be interpreted as the weighted center of mass of Q^h, i.e. the point electrode has to be in the center of e_m^h in the appropriate sense.
From now on we will denote the solution of the CEM for the electrode size h by $(u^h, U^h) \in (H^1(\Omega) \oplus \mathbb{R}^L)/\mathbb{R}$ and the solution of the PEM by $u \in H^{\frac{1}{2}-\varepsilon}(\Omega)/\mathbb{R}$.

Lemma 16. There exists $C > 0$ independent of e_m^h, $m = 1, \ldots, L$, and in particular of h, such that u^h satisfies

$$\|\sigma \nabla u^h \cdot \nu\|^2_{H^1(\Gamma_{e,h})} \leq C \sum_{m=1}^{L} \frac{|I_m|^2}{|e_m^h|}.$$

Proof. From theorem 11 we know that the Neumann-to-Dirichlet map $\Lambda : H_\diamond^s(\Gamma) \to H^{s+1}(\Gamma)/\mathbb{R}$, $f \to u|_\Gamma$ is well defined and bounded. Therefore we get

$$\|u^h\|^2_{H^1(\Gamma)/\mathbb{R}} \leq C\|\sigma \nabla u^h \cdot \nu\|^2_{L^2(\Gamma)}.$$

Thus equation (1.40) yields

$$\|u^h\|^2_{H^1(\Gamma)/\mathbb{R}} \leq C \sum_{m=1}^{L} \frac{|I_m|^2}{|e_m^h|}. \tag{1.45}$$

Since $\sigma \nabla u^h \cdot \nu = \sum_{m=1}^{L} \frac{1}{z_m}(U_m^h - u^h)\chi_{e_m^h}$, we have

$$\begin{aligned}\|\sigma \nabla u^h \cdot \nu\|^2_{H^1(\Gamma_{e,h})} &\leq \|\sigma\|_{L^\infty(\Omega)} \frac{1}{Z} \|U^h - u^h\|^2_{H^1(\Gamma_{e,h})} \leq C \left[\sum_{m=1}^{L} \|\nabla u^h\|^2_{L^2(e_m^h)} + \|U^h - u^h\|^2_{L^2(\Gamma_{e,h})} \right] \\ &\leq C\Big[\|u^h\|^2_{H^1(\Gamma)/\mathbb{R}} + \|U^h - u^h\|^2_{L^2(\Gamma_{e,h})}\Big] \leq C \sum_{m=1}^{L} \frac{|I_m|^2}{|e_m^h|} + C\|U^h - u^h\|^2_{L^2(\Gamma_{e,h})},\end{aligned}$$

where we used (1.45) in the last step. We can bound the last summand using the trace theorem

$$\begin{aligned}\|U^h - u^h\|^2_{L^2(\Gamma_{e,h})} &\le 2(\|U^h - c\|^2_{L^2(\Gamma_{e,h})} + \|u^h - c\|^2_{L^2(\Gamma_{e,h})}) \le 2(\|U^h - c\|^2_{L^2(\Gamma_{e,h})} + \|u^h - c\|^2_{L^2(\Gamma)}) \\ &\le C(\|U^h - c\|^2_{L^2(\Gamma_{e,h})} + \|u^h - c\|^2_{H^1(\Omega)}),\end{aligned}$$

for $c \in \mathbb{R}$. Hence with (1.39) we get

$$\|U^h - u^h\|^2_{L^2(\Gamma_{e,h})} \le \|(u^h, U^h)\|_\diamond \le C \sum_{m=1}^{L} \frac{|I_m|^2}{|e_m^h|}.$$

□

Lemma 17. We can find $h_0 > 0$ such that for every $\varepsilon > 0$ there exists $C > 0$ with

$$\|\sigma \nabla (u^h - u) \cdot \nu\|_{H^{-(3+\varepsilon)}(\Gamma)} \le C h^2 |I|$$

for all $0 < h < h_0$ and $I \in \mathbb{R}^L_\diamond$.

Proof. We will abbreviate $f^h = \sigma \nabla u^h \cdot \nu$. Using (1.43) and the previous lemma 16 we get

$$\|f^h\|^2_{H^1(\Gamma_{e,h})} \le C \sum_{m=1}^{L} \frac{|I_m|^2}{|e_m^h|} \le C h^{-2} |I|^2. \tag{1.46}$$

Let us fix $\varphi \in \mathcal{D}(\Gamma)$. Since u solves the PEM, we derive

$$|\langle \sigma \nabla (u^h - u) \cdot \nu, \varphi \rangle| = |\int_\Gamma f^h \varphi \, d\mathcal{H}^2 - \sum_{m=1}^{L} I_m \varphi(x_m)|.$$

Recall $\int_{e_m^h} f^h \, d\mathcal{H}^2 = I_m$, hence

$$\begin{aligned}|\langle \sigma \nabla (u^h - u) \cdot \nu, \varphi \rangle| &= \Big| \sum_{m=1}^{L} \int_{e_m^h} f^h (\varphi - \varphi(x_m)) \, d\mathcal{H}^2 \Big| \\ &\le \sum_{m=1}^{L} \left[\int_{e_m^h} \Big| \Big(f^h - \frac{I_m}{|e_m^h|} \Big) (\varphi - \varphi(x_m)) \Big| \, d\mathcal{H}^2 + \frac{|I_m|}{|e_m^h|} \Big| \int_{e_m^h} \varphi - \varphi(x_m) \, d\mathcal{H}^2 \Big| \right].\end{aligned}$$

Now we can use the Cauchy-Schwarz inequality

$$|\langle \sigma \nabla (u^h - u) \cdot \nu, \varphi \rangle| \le \sum_{m=1}^{L} \Big\| f^h - \frac{I_m}{|e_m^h|} \Big\|_{L^2(e_m^h)} \|\varphi - \varphi(x_m)\|_{L^2(e_m^h)} + \sum_{m=1}^{L} \frac{|I_m|}{|e_m^h|} \Big| \int_{e_m^h} \varphi \, d\mathcal{H}^2 - \varphi(x_m) |e_m^h| \Big|. \tag{1.47}$$

We will try to bound this expression. Fix $m = 1, \dots, L$ and abbreviate $\psi = f^h - \frac{I_m}{|e_m^h|}$. Then

$$\int_{e_m^h} \psi \, d\mathcal{H}^2 = \int_{e_m^h} f^h - \frac{I_m}{|e_m^h|} \, d\mathcal{H}^2 = 0.$$

Using change of variables we can derive

$$0 = \int_{e_m^h} \psi \, d\mathcal{H}^2 = \int_{Q^h} (\psi \circ X_m^h) \sigma_m^h \, dx = h^2 \int_Q \psi \circ X_m^h(hx) \, \sigma_m^h(hx) \, dx.$$

We can therefore apply the Poincaré inequality and obtain

$$\int_Q |\psi \circ X_m^h(hx) \sigma_m^h(hx)|^2 \, dx \le C \int_Q |\nabla_x (\psi \circ X_m^h(hx) \sigma_m^h(hx))|^2 \, dx.$$

The chain rule yields $\nabla_x(\psi \circ X_m^h(hx)\sigma_m^h(hx)) = h\nabla(\psi \circ X_m^h(hx)\sigma_m^h(hx))$ and with change of variables it follows

$$h^{-2}\int_{Q^h}|(\psi \circ X_m^h)\sigma_m^h|^2\,d = \int_Q|\psi \circ X_m^h(hx)\sigma_m^h(hx)|^2\,dx \le C\int_Q|\nabla_x(\psi \circ X_m^h(hx)\sigma_m^h(hx))|^2\,dx$$
$$= h^2C\int_Q|\nabla(\psi \circ X_m^h(hx)\sigma_m^h(hx))|^2\,dx = C\int_{Q^h}|\nabla((\psi \circ X_m^h)\sigma_m^h)|^2\,dx.$$

This detour, using change of variables twice, has the benefit that C can be chosen independent of h, as we used the Poincaré inequality only on the reference domain Q. We continue by

$$\Big\|f^h - \frac{I_m}{|e_m^h|}\Big\|^2_{L^2(e_m^h)} = \|\psi\|^2_{L^2(e_m^h)} = \int_{e_m^h}|\psi|^2\,d\mathcal{H}^2 = \int_{Q^h}|\psi \circ X_m^h|^2\sigma_m^h\,dx \le \frac{1}{c}\int_{Q^h}|(\psi \circ X_m^h)\sigma_m^h|^2\,dx$$
$$\le h^2C\int_{Q^h}|\nabla((\psi \circ X_m^h)\sigma_m^h)|^2\,dx.$$

Recall that the norm of σ_m^h in $C^1(\overline{Q^h})$ is uniformly bounded w.r.t. h. Together with the estimate (1.42) it follows

$$\Big\|f^h - \frac{I_m}{|e_m^h|}\Big\|^2_{L^2(e_m^h)} \le Ch^2\int_{Q^h}|\nabla(\psi \circ X_m^h)|^2\,dx \le Ch^2\|\psi\|^2_{H^1(e_m^h)} = Ch^2\Big\|f^h - \frac{I_m}{|e_m^h|}\Big\|^2_{H^1(e_m^h)}$$
$$\le Ch^2\Big(\Big\|f^h - \frac{I_m}{|e_m^h|}\Big\|^2_{L^2(e_m^h)} + \|f^h\|^2_{H^1(e_m^h)}\Big).$$

Since $C > 0$ is independent of h, we can choose $h_0 > 0$ such that $Ch^2 < 1$ for $0 < h < h_0$. Hence

$$\Big\|f^h - \frac{I_m}{|e_m^h|}\Big\|^2_{L^2(e_m^h)} \le h^2C\|f^h\|^2_{H^1(e_m^h)},$$

which we can bound by (1.46), i.e.

$$\Big\|f^h - \frac{I_m}{|e_m^h|}\Big\|^2_{L^2(e_m^h)} \le C|I|^2. \tag{1.48}$$

Next we want to bound $\|\varphi - \varphi(x_m)\|^2_{L^2(e_m^h)}$ in (1.47). For every $x \in e_m^h$ there exists a smooth curve $\gamma \subset e_m^h$ connecting x and x_m with $|\gamma| \le Ch$, e.g. take the line segment connecting 0 and ${X_m^h}^{-1}(x)$ and map it to e_m^h, then

$$|\gamma| \le C|{X_m^h}^{-1}(\gamma)| = C|{X_m^h}^{-1}(x) - 0| \le Ch.$$

Thus

$$|\varphi(x) - \varphi(x_m)| \le \int_{[0,1]}|(\varphi \circ \gamma)'(x)|\,dx \le Ch\|\varphi\|_{C^1(\Gamma)}$$

and using the bounds on $|e_m^h|$ (1.43) we get

$$\|\varphi - \varphi(x_m)\|^2_{L^2(e_m^h)} \le Ch^2\|\varphi\|^2_{C^1(\Gamma)}|e_m^h| \le C\ h^4\|\varphi\|^2_{C^1(\Gamma)}. \tag{1.49}$$

The last term in (1.47) to bound is $\Big|\int_{e_m^h}\varphi\,d\mathcal{H}^2 - \varphi(x_m)|e_m^h|\Big|$. Since Q^h is convex, we can use Taylor's theorem (Königsberger, 2000, Sec. 2.4) in order to expand $\varphi \circ X_m^h$ around 0

$$\varphi \circ X_m^h(x) = \varphi(x_m) + x \cdot \nabla(\varphi \circ X_m^h)(0) + r(x)$$

with

$$|r(x)| \le C|x|^2\|\varphi \circ X_m^h\|_{C^2(\overline{Q^h})} \le C|x|^2\|\varphi\|_{C^2(\Gamma)}.$$

It follows with the assumption (1.44),

$$\begin{aligned}\int_{Q^h}(\varphi\circ X_m^h)\sigma_m^h\,dx &= \varphi(x_m)\int_{Q^h}\sigma_m^h\,dx + \nabla(\varphi\circ X_m^h)(0)\int_{Q^h}x\sigma_m^h(x)\,dx + \int_{Q^h}r\sigma_m^h\,dx\\ &= \varphi(x_m)|e_m^h| + \int_{Q^h}r\sigma_m^h\,dx.\end{aligned}$$

Note that $|Q^h| = h^2$ and $|x|^2 \le Ch^2$ for $x \in Q^h$. Therefore we get

$$\Big|\int_{e_m^h}\varphi\,d\mathcal{H}^2 - \varphi(x_m)|e_m^h|\Big| = \Big|\int_{Q^h}r(x)\sigma_m^h(x)\,dx\Big| \le Ch^4\|\varphi\|_{C^2(\Gamma)}. \tag{1.50}$$

Plugging (1.48), (1.49), (1.50), (1.43) into (1.47) yields

$$\begin{aligned}|\langle\sigma\nabla(u^h-u)\cdot\nu,\varphi\rangle| &\le Ch^2\|\varphi\|_{C^2(\Gamma)}|I| + \left(\sum_{m=1}^L\frac{|I_m|^2}{|e_m^h|^2}\right)^{\frac12}\left(\sum_{m=1}^L\Big|\int_{e_m^h}\varphi\,d\mathcal{H}^2-\varphi(x_m)|e_m^h|\Big|^2\right)^{\frac12}\\ &\le Ch^2\|\varphi\|_{C^2(\Gamma)}|I| + Ch^2\|\varphi\|_{C^2(\Gamma)}|I| \le Ch^2\|\varphi\|_{C^2(\Gamma)}|I|.\end{aligned}$$

According to Wloka (1987, Thm. 6.5) the Sobolev embedding $H^{3+\varepsilon}(\Gamma)\hookrightarrow C^2(\Gamma)$ is bounded for $\varepsilon>0$. Hence there exists $C>0$, dependent on ε, with

$$|\langle\sigma\nabla(u^h-u)\cdot\nu,\varphi\rangle| \le Ch^2\|\varphi\|_{C^2(\Gamma)}|I| \le Ch^2|I|\|\varphi\|_{H^{3+\varepsilon}(\Gamma)}.$$

Since $\mathcal{D}(\Gamma)$ is dense in $H^{3+\varepsilon}(\Gamma)$ (Lions and Magenes, 1972), we finally conclude

$$\|\sigma\nabla(u^h-u)\cdot\nu\|_{H^{-(3+\varepsilon)}(\Gamma)} \le Ch^2|I|.$$

□

We can now prove the main result of this section.

Theorem 18. Let $\Omega_0\subset\Omega$ be a domain with $\overline{\Omega}_0\subset\Omega$. Then there exists $h_0>0$ and $C>0$ with

$$\|u^h-u\|_{H^1(\Omega_0)/\mathbb{R}} \le Ch^2|I|$$

for $0<h<h_0$ and $I\in\mathbb{R}^L_\diamond$.

Proof. We imposed the same assumptions as in 1.3.1, i.e. σ is smooth near the boundary and Γ is smooth. Since u^h-u solves $\operatorname{div}(\sigma\nabla(u^h-u))=0$ on Ω in the distributional sense we can use the estimate from (1.25), which yields

$$\|u^h-u\|_{H^{-(\frac12+\varepsilon)}(\Omega)/\mathbb{R}} \le C\|\sigma\nabla(u^h-u)\cdot\nu\|_{H^{-(3+\varepsilon)}(\Gamma)}.$$

Now it follows from the previous lemma

$$\|u^h-u\|_{H^{-(\frac12+\varepsilon)}(\Omega)/\mathbb{R}} \le Ch^2|I|. \tag{1.51}$$

We assume that Ω_0 is smooth with $K\subset\Omega_0$, otherwise we can enclose Ω_0 by such a smooth set and prove the theorem for this larger set. K was the compact set in Ω enclosing the non-smooth part of σ. Now u_h-u solves

$$\operatorname{div}(\sigma\nabla(u^h-u))=0 \quad\text{in }\Omega_0,\qquad \sigma\nabla(u^h-u)\cdot\nu = g \quad\text{on }\partial\Omega_0 \tag{1.52}$$

for $g\in L^2(\partial\Omega_0)$ with $\int_{\partial\Omega_0}g\,d\mathcal{H}^2=0$ and $\|g\|_{L^2(\partial\Omega_0)}\le Ch^2|I|$. To see this, note that since $u\in H^1_{\mathrm{loc}}(\Omega)$ we have $\sigma\nabla(u^h-u)\in H(\operatorname{div},\Omega_0)$ with $\operatorname{div}(\sigma\nabla(u^h-u))=0$ on Ω_0. Hence we can use (1.13)

$$0=\int_{\Omega_0}\operatorname{div}(\sigma\nabla(u^h-u))\,dx = \int_{\partial\Omega_0}\sigma\nabla(u^h-u)\cdot\nu\,d\mathcal{H}^2.$$

Further let us choose two smooth auxiliary domains $\Omega_0 \Subset V \Subset \Omega$ and $U \Subset (\Omega \setminus K)$ with $(V \setminus \overline{\Omega}_0) \Subset U$. Then we get

$$\begin{aligned}\|\sigma\nabla(u^h-u)\cdot\nu\|_{L^2(\partial\Omega_0)} &\leq \|\sigma\nabla(u^h-u)\cdot\nu\|_{L^2(\partial(V\setminus\Omega_0))} \leq C\|u^h-u\|_{H^{\frac{3}{2}}(V\setminus\overline{\Omega}_0)/\mathbb{R}} \\ &\leq C\|u^h-u\|_{H^{-(\frac{1}{2}+\varepsilon)}(U)/\mathbb{R}} \leq C\|u^h-u\|_{H^{-(\frac{1}{2}+\varepsilon)}(\Omega)/\mathbb{R}} \leq Ch^2|I|_{\mathbb{R}^L},\end{aligned}$$

where we used the trace theorem for the normal derivative, lemma 9 and (1.51).
Now since $u^h - u$ solves (1.52) we get

$$\begin{aligned}c\|u^h-u\|^2_{H^1(\Omega_0)/\mathbb{R}} &\leq \int_{\Omega_0}\sigma\nabla(u^h-u)\cdot\nabla(u^h-u)\,dx = \langle g, u^h-u\rangle_{L^2(\partial)\Omega_0} \\ &\leq C\|g\|_{L^2(\partial\Omega_0)}\|u^h-u\|_{H^1(\Omega_0)/\mathbb{R}} \leq Ch^2|I|\|u^h-u\|_{H^1(\Omega_0)/\mathbb{R}}.\end{aligned}$$

□

1.4. Finite Element Method

As explicitly solving the previously introduced boundary value problems is far to complicated, if not impossible, one has to try to solve them numerically by approximating the solutions. Let the weak formulation of the problem be given by

$$\text{Find } u \in H \text{ with } a(u,v) = l(v) \quad \forall v \in H, \tag{1.53}$$

where H is a Hilbert space, a bilinear, bounded, symmetric and coercive and l linear and bounded. As we saw earlier the lemma of Lax-Milgram ensures existence and uniqueness of a solution to this problem. Assume $V_h \subset H$ is a finite dimensional subspace, then we can restrict (1.53) to V_h

$$\text{Find } u_h \in V_h \text{ with } a(u_h,v_h) = l(v_h) \quad \forall v_h \in V_h. \tag{1.54}$$

Since V_h is a Hilbert space as well and the restrictions of a and l retain their properties, this problem possesses a unique solution $u_h \in V_h$, which will be our numerical approximation to the initial solution. This method is known as the Ritz-Garlerkin method. Ceá's lemma shows that u_h is the quasi-best approximation we can find in V_h,

$$\|u-u_h\| \leq \frac{C}{c}\inf_{v_h\in V_h}\|u-v_h\|,$$

since for $v_h \in V_h$ we get

$$c\|u-u_h\|^2 \leq a(u-u_h,u-u_h) = a(u-u_h,u-v_h) \leq C\|u-u_h\|\|u-v_h\|.$$

Notice that the Garlerkin orthogonality $a(u-u_h,v_h)=0$ is the key property of this approach. Since V_h is finite dimensional we can fix a basis $\{\varphi_1,\dots\varphi_N\}$ and write $u_h = \sum_{j=1}^N u_h^j\varphi_j$. From (1.54) we derive

$$\sum_{j=1}^N u_h^j a(\varphi_j,\varphi_i) = l(\varphi_i) \quad \forall i = 1\dots N.$$

If we set $A_{i,j} = a(\varphi_j,\varphi_i)$ and $b_i = l(\varphi_i)$, then we have to solve the equation system $Ax = b$. The solution x consists of the coefficients for u_h with respect to the previously chosen basis. Note that since a is symmetric and coercive, the matrix A is symmetric and positive definite.
The new question arising is how to choose the subspace V_h. Therefore we will consider so called finite elements. Following Brenner and Scott (2008); Ciarlet (2002) a finite element is a triple (K,P,N) with

1. $K \subset \mathbb{R}^n$ an open, non-empty, bounded, simply connected set with piecewise smooth-boundary (element domain)
2. $\mathcal{P}$ a k-dimensional space of functions $f : K \to \mathbb{R}$ (shape functions)
3. $\mathcal{N} = \{N_1, \dots N_k\}$ a set of k linear independent linear functionals on $\mathcal{P}$ (nodal variables).

A basis $\{\psi_1 \dots \psi_k\}$ of P with $N_i(\psi_j) = \delta_{ij}$ is called nodal basis for $\mathcal{P}$. Notice that $\mathcal{N}$ determines the elements of $\mathcal{P}$, i.e. if $\varphi_1, \varphi_2 \in \mathcal{P}$ with $N(\varphi_1) = N(\varphi_2)$ for all $N \in \mathcal{N}$, then $\varphi_1 = \varphi_2$.
In order to discretize our problem, we'll subdivide our domain Ω into smaller pieces. A subdivision of $\Omega \subset \mathbb{R}^n$ is a finite set $\{K_1 \dots K_M\}$ of sets satisfying condition 1. from above as well as

$$K_i \cap K_j = \emptyset \quad \text{for } i \neq j \quad \text{and} \quad \bigcup \bar{K}_i = \bar{\Omega}.$$

We obtain a finite number of finite elements with each consisting of a finite dimensional function space, hence the resulting problem will be finite dimensional as well. We assume that $\Omega \subset \mathbb{R}^3$ subdivides into tetrahedrons $\mathcal{T} = \{T_i \dots T_M\}$ with the additional condition

$$\bar{T}_i \cap \bar{T}_j = \emptyset \quad \text{or} \quad \bar{T}_i \cap \bar{T}_j \text{ is a common face of } T_i \text{ and } T_j.$$

We will call $\mathcal{T}$ a triangulation of Ω. We choose first order Lagrange elements, i.e $\mathcal{P}^i$ are polynomials of degree ≤ 1 restricted to T_i and $\mathcal{N}$ is given by point evaluations at the vertices of T_i. We further impose that the functions of V_h are continuous, hence

$$V_h = \{v \in C(\Omega) : v|_{T_i} \in \mathcal{P}_1(T_i) \ \forall i = 1 \dots M\}.$$

Notice that the functions of V_h are determined by their values on the vertices of the triangulation. If we number the vertices $\{x_1, \cdots, x_N\}$, then the functions $\varphi_i \in V_h$ with $\varphi_i(x_j) = \delta_{ij}$ form a basis of V_h and we have

$$v = \sum_{j=1}^{N} v(x_j)\varphi_j. \tag{1.55}$$

With additional requirements on the regularity of the triangulation one can prove inequalities of the form

$$\|u - I_h u\|_{H^1(\Omega)} \leq Ch|u|_{H^2(\Omega)} \qquad \text{and} \qquad \|u - I_h u\|_{L^2(\Omega)} \leq Ch^2|u|_{H^2(\Omega)}$$

for $u \in H^2(\Omega)$, where $I_h : H^2(\Omega) \to V_h$ is the nodal interpolation operator basically given by (1.55) (Brenner and Scott, 2008, Sec. 4.4). Unfortunately we won't have so much regularity, only $u \in H^1(\Omega)$ (or even less in the case of the PEM, which will be a special case anyway). Therefore $u(x_i)$ isn't well defined. In this case one can use a different type of Interpolation operator (Brenner and Scott, 2008, Sec. 4.8) to still get error estimates of the form

$$\|u - \tilde{I}_h u\|_{H^1(\Omega)} \leq C|u|_{H^1(\Omega)} \qquad \text{and} \qquad \|u - \tilde{I}_h u\|_{L^2(\Omega)} \leq Ch|u|_{H^1(\Omega)}. \tag{1.56}$$

It is very likely that one has to drop the assumption that Ω subdivides into tetrahedrons, e.g. when the boundary is curved. One can then try to use other finite elements that adapt better to the shape of Ω or one commits a variational crime and instead solves

$$a_h(u_h, v_h) = l_h(v_h),$$

where v_h, u_h are functions defined on Ω_h, which is only an approximation of Ω, and with a_h, l_h modified accordingly. Other variational crimes are e.g. the usage of quadrature instead of exact integration, non-conformal finite elements or perturbations in the coefficients. One can try to use Strang's lemma, which generalize Ceá's lemma, in order to obtain error estimates (cf. Brenner and Scott, 2008). In our case we will ignore this and simply assume that σ is constant on

each tetrahedron and that Ω subdivides into tetrahedrons.

Recall that we already derived weak formulations for the continuum model and the complete electrode model. For the CM we get

$$A_{i,j} = a(\varphi_j, \varphi_i) = \int_\Omega \sigma \nabla \varphi_j \cdot \nabla \varphi_i \, dx \quad \text{and} \quad b_i = l(\varphi_i) = \langle f, \varphi_i \rangle.$$

and the corresponding equation system is $Ax = b$ as mentioned earlier. For the CEM this is a bit more complicated. We denote by e_m the mth standard unit vector in $\mathbb{R}^L$. Since this time we are looking for solutions in the space $H^1(\Omega) \oplus \mathbb{R}^L$ our discritized function space is $V_h \oplus \mathbb{R}^l$. Therefore our basis is given by

$$(\varphi_i, 0) \in V_h \oplus \mathbb{R}^l \text{ with } \varphi_i(x_j) = \delta_{ij}, \quad i = 1 \dots N,$$

and

$$(0, e_m) \in V_h \oplus \mathbb{R}^l, \quad m = 1 \dots L.$$

Let us set

$$\begin{aligned}
A_{i,j} = a((\varphi_j, 0), (\varphi_i, 0)) &= \int_\Omega \sigma \nabla \varphi_j \cdot \nabla \varphi_i \, dx + \sum_{m=1}^{L} \frac{1}{z_m} \int_{e_m} \varphi_j \varphi_i \, d\mathcal{H}^2 \\
B_{i,m} = a((0, e_m), (\varphi_i, 0)) &= -\frac{1}{z_m} \int_{e_m} \varphi_i \, d\mathcal{H}^2 \\
C_{k,m} = a((0, e_m), (0, e_k)) &= \frac{|e_m|}{z_m} \delta_{m,k}.
\end{aligned}$$

The resulting equation system is

$$M \begin{pmatrix} x_1 \\ x_2 \end{pmatrix} = \begin{pmatrix} A & B \\ B^T & C \end{pmatrix} \begin{pmatrix} x_1 \\ x_2 \end{pmatrix} = \begin{pmatrix} 0 \\ I \end{pmatrix}$$

where $x_1 \in \mathbb{R}^N$ consists of the coefficients for u_h and $x_2 = U \in \mathbb{R}^L$. This can be solved using the Schur complement $S = C - B^T A^{-1} B$, i.e.

$$x_2 = S^{-1} I \quad \text{and} \quad x_1 = -A^{-1} B x_2 = -A^{-1} B S^{-1} I. \tag{1.57}$$

Notice that even though in both cases A and in the CEM also M are symmetric, they are only positive semi definite and not invertible. This is due to the fact, that the potential is only unique up to an additive constant. Hence their null spaces are of the form $\mathbb{R} \cdot (1, \dots, 1)^T$. We can overcome this by removing one degree of freedom. Let us replace the ith row and column of A by 0, $A_{i,i} = 1$ and furthermore the ith component of the right hand side by 0. In the case of CEM, we also have to replace the ith row of B by 0. Then A and M are symmetric, positive definite and we obtain the unique solution with $u(x_i) = 0$. A more detailed explanation can be found in Höltershinken (2021), which discusses the CM, but can be directly transferred to the CEM. Note that if A and M are both positive definite, then the Schur complement is positive definite as well (Boyd and Vandenberghe, 2004, A.5.5) and hence (1.57) is valid.
For the PEM we couldn't derive a formulation like (1.53), we could only interpret the PDE in the sense of distributions and the boundary condition in the trace sense. Let us denote the electrode positions by $\tilde{x}_m$, $m = 1, \dots, L$. By formally applying the divergence theorem we get

$$\int_\Omega \sigma \nabla u \nabla v \, d = \sum_{m=1}^{L} I_m v(\tilde{x}_m).$$

This motivates our discretization

$$\text{Find } u_h \in V_h \text{ with } \int_\Omega \sigma \nabla u_h \nabla v_h \, d = \sum_{m=1}^{L} I_m v_h(\tilde{x}_m) \quad \forall v_h \in V_h. \tag{1.58}$$

Notice that since v_h is continuous, point evaluations are well defined. As already mentioned earlier, since V_h is a finite dimensional subspace of $H^1(\Omega)$, it is closed and hence a Hilbert space as well. We already showed, that the bilinearform a is bounded and coercive on $H^1(\Omega)/\mathbb{R}$, hence the same is true for the restriction to $V_h/\mathbb{R}$. Let us denote $f = \sum_{m=1}^{L} I_m \delta_{\tilde{x}_m}$. For $I \in \mathbb{R}^L_\diamond$ this functional is well defined on $V_h/\mathbb{R}$. Obviously $f : V_h/\mathbb{R} \to \mathbb{R}$ is linear and because V_h is finite dimensional, it is continuous. We can apply the lemma of Lax-Milgram, which proves existence and uniqueness of a solution for (1.58). The system matrix for the PEM is the same as for the CM, as the bilinearforms are identical. If we choose the electrodes to be located on vertices, then we get

$$b_i = \begin{cases} I_i, & \text{if } x_i \in \{\tilde{x}_1 \dots \tilde{x}_L\} \\ 0, & \text{else.} \end{cases}$$

Details on assembly of the system matrices, especially for the CEM, can be found in Crabb (2017). Typically one does not iterate over the indices i, j, but over the elements of the subdivision. Notice that since the functions φ_i are only supported on the adjoining elements to the corresponding vertex, the matrices defined above are sparse. For more information on how to solve the resulting equation systems we refer to Höltershinken (2021).
Note that we always considered quotient spaces in order to get uniqueness results. We can bypass this by restricting ourselves to the subspace of functions with zero mean, i.e. with $\langle u, 1\rangle = 0$. Each equivalence class has exactly one such representative and if we set $u_\Omega = \frac{1}{|\Omega|}\int_\Omega u \, dx$ we obtain

$$\|u - u_\Omega\|_{L^2(\Omega)} \le C\|\nabla u\|_{L^2(\Omega)} = C\|\nabla(u-c)\|_{L^2(\Omega)} \le C\|u-c\|_{H^1(\Omega)} \quad \forall c \in \mathbb{R},$$

by Poincaré inequality. Hence

$$\|u - u_\Omega\|_{H^1(\Omega)} \le C\|u\|_{H^1(\Omega)/\mathbb{R}}.$$

One can prove a similar result as the Poincaré inequality for $H^s(\Omega)$ with $s \in (0,1)$, we refer to Drelichman and Durán (2018). Note that it even holds $\|u - u_\Omega\|_{H^1(\Omega)} = \|u\|_{H^1(\Omega)/\mathbb{R}}$, as in Hilbert spaces H/V is isometrically isomorphic to $V^\perp$ and in our case $\mathbb{R}^\perp$ are exactly the functions with zero mean.
We already stated some general error estimates earlier (1.56). They can be applied to the CM and moreover to the CEM, since

$$\inf_{\substack{v_h \in V_h, \\ V^h \in \mathbb{R}^L}} \|(u,U) - (v_h, V^h)\|^2_{\mathcal{H}} = \inf_{\substack{v_h \in V_h, \\ V^h \in \mathbb{R}^L}} \|u - v_h\|^2_{H^1(\Omega)} + |U - V^h|^2 \le \inf_{v_h \in V_h} \|u - v_h\|^2_{H^1(\Omega)}.$$

For the CEM we can strengthen the convergence results. Under the assumption of $\sigma \in C^\infty(\bar{\Omega}, \mathbb{R}^{3\times 3})$ one can show $u \in H^{\frac{3}{2}+s}(\Omega)$ and obtain

$$\|u - u_h\|_{H^1(\Omega)} \le Ch^{\frac{1}{2}+s} \quad \text{and} \quad \|u - u_h\|_{L^2(\Omega)} \le Ch^{1+2s}$$

for $s \in (0, \frac{1}{2})$ (Crabb, 2017; Dardé and Staboulis, 2016). The FEM approximation of the PEM is not expected to converge to the real solution in the L^2-norm. However according to (Crabb, 2017) due to elliptic regularity, one can expect convergence in the H^1- and L^2-norm in the interior of Ω away from the boundary .

1.5. Analytical Solutions for the Multilayer Sphere Model

In section 1.6 we want to verify our FEM solutions for the point electrode model and the complete electrode model in the controlled environment of a multilayer sphere model with isotropic conductivity. Therefore we want to derive analytical solutions in this section. The basic idea is to find functions which solve the PDE and to combine them into a series, such that the boundary conditions are satisfied as well. Since these solutions will be series expansions and we have to truncate them in order to calculate them, the term semi-analytical actually suits better.
The multilayer sphere model consists of N concentric spherical shells with radii given by $0 = r_0 < \cdots < r_N$. We'll denote the (interior of the) shells by $K_n = \{x \in \mathbb{R}^3 : r_{n-1} < \|x\| < r_n\}$. Further we assume that the conductivity is constant on each layer and $\sigma_n = \sigma|_{K_n} \in \mathbb{R}_{>0}$. In cartesian coordinates the Lapace operator on $\mathbb{R}^d$ is defined $\Delta = \sum_{i=1}^{d} \frac{\partial^2}{\partial x_i^2}$. More general for Riemannian manifolds one can define the Laplace-Beltrami operator in local coordinates by

$$\Delta u = \frac{1}{\sqrt{|g|}} \sum_{i,j} \frac{\partial}{\partial x_i}\Big(g^{ji}\sqrt{|g|}\frac{\partial u}{\partial x_j}\Big),$$

where $|g|$ is the absolute value of the determinant of the metric tensor and g^{ij} are the components of the inverse metric tensor. Using polar coordinates $(r, \xi) \in \mathbb{R}_{>0} \times \mathbb{S}^{d-1}$, we can derive

$$\Delta u = \frac{1}{r^{d-1}} \frac{\partial}{\partial r}\Big(r^{d-1}\frac{\partial u}{\partial r}\Big) + \frac{1}{r^2}\Delta_{\mathbb{S}^{d-1}} u,$$

where $\Delta_{\mathbb{S}^{d-1}}$ is the Laplace-Beltrami operator on $\mathbb{S}^{d-1}$. If we extend $f : \mathbb{S}^{d-1} \to \mathbb{R}$ by $f^*(x) = f(\frac{x}{\|x\|})$, then $\Delta f^*|_{\mathbb{S}^{d-1}} = \Delta_{\mathbb{S}^{d-1}} f$ (Shubin, 2001, Prop. 22.1).
The next results are taken from Atkinson and Han (2012). Even tough they deal with complex polynomials and functions, the results also hold for the real case. Let us denote the set of all homogeneous polynomials of degree n on $\mathbb{R}^d$ by $\mathbb{H}_n^d$, i.e. all polynomials of the form

$$\sum_{|\alpha|=n} a_\alpha x^\alpha.$$

The space of homogeneous harmonics of degree n in d dimensions, $\mathbb{Y}_n(\mathbb{R}^d)$, is the subspace of all harmonic polynomials in $\mathbb{H}_n^d$. We further define the spherical harmonic space of order n in d dimensions by $\mathbb{Y}_n^d = \mathbb{Y}_n(\mathbb{R}^d)|_{\mathbb{S}^{d-1}}$. By definition every spherical harmonic $Y_n \in \mathbb{Y}_n^d$ is related to a homogeneous harmonic $H_n \in \mathbb{Y}_n(\mathbb{R}^d)$ by

$$H_n(r\xi) = r^n Y_n(\xi) \quad r \in \mathbb{R}_{\geq 0},\ \xi \in \mathbb{S}^{d-1}.$$

For $m \neq n$ it holds $\mathbb{Y}_m^d \perp \mathbb{Y}_n^d$ in $L^2(\mathbb{S}^{d-1})$. Furthermore one can prove the orthogonal decomposition

$$L^2(\mathbb{S}^{d-1}) = \bigoplus_{n=0}^{\infty} \mathbb{Y}_n^d. \tag{1.59}$$

Let $Y_n \in \mathbb{Y}_n^d$ and set $Y_n(x) = Y_n(r\xi) = r^n Y_n(\xi)$. Then $Y_n \in \mathbb{Y}^n(\mathbb{R}^d)$ and hence

$$0 = \Delta Y_n(x) = \Big(\frac{1}{r^{d-1}}\frac{\partial}{\partial r}\Big(r^{d-1}\frac{\partial}{\partial r}\Big) + \frac{1}{r^2}\Delta_{S^{d-1}}\Big) r^n Y_n(\xi)$$

i.e.

$$\Delta_{\mathbb{S}^{d-1}} Y_n(\xi) = -n(n+d-2)Y_n(\xi).$$

Therefore we can define fractional powers of the Laplace-Beltrami operators straightforward. This is possible on general compact Riemannian manifolds (Berard, 1986, p.53). Now we can give a more intrinsic definition of the spaces $H^s(\Gamma)$ as shown in Lions and Magenes (1972,

Remark 7.6). Let $(w_j)_j$ be an orthonormal basis of $L^2(\Gamma)$ consisting of eigenfunctions of $-\Delta_\Gamma$ with corresponding eigenvalues λ_j, then

$$H^s(\Gamma) = \{u \in \mathcal{D}'(\Gamma) : \sum_{j=1}^{\infty} \lambda_j^{2s} |\langle u, w_j \rangle|^2 < \infty\} \tag{1.60}$$

with equivalent norm

$$\|u\|^2_{H^s(\Gamma)} = \sum_{j=1}^{\infty} (1 + \lambda_j^2)^s |\langle u, w_j \rangle|^2.$$

Hence we are interested in finding an orthonormal basis for each $\mathbb{Y}_n^d$. We start with defining the Legendre polynomials by

$$P_{n,d}(t) = n!\,\Gamma\left(\frac{d-1}{2}\right) \sum_{k=0}^{\lfloor n/2 \rfloor} (-1)^k \frac{(1-t^2)^k t^{n-2k}}{4^k k!(n-2k)!\,\Gamma\left(k + \frac{d-1}{2}\right)}, \quad t \in [-1, 1]\,.$$

$P_{n,3}$ are the standard Legendre polynomials. We can use Rodrigues representation formula for $d \geq 2$

$$P_{n,d}(t) = (-1)^n R_{n,d} (1-t^2)^{\frac{3-d}{2}} \left(\frac{d}{dt}\right)^n (1-t^2)^{n+\frac{d-3}{2}} \quad \text{with } R_{n,d} = \frac{\Gamma(\frac{d-1}{2})}{2^n \Gamma(n + \frac{d-1}{2})}.$$

The Legendre polynomials solve the so called Legendre's differential equation. One can show that for fixed d they are orthogonal with respect to the L^2 inner product weighted with $(1-t^2)^{\frac{d-3}{2}}$. Further they fulfill a number of recursions and identities that we will not further discuss. We refer to Atkinson and Han (2012). For $d = 3$ we get

$$P_{n,3}(t) = \frac{1}{2^n n!} \left(\frac{d}{dt}\right)^n (t^2 - 1)^n.$$

Next we introduce the associated Legendre functions, sometimes called associated Legendre polynomials, even tough they aren't polynomials in general. We define

$$P_{n,d,j}(t) = \frac{(n+d-3)!}{(n+j+d-3)!} (1-t^2)^{\frac{j}{2}} P_{n,d}^{(j)}(t),$$

where $P_{n,d}^{(j)}$ denotes the jth derivative of $P_{n,d}$. This isn't the definition used in Atkinson and Han (2012) but rather a theorem that holds. We see that these functions are polynomials in t if and only if j is even. For the $d = 3$ we get

$$P_{n,3,j}(t) = \frac{n!}{(n+j)!} (1-t^2)^{\frac{j}{2}} P_{n,3}^{(j)}(t). \tag{1.61}$$

The definition from Atkinson and Han (2012) slightly differs in scaling from other common definitions, e.g. $P_{n,3,j}(t)$ is oft defined as $(-1)^j (1-t^2)^{\frac{j}{2}} P_{n,3}^{(j)}(t)$. But since we will normalize these functions anyway, this has no effect for us. Further note that we omit the Condon–Shortley phase factor $(-1)^j$, which is typically included in the quantum mechanics community. The associated Legendre functions satisfy the general Legendre equation. Furthermore for fixed d and j they are orthogonal with respect to the weighted L^2 inner product defined above. We want to normalize these functions with regards to the weighted inner product. For $d = 3$ ones can derive

$$\tilde{P}_{n,3,j}(t) = \left(\frac{(n+\frac{1}{2})(n-j)!}{(n+j)!}\right)^{\frac{1}{2}} (1-t^2)^{\frac{j}{2}} P_{n,3}^{(j)}(t).$$

Notice that $(1-t^2)^{\frac{j}{2}} P_{n,3}^{(j)}(t)$ is the common defintion for associated Legendre functions mentioned above. With these normalized asssociated Legendre functions it is possible to construct an orthonormal basis for $\mathbb{Y}_n^d$, based on a given orthonormal basis of $\mathbb{Y}_n^{d-1}$. If

$$\{Y_{m,d-1,j} : 1 \le j \le N_{m,d-1}\}$$

is an orthonormal basis of $\mathbb{Y}_n^{d-1}$, $0 \le m \le n$, then we can construct one for $\mathbb{Y}_n^d$ by

$$\{\tilde{P}_{n,d,m}(t) Y_{m,d-1,j}(\xi_{(d-1)}) : 1 \le j \le N_{m,d-1}, 0 \le m \le n\},$$

where $(t, \xi_{(d-1)}) \in [-1,1] \times \mathbb{S}^{d-1}$ are coordinates for $\mathbb{S}^d$, i.e $(t, \xi_{(d-1)}) \mapsto t e_d + \sqrt{1-t^2}\xi_{(d-1)}$. For $\mathbb{S}^2$ we use $t = \cos\theta$, $0 \le \theta \le \pi$, and $\xi_{(2)} = (\cos\varphi, \sin\varphi)^T$ for $0 \le \varphi < 2\pi$. Then a orthonormal basis for $\mathbb{Y}_m^2$ is given by

$$\{Y_{m,2,1}(\xi_{(2)}) = \frac{1}{\sqrt{\pi}}\cos(m\varphi),\ Y_{m,2,2}(\xi_{(2)}) = \frac{1}{\sqrt{\pi}}\sin(m\varphi)\},$$

if $m \ge 1$ and for $m = 0$ by $\frac{1}{\sqrt{2\pi}}$. Hence the desired basis for $d = 3$ is given by

$$Y_{l,3,m}(\theta,\varphi) = \begin{cases} \left(\frac{(2l+1)(l-m)!}{2\pi(l+m)!}\right)^{\frac{1}{2}} (\sin\theta)^m P_{l,3}^{(m)}(\cos\theta)\cos(m\varphi) & \text{for } 1 \le m \le l \\ \left(\frac{(2l+1)}{4\pi}\right)^{\frac{1}{2}} P_{l,3}(\cos\theta) & \text{for } m = 0 \\ \left(\frac{(2l+1)(l-|m|)!}{2\pi(l+|m|)!}\right)^{\frac{1}{2}} (\sin\theta)^{|m|} P_{l,3}^{(|m|)}(\cos\theta)\sin(|m|\varphi) & \text{for } -l \le m \le -1. \end{cases} \tag{1.62}$$

We will fix this basis and only write $Y_{l,m}$. By definition $r^l Y_{l,m}$ is harmonic. The same is true for $r^{-(l+1)}Y_{l,m}$. Recall, $Y_{l,m}$ is an eigenfunction of the Laplace-Beltrami operator with eigenvalue $-l(l+1)$. Hence for $r > 0$

$$\begin{aligned} \Delta\left(r^{-(l+1)}Y_{l,m}\right) &= \left(\frac{1}{r^2}\frac{\partial}{\partial r}\left(r^2\frac{\partial}{\partial r}\right) + \frac{1}{r^2}\Delta_2^*\right) r^{-(l+1)} Y_l(\xi) = \left(\frac{2}{r}\frac{\partial}{\partial r} + \frac{\partial^2}{\partial r^2} + \frac{1}{r^2}\Delta_2^*\right) r^{-(l+1)} Y_{l,m} \\ &= (-2(l+1) + (l+1)(l+2) - l(l+1)) r^{-(l+3)} Y_{l,m} = 0. \end{aligned}$$

1.5.1. Complete Electrode Model

We want to derive a solution for the complete electrode model. Even though there are solution for the CEM in three dimensions (Pidcock et al., 1995a,b), they omit the condition $\int_{e_m} \sigma \nabla u \cdot \nu \, d\mathcal{H}^2 = I_m$ and only impose normal Robin boundary conditions. Somersalo et al. (1992) derived a solution for the two dimensional case with equidistant electrodes and some specific current patterns. We will come back to this later.

Theorem 19. If $u \in H^1(\Omega)$ solves $\operatorname{div}(\sigma\nabla u) = 0$ on the multilayer sphere model, then we can find unique coefficients $(A_{l,m}^{(n)})_{l,m}, (B_{l,m}^{(n)})_{l,m} \in \ell^2$ for $1 \le n \le N,\ m \in \mathbb{N}_0, l = -m, \dots, m$, such that

$$u(x) = \sum_{l=0}^{\infty}\sum_{m=-l}^{l} \left[A_{l,m}^{(n)} r^l + B_{l,m}^{(n)} r^{-(l+1)}\right] Y_{l,m}(\xi) \quad \text{for } r_{n-1} < |x| < r_n, \tag{1.63}$$

where the sum converges in $H^1(\Omega)$.

From now on we will abbreviate $\sum_{l,m} = \sum_{l=0}^{\infty}\sum_{m=-l}^{l}$.

Proof. Denote the series by $\tilde{u}$. It suffices to show that we can find coefficients for each layer K_n, such that $\tilde{u}|_{K_n}$ converges to u in $H^1(K_n)$ and that $\tilde{u}|_{\bar{K}_n \cap r_n \mathbb{S}^2} = \tilde{u}|_{\bar{K}_{n-1} \cap r_n \mathbb{S}^2}$. Then we can deduce for $\varphi \in \mathcal{D}(\Omega)$

$$\int_\Omega \tilde{u} D^i \varphi \, dx = \sum_{n=1}^N \int_{K_n} \tilde{u} D^i \varphi \, dx = \sum_{n=1}^N \int_{\partial K_n} \tilde{u} \varphi n_i \, d\mathcal{H}^2 - \int_{K_n} D^i \tilde{u} \varphi \, dx = - \int_\Omega D^i \tilde{u} \varphi \, dx,$$

i.e. $\tilde{u} \in H^1(\Omega)$ and $\tilde{u} = u$ in $H^1(\Omega)$. Now if $\tilde{u}$ converges in $H^1(K_n)$ and the restrictions of u and $\tilde{u}$ to ∂K_n agree, then $u = \tilde{u}$ on K_n. To be more precise, both solve $\operatorname{div}(\sigma \nabla v) = 0$, u by assumption and $\tilde{u}$ by construction and since the solution of this boundary value problem with the Dirichlet boundary condition is unique, we derive $u = \tilde{u}$ on K_n. We assume that $n > 1$. Without loss of generality, we can assume $K_n = \{x \in \mathbb{R}^3 : R < \|x\| < 1\}$ with $R \in (0,1)$. Since $u \in H^1(K_n)$, the trace theorem yields $u|_{R\mathbb{S}^2} \in H^{\frac{1}{2}}(R\mathbb{S}^2)$ and $u|_{\mathbb{S}^2} \in H^{\frac{1}{2}}(\mathbb{S}^2)$. From (1.60) and (1.59) we know there exist unique $(\alpha_{l,m})_{l,m}, (\beta_{l,m})_{l,m} \in \ell^2$ with

$$\sum_{l,m} (1 + l^2(l+1)^2)^{\frac{1}{2}} \alpha_{l,m}^2 < \infty \quad \text{and} \quad \sum_{l,m} (1 + l^2(l+1)^2)^{\frac{1}{2}} \beta_{l,m}^2 < \infty \tag{1.64}$$

and

$$u|_{R\mathbb{S}^2} = \sum_{l,m} \alpha_{l,m} Y_{l,m} \quad \text{and} \quad u|_{\mathbb{S}^2} = \sum_{l,m} \beta_{l,m} Y_{l,m}.$$

We will drop the superscripts (n) for the following calculations. Since $Y_{l,m}$ are orthonormal we deduce

$$\alpha_{l,m} = A_{l,m} R^l + B_{l,m} R^{-(l+1)} \quad \text{and} \quad \beta_{l,m} = A_{l,m} + B_{l,m}.$$

Hence

$$A_{l,m} = \frac{\alpha_{l,m} R^{l+1} - \beta_{l,m}}{R^{2l+1} - 1} \quad \text{and} \quad B_{l,m} = \frac{\beta_{l,m} R^{2l+1} - \alpha_{l,m} R^{l+1}}{R^{2l+1} - 1}.$$

Since $0 < R < 1$ is fixed, we get $|R^{2l+1} - 1| \geq |R - 1|$ and hence there exists $C > 0$ independent of l, m with

$$A_{l,m}^2 \leq C(\alpha_{l,m}^2 + \beta_{l,m}^2) \quad \text{and} \quad B_{l,m}^2 \leq C(\alpha_{l,m}^2 + \beta_{l,m}^2) R^{2l+2}.$$

We can plug this in and obtain

$$\begin{aligned}
\int_{K_n} |\tilde{u}|^2 \, dx &= \int_R^1 \int_{\mathbb{S}^2} \left(\sum_{l,m} (A_{l,m} r^l + B_{l,m} r^{-(l+1)}) Y_{l,m}(\xi) \right)^2 r^2 \, d\mathcal{H}^2(\xi) \, dr \\
&= \int_R^1 \sum_{l,m} \left(A_{l,m} r^l + B_{l,m} r^{-(l+1)} \right)^2 r^2 dr \leq 2 \int_R^1 \sum_{l,m} A_{l,m}^2 r^{2l+2} + B_{l,m}^2 r^{-2l} dr \\
&\leq 2C \sum_{l,m} \frac{(1 - R^{2l+3})}{2l+3} (\alpha_{l,m}^2 + \beta_{l,m}^2) + \frac{1}{|2l-1|} (R^{2l+2} - R^3)(\alpha_{l,m}^2 + \beta_{l,m}^2).
\end{aligned}$$

Thus the partial sums of $\tilde{u}$ are a Cauchy sequence in $L^2(K_n)$ and hence $\tilde{u} \in L^2(K_n)$ converges. Next we will consider $\nabla \tilde{u}$. On a Riemannian manifold the gradient in local coordinates is given by

$$\nabla u = \sum_{i,j} g^{i,j} \frac{\partial u}{\partial x_i} \frac{\partial}{\partial x_j}.$$

Let ∇ denotes the gradient on $\mathbb{R}^d$ and $\nabla_{\mathbb{S}^{d-1}}$ the gradient on $\mathbb{S}^{d-1}$. For polar coordinates $(r, \xi) \in \mathbb{R}_{>0} \times \mathbb{S}^{d-1}$ one can derive

$$\nabla u = \frac{\partial u}{\partial r} \xi + \frac{1}{r} \nabla_{\mathbb{S}^{d-1}} u, \tag{1.65}$$

with $\|\xi\| = 1$ and $\xi \perp \nabla_{\mathbb{S}^2} u$. Notice that by the divergence theorem for compact Riemannian manifolds (Lee, 2012, Thm 16.32 & 16.48)

$$\int_{\mathbb{S}^2} \nabla_{\mathbb{S}^2} Y_{k,s} \cdot \nabla_{\mathbb{S}^2} Y_{l,m} \, d\mathcal{H}^2 = \int_{\mathbb{S}^2} Y_{k,s}(-\Delta_{\mathbb{S}^2}) Y_{l,m} \, d\mathcal{H}^2 = \int_{\mathbb{S}^2} Y_{k,s} Y_{l,m} l(l+1) \, d\mathcal{H}^2 = l(l+1)\delta_{l,k}\delta_{m,s}. \tag{1.66}$$

We can use this together with $\xi \perp \nabla_{\mathbb{S}^2} Y_{l,m}$ in order to derive

$$\begin{aligned}
\int_{K_n} |\nabla \tilde{u}|^2 \, dx &= \int_R^1 \int_{\mathbb{S}^2} \left| \nabla \sum_{l,m} (A_{l,m} r^l + B_{l,m} r^{-(l+1)}) Y_{l,m}(\xi) \right|^2 r^2 \, d\mathcal{H}^2(\xi) \, dr \\
&= \int_R^1 \int_{\mathbb{S}^2} \left| \sum_{l,m} (A_{l,m} l r^l - B_{l,m}(l+1) r^{-(l+1)}) Y_{l,m}(\xi) \xi + \sum_{l,m} (A_{l,m} r^l + B_{l,m} r^{-(l+1)}) \nabla_{\mathbb{S}^2} Y_{l,m}(\xi) \right|^2 d\mathcal{H}^2(\xi) \, dr \\
&= \int_R^1 \int_{\mathbb{S}^2} \left[\sum_{l,m} (A_{l,m} l r^l - B_{l,m}(l+1) r^{-(l+1)}) Y_{l,m}(\xi) \right]^2 + \left| \sum_{l,m} (A_{l,m} r^l + B_{l,m} r^{-(l+1)}) \nabla_{\mathbb{S}^2} Y_{l,m}(\xi) \right|^2 d\mathcal{H}^2(\xi) \, dr \\
&= \int_R^1 \sum_{l,m} \left(A_{l,m} l r^l - B_{l,m}(l+1) r^{-(l+1)} \right)^2 + \left(A_{l,m} r^l + B_{l,m} r^{-(l+1)} \right)^2 l(l+1) dr \\
&\leq 2 \int_R^1 \sum_{l,m} A_{l,m}^2 l(2l+1) r^{2l} + B_{l,m}^2 (l+1)(2l+1) r^{-(2l+2)} dr \\
&= 2 \sum_{l,m} l A_{l,m}^2 (1 - R^{2l+1}) + (l+1) B_{l,m}^2 (R^{-(2l+1)} - 1).
\end{aligned}$$

Looking at one specific summand we get

$$l A_{l,m}^2 (1 - R^{2l+1}) + (l+1) B_{l,m}^2 (R^{-(2l+1)} - 1) \leq C l (1 - R^{2l+1})(\alpha_{l,m}^2 + \beta_{l,m}^2) + (l+1) C (\alpha_{l,m}^2 + \beta_{l,m}^2)(R - R^{2l+2}).$$

With (1.64) we therefore see, that the partial sums of $\tilde{u}$ are a Cauchy sequence in $H^1(K_n)$. By construction $\tilde{u}$ and u agree on the boundary of K_n, thus we get the desired result. We assumed $n > 1$ so far, notice that for $n = 1$ we necessarily have $B_{l,m}^{(1)} = 0$. This simplifies the above calculations, which we won't carry out again. □

It now arises the question how to calculate these coefficients. According to Gilbarg and Trudinger (2001, Thm. 8.24) the solution u is continuous at the inner layer boundaries. Moreover it is continuous away from the outer boundary of Ω. This is our first inner transition condition. Furthermore the current density normal to the layer boundary, $\sigma \nabla u \cdot \nu$, is continuous as well. To see this, denote an inner layer interface of two shells K_i and K_j by Λ and choose a point $x \in \Lambda$. Let B be a small open ball centered at x, such that $B_i = B \cap K_i$ and $B_j = B \cap K_j$ are connected. We denote the restrictions of u and σ to B_i resp. B_j by subscripts i, j. Let $\varphi \in \mathcal{D}(B)$ be arbitrary. Then we get

$$0 = \int_\Omega \sigma \nabla u \cdot \nabla \varphi \, dx = \int_{B_i} \sigma_i \nabla u_i \cdot \nabla \varphi \, dx + \int_{B_j} \sigma_j \nabla u_j \cdot \nabla \varphi \, dx.$$

From Lemma 9 we know that u_i and u_j are smooth, and by choosing test functions supported in B_i resp. B_j, we deduce that u_i and u_j are harmonic. With the divergence theorem we can derive

$$0 = -\int_{B_j} \sigma_j \Delta u_j \varphi \, d - \int_{B_i} \sigma_i \Delta u_i \varphi \, d + \int_{\Lambda \cap B} (\sigma_j \nabla u_j - \sigma_i \nabla u_i) \cdot \nu \varphi \, d\mathcal{H}^2 = \int_{\Lambda \cap B} (\sigma_j \nabla u_j - \sigma_i \nabla u_i) \cdot \nu \varphi \, d\mathcal{H}^2.$$

Therefore $\sigma_i \nabla u_i \cdot \nu = \sigma_j \nabla u_j \cdot \nu$ a.e. on $\Lambda \cap B$ and since both functions are continuous, we get the equality everywhere on $\Lambda \cap B$. Notice this is also true if the layer interfaces aren't spheres,

but only smooth. For each pair (l,m) we need to determine $2N-1$ coefficients. We have $2N-2$ transition conditions and the outer boundary condition. As done in Somersalo et al. (1992); Ferree et al. (2000) we will rescale the representation (1.63) in order to prevent numerical under or overflow

$$u(x) = \sum_{l=0}^{\infty} \sum_{m=-l}^{l} \left[A_{l,m}^{(n)} \left(\frac{r}{r_n} \right)^l + B_{l,m}^{(n)} \left(\frac{r}{r_n} \right)^{-(l+1)} \right] Y_{l,m}(\xi) \quad \text{for } r_{n-1} < |x| < r_n. \tag{1.67}$$

As mentioned earlier Somersalo et al. (1992) derived the solution for the two dimensional case with equidistant electrodes and some specific current patterns. They reformulate the weak formulation into a minimization problem. The optimizer of the resulting problem then consists of the desired coefficients for the series expansion. By truncating the problem, they reduce it to a finite dimensional minimization problem, which can be solved by solving a linear equation system. We will proceed slightly different and use a Garlerkin approach, where the finite dimensional subspace is now given by a finite set of summands from the series expansion. This approach directly provides the proof that our semi-analytical solution converges towards the real solution. In the end, both approaches yield the same approximation.
First notice that $\sigma \nabla u \cdot \nu = \sigma \frac{\partial u}{\partial r}$. We will focus on the layer interface at $r = r_n$, $1 \le n < N$ and fix a pair (l,m). The transition conditions yield for each pair (l,m) a system of two equations

$$A_{l,m}^{(n+1)} \left(\frac{r_n}{r_{n+1}} \right)^l + B_{l,m}^{(n+1)} \left(\frac{r_n}{r_{n+1}} \right)^{-(l+1)} = A_{l,m}^{(n)} + B_{l,m}^{(n)}$$

$$\sigma^{(n+1)} A_{l,m}^{(n+1)} \left(\frac{r_n}{r_{n+1}} \right)^{l-1} \frac{l}{r_{n+1}} - \sigma^{(n+1)} B_{l,m}^{(n+1)} \left(\frac{r_n}{r_{n+1}} \right)^{-(l+2)} \frac{(l+1)}{r_{n+1}} = \sigma^{(n)} A_{l,m}^{(n)} \frac{l}{r_n} - \sigma^{(n)} B_{l,m}^{(n)} \frac{(l+1)}{r_n}.$$

We can solve this and derive

$$(2l+1) A_{l,m}^{(n+1)} = \left(l + 1 + l \frac{\sigma^{(n)}}{\sigma^{(n+1)}} \right) \left(\frac{r_n}{r_{n+1}} \right)^{-l} A_{l,m}^{(n)} + (l+1) \left(1 - \frac{\sigma^{(n)}}{\sigma^{(n+1)}} \right) \left(\frac{r_n}{r_{n+1}} \right)^{-l} B_{l,m}^{(n)}$$

$$(2l+1) B_{l,m}^{(n+1)} = l \left(1 - \frac{\sigma^{(n)}}{\sigma^{(n+1)}} \right) \left(\frac{r_n}{r_{n+1}} \right)^{l+1} A_{l,m}^{(n)} + \left(l + (l+1) \frac{\sigma^{(n)}}{\sigma^{(n+1)}} \right) \left(\frac{r_n}{r_{n+1}} \right)^{l+1} B_{l,m}^{(n)}.$$

We can combine this in a matrix

$$F_l^{(n)} = \begin{pmatrix} \left(l + 1 + l \frac{\sigma^{(n)}}{\sigma^{(n+1)}} \right) \left(\frac{r_n}{r_{n+1}} \right)^{-l} & (l+1) \left(1 - \frac{\sigma^{(n)}}{\sigma^{(n+1)}} \right) \left(\frac{r_n}{r_{n+1}} \right)^{-l} \\ l \left(1 - \frac{\sigma^{(n)}}{\sigma^{(n+1)}} \right) \left(\frac{r_n}{r_{n+1}} \right)^{l+1} & \left(l + (l+1) \frac{\sigma^{(n)}}{\sigma^{(n+1)}} \right) \left(\frac{r_n}{r_{n+1}} \right)^{l+1} \end{pmatrix} \frac{1}{2l+1}$$

i.e.

$$\begin{pmatrix} A_{l,m}^{(n+1)} & B_{l,m}^{(n+1)} \end{pmatrix}^T = F_l^{(n)} \begin{pmatrix} A_{l,m}^{(n)} & B_{l,m}^{(n)} \end{pmatrix}^T.$$

We recursively define

$$\begin{pmatrix} \alpha_l^{(1)} & \beta_l^{(1)} \end{pmatrix}^T = \begin{pmatrix} 1 & 0 \end{pmatrix}^T \quad \text{and} \quad \begin{pmatrix} \alpha_l^{(n+1)} & \beta_l^{(n+1)} \end{pmatrix}^T = F_l^{(n)} \begin{pmatrix} \alpha_l^{(n)} & \beta_l^{(n)} \end{pmatrix}^T.$$

By induction one can easily verify

$$\begin{pmatrix} A_{l,m}^{(n)} & B_{l,m}^{(n)} \end{pmatrix}^T = A_{l,m}^{(1)} \begin{pmatrix} \alpha_l^{(n)} & \beta_l^{(n)} \end{pmatrix}^T. \tag{1.68}$$

If we now set $C_{l,m} = A_{l,m}^{(N)} + B_{l,m}^{(N)} = A_{l,m}^{(1)} (\alpha_l^{(N)} + \beta_l^{(N)})$ we can rearrange this equation for $A_{l,m}^{(1)}$ and insert it in (1.68) to obtain

$$\begin{pmatrix} A_{l,m}^{(n)} & B_{l,m}^{(n)} \end{pmatrix}^T = \frac{C_{l,m}}{\alpha_l^{(N)} + \beta_l^{(N)}} \begin{pmatrix} \alpha_l^{(n)} & \beta_l^{(n)} \end{pmatrix}^T.$$

Therefore finding the coefficients $A_{l,m}^{(n)}, B_{l,m}^{(n)}$ reduces to finding $C_{l,m}$, since we can easily calculate the other variables. Hence we obtain

$$u(x) = \sum_{l=0}^{\infty} \sum_{m=-l}^{l} \frac{C_{l,m}}{\alpha_l^{(N)} + \beta_l^{(N)}} \left[\alpha_l^{(n)} \left(\frac{r}{r_n} \right)^l + \beta_l^{(n)} \left(\frac{r}{r_n} \right)^{-(l+1)} \right] Y_{l,m}(\xi) \quad \text{for } r_{n-1} < |x| < r_n.$$

Next we define the functions $v_{l,m} : \Omega \to \mathbb{R}$

$$v_{l,m}(x) = \frac{1}{\alpha_l^{(N)} + \beta_l^{(N)}} \left[\alpha_l^{(n)} \left(\frac{r}{r_n} \right)^l + \beta_l^{(n)} \left(\frac{r}{r_n} \right)^{-(l+1)} \right] Y_{l,m}(\xi) \quad \text{for } r_{n-1} < |x| < r_n.$$

These functions will span the finite dimensional subspace of $H^1(\Omega)$ we mentioned earlier. We have

$$\begin{aligned}
a((v_{l,m},0),(v_{k,s},0)) &= \left[\int_\Omega \sigma \nabla v_{l,m} \cdot \nabla v_{k,s} \, dx + \sum_{j=1}^{L} \frac{1}{z_j} \int_{e_j} Y_{l,m} Y_{k,s} \, d\mathcal{H}^2 \right] \\
a((v_{l,m},0),(0,e_j)) &= -\frac{1}{z_j} \int_{e_j} Y_{l,m} \, d\mathcal{H}^2 \\
a((0,e_i),(v_{k,s},0)) &= a((v_{k,s},0),(0,e_i)) \\
a((0,e_i),(0,e_j)) &= \frac{1}{z_j} |e_j| \delta_{i,j}.
\end{aligned}$$

Using (1.65) we can write

$$\int_\Omega \sigma \nabla v_{l,m} \cdot \nabla v_{k,s} \, dx = \int_0^{r_N} \sigma \int_{\mathbb{S}^2} \frac{\partial v_{l,m}}{\partial r} \frac{\partial v_{k,s}}{\partial r} + \frac{1}{r^2} \nabla_{\mathbb{S}^2} v_{l,m} \cdot \nabla_{\mathbb{S}^2} v_{k,s} \, d\mathcal{H}^2 r^2 dr.$$

For the sake of readability, we will drop the superscripts of α and β, but keep in mind, that they depend on the layer. Recall, $Y_{l,m}$ are orthogonal with respect to $L^2(\mathbb{S}^2)$, hence

$$\begin{aligned}
&\int_0^{r_N} \sigma \int_{\mathbb{S}^2} \frac{\partial v_{l,m}}{\partial r} \frac{\partial v_{k,s}}{\partial r} \, d\mathcal{H}^2 r^2 dr \\
&= \sum_{n=1}^{N} \int_{r_{n-1}}^{r_n} \sigma^{(n)} \int_{\mathbb{S}^2} \left[l\alpha_l \left(\frac{r}{r_n} \right)^l - (l+1)\beta_l \left(\frac{r}{r_n} \right)^{-l-1} \right] \left[k\alpha_k \left(\frac{r}{r_n} \right)^k - (k+1)\beta_k \left(\frac{r}{r_n} \right)^{-k-1} \right] Y_{l,m} Y_{k,s} \, d\mathcal{H}^2 dr \\
&= \sum_{n=1}^{N} \int_{r_{n-1}}^{r_n} \sigma^{(n)} \left[l\alpha_l \left(\frac{r}{r_n} \right)^l - (l+1)\beta_l \left(\frac{r}{r_n} \right)^{-l-1} \right]^2 dr \, \delta_{l,k} \delta_{m,s} \\
&= \sum_{n=1}^{N} \sigma^{(n)} \int_{r_{n-1}}^{r_n} l^2 \alpha_l^2 \left(\frac{r}{r_n} \right)^{2l} + (l+1)^2 \beta_l^2 \left(\frac{r}{r_n} \right)^{-2l-2} - 2l(l+1)\alpha_l \beta_l \left(\frac{r}{r_n} \right)^{-1} dr \, \delta_{l,k} \delta_{m,s} \\
&= \sum_{n=1}^{N} \sigma^{(n)} r_n \left[\frac{l^2 \alpha_l^2}{2l+1} \left[1 - \left(\frac{r_{n-1}}{r_n} \right)^{2l+1} \right] - \frac{(l+1)^2 \beta_l^2}{2l+1} \left[1 - \left(\frac{r_{n-1}}{r_n} \right)^{-2l-1} \right] - 2l(l+1)\alpha_l \beta_l \ln \frac{r_n}{r_{n-1}} \right] \delta_{l,k} \delta_{m,s}.
\end{aligned}$$

With (1.66) we can calculate the remaining term

$$\begin{aligned}
&\int_0^{r_N} \sigma \int_{\mathbb{S}^2} \frac{1}{r^2} \nabla_{\mathbb{S}^2} v_{l,m} \cdot \nabla_{\mathbb{S}^2} v_{k,s} \, d\mathcal{H}^2 r^2 dr \\
&= \sum_{n=1}^{N} \int_{r_{n-1}}^{r_n} \sigma^{(n)} \int_{\mathbb{S}^2} \left[\alpha_l \left(\frac{r}{r_n} \right)^l + \beta_l \left(\frac{r}{r_n} \right)^{-l-1} \right] \left[\alpha_k \left(\frac{r}{r_n} \right)^k + \beta_k \left(\frac{r}{r_n} \right)^{-k-1} \right] \nabla_{\mathbb{S}^2} Y_{l,m} \cdot \nabla_{\mathbb{S}^2} Y_{k,s} \, d\mathcal{H}^2 dr \\
&= \sum_{n=1}^{N} \int_{r_{n-1}}^{r_n} \sigma^{(n)} D_{l,m}^2 \left[\alpha_l \left(\frac{r}{r_n} \right)^l + \beta_l \left(\frac{r}{r_n} \right)^{-l-1} \right]^2 l(l+1) dr \, \delta_{l,k} \delta_{m,s}
\end{aligned}$$

$$= \sum_{n=1}^{N} \sigma^{(n)} \int_{r_{n-1}}^{r_n} \alpha_l^2 \left(\frac{r}{r_n}\right)^{2l} + \beta_l^2 \left(\frac{r}{r_n}\right)^{-2l-2} + 2\alpha_l\beta_l \left(\frac{r}{r_n}\right)^{-1} dr\, l(l+1)\, \delta_{l,k}\delta_{m,s}$$

$$= \sum_{n=1}^{N} \sigma^{(n)} r_n \left[\frac{l(l+1)\alpha_l^2}{2l+1}\left[1-\left(\frac{r_{n-1}}{r_n}\right)^{2l+1}\right] - \frac{l(l+1)\beta_l^2}{2l+1}\left[1-\left(\frac{r_{n-1}}{r_n}\right)^{-2l-1}\right] + 2l(l+1)\alpha_l\beta_l \ln\frac{r_n}{r_{n-1}}\right] \delta_{l,k}\delta_{m,s}.$$

Putting this together we finally derive

$$\int_\Omega \sigma \nabla v_{l,m} \cdot \nabla v_{k,s}\, dx = \sum_{n=1}^{N} \sigma^{(n)} r_n \left[l\left(\alpha_l^{(n)}\right)^2 \left[1-\left(\frac{r_{n-1}}{r_n}\right)^{2l+1}\right] - (l+1)\left(\beta_l^{(n)}\right)^2 \left[1-\left(\frac{r_{n-1}}{r_n}\right)^{-2l-1}\right]\right] \delta_{l,k}\delta_{m,s}.$$

The other integrals strongly depend on how we model the electrodes. For now, let us assume that we already know how to model them and how to evaluate the integrals. Let us define the operator $\Lambda : D(\Lambda) \subset \mathbb{R}^{\mathbb{N}} \to H^1(\Omega)$

$$(C_{l,m})_{l,m} \mapsto \sum_{l=0}^{\infty} \sum_{l=-m}^{m} C_{l,m} v_{l,m}.$$

The functions $(v_{l,m})$ are orthogonal in $H^1(\Omega)$, therefore the domain of Λ is the w-weighted ℓ^2 space with $w_{l,m} = \|v_{l,m}\|^2_{H^1(\Omega)}$, which we'll denote ℓ^2_w. Since $W = \operatorname{Image}(\Lambda) \oplus \mathbb{R}^L \subset H^1(\Omega) \oplus \mathbb{R}^L$ and $(u, U) \in W$, the solution (u, U) also solves the weak problem restricted to W. Note that $a : H^1(\Omega) \times H^1(\Omega) \to \mathbb{R}$ and $l : H^1(\Omega) \to \mathbb{R}$ from the weak formulation are symmetric and real-valued, hence according to the characterization theorem (Braess, 2013, Thm. 2.2) the solution can be characterized by

$$(u, U) \in \operatorname*{arg\,min}_{(v,V)\in W} \frac{1}{2} a((v, V), (v, V)) - l(v, V). \tag{1.69}$$

To be precise, we applied the characterization theorem to $W/\mathbb{R}$ which characterizes the unique solution $(u, U) + \mathbb{R}$ as the unique minimizer in $W/\mathbb{R}$. But since the objective function vanishes on constant functions, every representative of $(u, U) + \mathbb{R}$ is a minimizer in W. Note that ℓ^2_w is a Hilbert space and $\Lambda : \ell^2_w \to H^1(\Omega)$ is isometric. As $v_{0,0} = (4\pi)^{-\frac{1}{2}}$ it follows that $\Lambda(\mathbb{R}, 0, \dots) = \mathbb{R} \subset H^1(\Omega)$. Therefore we define

$$K = \{x \in \ell^2_w : x_{l,m} = 0\ \forall l, m \neq 0\} = \Lambda^{-1}(\mathbb{R}).$$

These elements correspond to the constant functions in $\operatorname{Image}(\Lambda)$. When we write $(\ell^2_w \oplus \mathbb{R}^L)/\mathbb{R}$, we precisely mean $(\ell^2_w \oplus \mathbb{R}^L)/(K \oplus \mathbb{R})$. Note that we can canonically define $(\Lambda, \mathrm{id}) : (\ell^2_w \oplus \mathbb{R}^L)/\mathbb{R} \to (H^1(\Omega) \oplus \mathbb{R}^L)/\mathbb{R}$ and that this mapping remains isometric. The above minimizing problem (1.69) is equivalent to the minimizing problem, where one pulls back a and l by (Λ, id). Let us further define

$$\eta_{l,m} = \sum_{n=1}^{N} \sigma^{(n)} r_n \left[l\left(\alpha_l^{(n)}\right)^2 \left(1 - \left(\frac{r_{n-1}}{r_n}\right)^{2l+1}\right) - (l+1)\left(\beta_l^{(n)}\right)^2 \left(1 - \left(\frac{r_{n-1}}{r_n}\right)^{-2l-1}\right)\right]$$

$$\gamma^{(j)}_{l,m,k,s} = \int_{e_j} Y_{l,m} Y_{k,s}\, d\mathcal{H}^2 \quad \text{and} \quad \beta_{j,l,m} = \int_{e_j} Y_{l,m}\, d\mathcal{H}^2.$$

The approach of Somersalo et al. (1992) applied on the three dimensional case would be as follows: Since the series expansion of $\tilde{u}$ converges in $H^1(\Omega)$, we can write

$$a((u, U), (u, U)) = a((u, 0), (u, 0)) + 2a((u, 0), (0, U)) + a((0, U), (0, U))$$

$$= \sum_{l,m}\sum_{k,s} C_{l,m}C_{k,s}\, a((v_{l,m}, 0), (v_{k,s}, 0)) + 2\sum_{j=1}^{L}\sum_{l,m} C_{l,m}U_j\, a((v_{l,m}, 0), (0, e_j)) + \sum_{i,j=1}^{L} U_iU_j\, a((0, e_i), (0, e_j))$$

$$= \sum_{l,m} C_{l,m}^2 \eta_{l,m} + \sum_{j=1}^{L} \frac{1}{z_j} \left[\sum_{l,m}\sum_{k,s} C_{l,m}C_{k,s}\gamma^{(j)}_{l,m,k,s} - 2U_j \sum_{l,m} C_{l,m}\beta_{j,l,m} + U_j^2|e_j|\right].$$

If we order the pairs (l,m), $l \in \mathbb{N}_0$, $m = -l,\dots,l$, lexicographically, then we can think of $C = (C_{l,m})_{l,m}$ as a vector and define a bilinear form $M_S : \mathbb{R}^L \oplus \ell^2_w \times \mathbb{R}^L \oplus \ell^2_w \to \mathbb{R}$ by formally multiplying in the style of $x^T S x$ with the following infinite-dimensional matrix

$$S = \begin{pmatrix} \operatorname{diag}_L \left(\frac{U_j|e_j|}{z_j}\right)_{j=1\dots L} & -\left(\frac{1}{z_j}\beta_{j,l,m}\right)_{\substack{j=1\dots L \\ l,m}} \\ -\left(\frac{1}{z_j}\beta_{j,l,m}\right)^T_{\substack{j=1\dots L \\ l,m}} & \operatorname{diag}_\infty (\eta_{l,m})_{l,m} + \sum_{j=1}^L \frac{1}{z_j}\left(\gamma^{(j)}_{l,m,k,s}\right)_{\substack{k,s \\ l,m}} \end{pmatrix}.$$

Further define a similar operator $M_r : \mathbb{R}^L \oplus \ell^2_w \to \mathbb{R}$ with

$$r = \begin{pmatrix} I_1 & \dots & I_L & 0 & 0 & \dots \end{pmatrix}^T$$

by $M_r((v,V)) = \langle r, (V,v)\rangle$. Then (1.69) is equal to

$$\min_{v\in\ell^2_w, V\in\mathbb{R}^L} \frac{1}{2} M_S((V,v),(V,v)) - M_r((V,v)).$$

Choosing the finite dimensional subspace $\ell_N = \{(l,m) : 0 \le l \le N, -l \le m \le l\}$, we can truncate S at the $L + (N+1)^2$th row and column, and r at the $L + (N+1)^2$th row, to obtain S_N and r_N and solve the problem

$$\min_{v_N\in\ell_N, V\in\mathbb{R}^L} \frac{1}{2}(V,v_N)^T S_N (V,v_N) - (V,v_N)^T r_N$$

as an approximation. Hence we have to solve the system $S_N(V,v_N) = r_N$, where S_N is a finite dimensional matrix.
The slightly different approach mentioned previously is as follows: We already know that $u \in \text{Image}(\Lambda)$, hence there exists a unique element $\tilde{u} \in \ell^2_w$ with $u = \Lambda\tilde{u}$. Since (u,U) is a solution of the CEM we obtain

$$\tilde{a}((\tilde{u},U),(v,V)) = a((\Lambda\tilde{u},U),(\Lambda v,V)) = l(\Lambda v,V) = \tilde{l}(v,V) \quad \forall (v,V) \in \ell^2_w \oplus \mathbb{R}^L.$$

As $\tilde{a}$ is coercive on $(\ell^2_w \oplus \mathbb{R}^L)/\mathbb{R}$, it follows from the Lemma of Lax-Milgram, that $(\tilde{u},U)$ is the unique solution of the problem in $(\ell^2_w \oplus \mathbb{R}^L)/\mathbb{R}$. We can now restrict this problem to the space $(\ell_N \oplus \mathbb{R}^L)/\mathbb{R}$. By the same arguments as before, it follows that there exists a unique solution. If we take a closer look, we see that the formulation is equivalent to

$$(V_N,v_N)^T S_N (U_N,\tilde{u}_N) = (V_N,v_N)^T r_N \quad \forall (v_N,V_N) \in (\ell_N \oplus \mathbb{R}^L)/\mathbb{R}.$$

Hence we obtain the identical equation system. Furthermore we have the Garlerkin orthogonality

$$\tilde{a}((\tilde{u}-u_N, U-U_N),(v_N,V_N)) = 0 \quad \forall (v_N,V_N) \in (\ell_N \oplus \mathbb{R}^L)/\mathbb{R}$$

and hence

$$\begin{aligned} &c\|(\tilde{u}-u_N,U-U_N)\|^2_{(l^2_w\oplus\mathbb{R}^L)/\mathbb{R}} \le \tilde{a}((\tilde{u}-u_N,U-U_N),(\tilde{u}-u_N,U-U_N)) \\ &= \tilde{a}((\tilde{u}-u_N,U-U_N),(\tilde{u}-v_N,U-V_N)) \le C\|(\tilde{u}-u_N,U-U_N)\|\|(\tilde{u}-v_N,U-V_N)\|, \end{aligned}$$

where the last two norms are taken in $(l^2_w \oplus \mathbb{R}^L)/\mathbb{R}$. Thus there exists $C > 0$ with

$$\|(\tilde{u}-u_N,U-U_N)\|_{(l^2_w\oplus\mathbb{R}^L)/\mathbb{R}} \le C \inf_{(v_N,V_N)\in\ell_N\oplus\mathbb{R}^L/\mathbb{R}} \|(\tilde{u}-v_N,U-V_N)\|_{(l^2_w\oplus\mathbb{R}^L)/\mathbb{R}}.$$

Now note that we can choose $V_N = U$ and project $\tilde{u}$ onto ℓ_N, which we'll denote $\tilde{u}_N$. Since the series expansion of u converges in $H^1(\Omega)$, it follows $\|\tilde{u}-\tilde{u}_N\|_{\ell^2_w} \to 0$. We finally obtain

$$\|(u-\Lambda u_N, U-U_N)\|_{(H^1(\Omega)\oplus\mathbb{R}^L)/\mathbb{R}} = \|(\tilde{u}-u_N,U-U_N)\|_{(l^2_w\oplus\mathbb{R}^L)/\mathbb{R}} \le C\|\tilde{u}-\tilde{u}_N\|_{\ell^2_w} \to 0.$$

When trying to invert S_N the same problem as in the FEM case arises. Unfortunately S_N is only positive semi-definite, the null space is given by $\mathbb{R} \cdot (e_1 + \cdots + e_{L+1})$. We can enforce uniqueness of the solution in $\ell_N \oplus \mathbb{R}^l$, if we add the condition $\Lambda(u_N)(0) = 0$. We can incorporate this condition similar to the FEM case. We can replace the $L+1$th row and column of S_N by 0 and insert a 1 on the diagonal and therefore enforcing $(u_N)_{0,0} = 0$.

So far we assumed that we know how to model the electrodes and how to calculate the integrals. In the following we want to specify this. We will model the electrodes as spherical caps. Let $x_j \in r_N \mathbb{S}^2$ be the center of the electrode, then

$$e_j = \{x \in r_N \mathbb{S}^2 : \frac{x \cdot x_j}{r_N^2} > \cos \alpha_j\}$$

is a spherical cap with width $2\alpha_j$. Now we could use special quadrature rules for spherical caps as in Hesse and Womersley (2012) to approximate the integrals, but we will try to carry out some more analytical calculations to speed up numerical calculations. Therefore we want to express the electrodes in spherical coordinates. Hence consider $(\theta, \varphi) \mapsto r_N(\sin\theta\cos\varphi, \sin\theta\sin\varphi, \cos\theta)$ with $\theta \in [0, \pi]$, $\varphi \in [0, 2\pi)$, where we will identify coordinates that map to the same point, namely to the north resp. south pole.
Let (θ_j, φ_j) be the spherical coordinates of x_j. If $x_j = (0, 0, \pm r_N)$, then we easily see that $e_j = [0, \alpha) \times [0, 2\pi)$ resp. $e_j = (\pi - \alpha, \pi] \times [0, 2\pi)$. Let us consider the case $x_j \neq (0, 0, \pm r_N)$. Denote for $x \in e_j$ the spherical coordinates by (θ, φ) Let $\beta = \arccos \frac{x \cdot x_j}{r_N^2}$ be the central angle between x and x_j. We have $0 \leq \beta \leq \alpha$. The three points $\frac{x}{r_N}, \frac{x_j}{r_N}$ and $(0, 0, 1)$ span a spherical triangle on $\mathbb{S}^2$ with side lengths β, θ, θ_j and a dihedral angle at $(0, 0, 1)$ equal to $|\varphi - \varphi_j|$.The cosine law for spherical triangles (Gellert et al., 1975, Ch. 12) reads

$$\cos\beta = \cos\theta\cos\theta_j + \sin\theta\sin\theta_j\cos(\varphi - \varphi_j).$$

We can use this and derive

$$\cos(\varphi - \varphi_j) = \frac{\cos\beta - \cos\theta\cos\theta_j}{\sin\theta\sin\theta_j}. \tag{1.70}$$

Hence we can express $|\varphi - \varphi_j|$ as a function of θ and β. Unfortunately, when φ is close to φ_j errors on the right hand side in (1.70) will lead to quite large numerical errors in $|\varphi - \varphi_j|$ as arccos is ill-conditioned near 1. Alternatively we can use the haversine formula (Korn and Korn, 1968, Sec. B.9), which can be rearranged to obtain

$$\mathrm{hav}(\varphi - \varphi_j) = \frac{\mathrm{hav}\beta - \mathrm{hav}(\theta - \theta_j)}{\sin\theta\sin\theta_j} = \frac{\cos(\theta_j - \theta) - \cos\beta}{2\sin\theta\sin\theta_j}.$$

Note that $\mathrm{hav}x = \sin^2\frac{x}{2}$, hence we traded arccos in for arcsin, which is better conditioned near 0. The author's numerical experiments showed no significant effect on the final results. We define

$$g_j(\theta) = 2\arcsin\left[\left(\frac{\cos(\theta_j - \theta) - \cos\alpha}{2\sin\theta\sin\theta_j}\right)^{\frac{1}{2}}\right] \quad \theta \in (0, \pi).$$

It is plausible to restrict $\alpha \leq \frac{\pi}{2}$. In order to simplify calculations, we won't restrict φ to the interval $[0, 2\pi)$ but we will identify points via $(\theta_1, \varphi_1) \sim (\theta_2, \varphi_2) \Leftrightarrow \theta_1 = \theta_2$ and $\varphi_1 \equiv \varphi_2 \pmod{2\pi}$. Let us first assume $\alpha \leq \theta_j$ and $\alpha \leq \pi - \theta_j$. This means that the electrode does not overlap one of the poles. Then the electrode is given by

$$e_j = \{(\theta, \varphi) \in (\theta_j - \alpha, \theta_j + \alpha) \times [\varphi_j - \alpha, \varphi_j + \alpha] : |\varphi - \varphi_j| < g_j(\theta)\}/\sim.$$

For $\alpha > \theta_j$ we get

$$e_j = [0, \alpha - \theta_j) \times [0, 2\pi] \cup \{(\theta, \varphi) \in [\alpha - \theta_j, \theta_j + \alpha) \times [\varphi_j - \alpha, \varphi_j + \alpha] : |\varphi - \varphi_j| < g_j(\theta)\}/\sim$$

and otherwise for $\pi - \theta_j < \alpha$

$$e_j = (2\pi - \theta_j - \alpha, \pi] \times [0, 2\pi] \cup \{(\theta, \varphi) \in (\theta_j - \alpha, 2\pi - \theta_j - \alpha] \times [\varphi_j - \alpha, \varphi_j + \alpha] : |\varphi - \varphi_j| < g_j(\theta)\}/\sim.$$

Recall the spherical harmonic basis functions from (1.62)

$$Y_{l,m}(\theta, \varphi) = N_{l,m} P_{l,3,|m|}(\cos\theta) \cdot \begin{cases} \cos(m\varphi), & \text{for } m > 0 \\ 1, & \text{for } m = 0 \\ \sin(|m|\varphi), & \text{for } m < 0, \end{cases}$$

where $N_{l,m}$ are normalizing constants. Since we are only dealing with $\mathbb{R}^3$, we will omit the 3 from the subscripts of the associated Legendre functions. Denote the function after the bracket by f_m. Since we want to integrate the product of two spherical harmonics, we have to integrate the product of all pairs consisting of $\sin, \cos$ and 1, i.e $f_m f_s$. For all these combinations we can quite easily find their antiderivative, which we will denote by $F_{m,s}$ (see A.1). The antiderivative of f_m is given by $F_{m,0}$. We can now tackle the integrals

$$\int_{e_j} Y_{l,m} Y_{k,s} \, d\mathcal{H}^2 \quad \text{and} \quad \int_{e_j} Y_{l,m} \, d\mathcal{H}^2.$$

We first consider the case $\alpha \leq \theta_j$ and $\alpha \leq \pi - \theta_j$. Then

$$\begin{aligned} \int_{e_j} Y_{l,m} Y_{k,s} \, d\mathcal{H}^2 &= r_N^2 \int_{\theta_j - \alpha}^{\theta_j + \alpha} \int_{\varphi_j - g_j(\theta)}^{\varphi_j + g_j(\theta)} N_{l,m} N_{k,s} P_{l,|m|}(\cos\theta) P_{k,|s|}(\cos\theta) \sin\theta f_m(\varphi) f_s(\varphi) d\varphi \, d\theta \\ &= r_N^2 \int_{\theta_j - \alpha}^{\theta_j + \alpha} N_{l,m} N_{k,s} P_{l,|m|}(\cos\theta) P_{k,|s|}(\cos\theta) \sin\theta (F_{m,s}(\varphi_j + g_j(\theta)) - F_{m,s}(\varphi_j - g_j(\theta))) d\theta \end{aligned} \tag{1.71}$$

and similar

$$\int_{e_j} Y_{l,m} \, d\mathcal{H}^2 = r_N^2 \int_{\theta_j - \alpha}^{\theta_j + \alpha} N_{l,m} P_{l,|m|}(\cos\theta) \sin\theta (F_{m,0}(\varphi_j + g_j(\theta)) - F_{m,0}(\varphi_j - g_j(\theta))) d\theta.$$

Now assume $\alpha > \theta_j$, the case $\alpha > \pi - \theta_j$ is similar. Then we get

$$\int_{e_j} Y_{l,m} Y_{k,s} \, d\mathcal{H}^2 = r_N^2 \left[\int_0^{\alpha - \theta_j} \int_0^{2\pi} Y_{l,m} Y_{k,s} d\varphi \, d\theta + \int_{\alpha - \theta_j}^{\theta_j + \alpha} \int_{\varphi_j - g_j(\theta)}^{\varphi_j + g_j(\theta)} Y_{l,m} Y_{k,s} d\varphi \, d\theta \right]. \tag{1.72}$$

The second summand is similar to the integrals in (1.71), only the integration boundaries w.r.t θ are different. Looking at the first summand yields

$$\int_0^{\alpha - \theta_j} \int_0^{2\pi} Y_{l,m} Y_{k,s} d\varphi \, d\theta = \int_0^{\alpha - \theta_j} N_{l,m} N_{k,s} P_{l,|m|}(\cos\theta) P_{k,|s|}(\cos\theta) \sin\theta \, d\theta \cdot \begin{cases} 0, & \text{for } m \neq s \\ \pi, & \text{for } m = s \neq 0 \\ 2\pi, & \text{for } m = s = 0 \end{cases}.$$

The integral of $\int_{e_j} Y_{l,m} \, d\mathcal{H}^2$ can be split similar to (1.72), where we then only have two cases for the first summand, namely

$$\int_0^{\alpha - \theta_j} \int_0^{2\pi} Y_{l,m} d\varphi \, d\theta = \int_0^{\alpha - \theta_j} N_{l,m} P_{l,|m|}(\cos\theta) \sin\theta \, d\theta \cdot \begin{cases} 0, & \text{for } m \neq 0 \\ 2\pi, & \text{for } m = 0 \end{cases}.$$

Hence we have to calculate integrals of the form

$$\int_a^b P_{l,m}(\cos\theta)P_{k,s}(\cos\theta)\sin\theta\ h(\theta)\,d\theta,$$

where $[a,b] \subseteq [0,\pi]$ and h is an arbitrary function dependent on θ. We can transform the integral by $t = \cos\theta$ and derive

$$\int_{\cos b}^{\cos a} P_{l,m}(t)P_{k,s}(t)\ h(\arccos(t))\,dt.$$

Note that

$$g_j(\arccos(t)) = \arccos\left(\frac{\cos\alpha - t\cos\theta_j}{\sqrt{1-t^2}\sin\theta_j}\right) = 2\arcsin\left[\left(\frac{\cos(\theta_j - \arccos(t)) - \cos\alpha}{2\sqrt{1-t^2}\sin\theta_j}\right)^{\frac{1}{2}}\right].$$

We will use a Gauss-Legendre quadrature from Trefethen (2008) in order to numerically approximate the integrals. A Gauss-Legendre quadrature with n points is exact on polynomials up to degree $2n-1$.

1.5.2. Point Electrode Model

For the point electrode model on the four layer sphere model formulas are derived in Ferree et al. (2000) and the references therein. They deal with the case of 2 electrodes, but can easily be modified to the multiple electrode case. As the mere presence of further electrodes doesn't effect the potential generated by the others, one can take advantage of azimuthal symmetries, which yield simpler series expansions. Assume that the electrode set up is given by

$$g = \sum_{i=1}^{L} I_i \delta_{x_i},$$

where $I \in \mathbb{R}^L_\diamond$. Then the potential is given by

$$u(x) = \sum_{l=1}^{\infty}\left[\left(A_l^{(n)}\left(\frac{r}{r_n}\right)^l + B_l^{(n)}\left(\frac{r}{r_n}\right)^{-(l+1)}\right)\sum_{i=1}^{L} I_i P_l\left(\arccos\frac{\langle x, x_i\rangle}{|x| r_4}\right)\right] \quad \text{for } r_{n-1} < |x| < r_n.$$

For the coefficients $A_l^{(n)}, B_l^{(n)}$, $n = 1\ldots4$, $l \in \mathbb{N}$, we refer to Ferree et al. (2000) and the correction Ferree et al. (2001). It is not expected that this series converges in $H^1(\Omega)$, but perhaps in $H^{\frac{1}{2}-\varepsilon}(\Omega)$ or in $H^1(\Omega_0)$ for $\Omega_0 \Subset \Omega$. Further investigations would be needed, but we will ignore this and continue without.

1.6. Numerical Evaluation

Before we continue with our further analysis involving the finite element solutions, we will try to verify them on a four layer sphere model with isotropic conductivity, consisting of four concentric layers representing skin, skull, cerebrospinal fluid (CSF) and brain. As a reference we will use the semi-analytically expressions derived in the previous sections. Furthermore we want to compare the semi-analytic solutions of the PEM and the CEM to illustrate the differences and investigate whether the FEM solutions behave similarly. We are particularly interested in the behavior of the FEM solutions when we reduce the electrode size. Note that we did not derive (semi-) analytical expressions for the current density, hence we will only compare the numerical ones. The radii and the conductivities of the model are shown in table 1.1 (Dannhauer et al., 2011; Baumann et al., 1997). Note that the conductivity of the skull compacta is chosen for the whole skull layer. In order to compute the FEM solutions, the open source MATLAB (2020) toolbox Zeffiro Interface (2022) was used, a tool for finite element method assisted forward and inverse simulations for electromagnetic brain imaging and investigations. Zeffiro requires surfaces meshes of the compartments as an input. It generates a hexahedral volume mesh and divides every hexahedron into tetrahedrons. Then those are assigned to a compartment, based on their position relative to the surface meshes. A set of high quality surface meshes generated by Lunkenheimer (2021) was used, consisting of 155734 nodes and 311452 triangles with an average edge length of 1.63 mm (min. 1.03 mm, max. 2.33 mm). The quality is measured by the scaled ratio of inradius and circumradius, where 1 is optimal and 0 the worst possible. The used meshes have an average value of 0.9919 and a minimal value of 0.6457. The volume mesh generated by Zeffiro with a mesh width of 1 mm consisted of 3260879 nodes and 15908720 tetrahedrons. Further a smoothing was applied to remove the staircase pattern. The effect of this smoothing can be seen in figure 1.2. As a comparison the semi-analytical solutions obtained in the previous section 1.5 were implemented in MATLAB (2020) and evaluated at the nodes of the mesh. We will consider three different electrode montages. The first two setups consist of two electrodes each, which are sep-

Outer radius (mm)	Tissue	Conductivity (S/m)
92	Skin	0.43
86	Skull	0.0064
80	CSF	1.79
78	Brain	0.33

Table 1.1.: Four layer sphere model

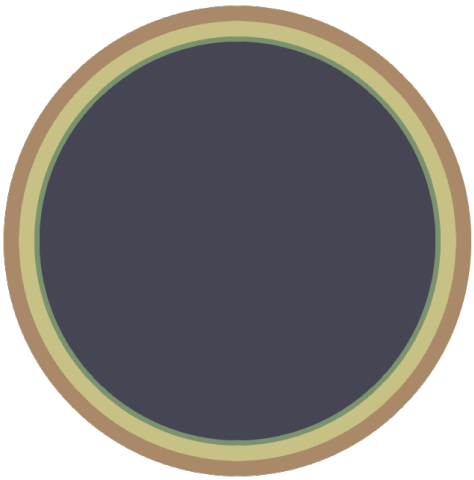

Figure 1.1.: Cross section of model

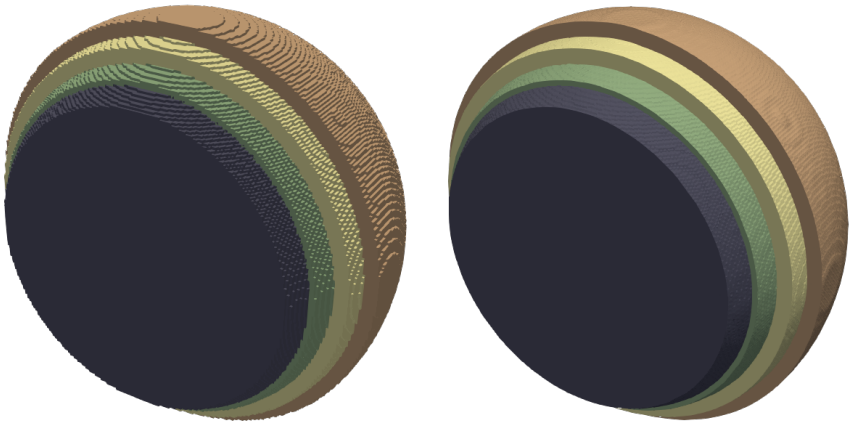

Figure 1.2.: Volume mesh non-smoothed (l.) and smoothed (r.)

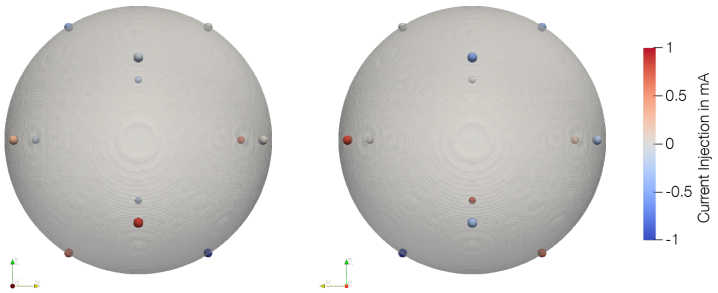

Figure 1.3.: Current pattern of (iii) front (l.) & back (r.)

arated at a 90 degree angle (i) and in the second case at a 180 degree angle (ii). A unit current is injected in both cases. Since the PDE is linear, we can think of this as being in 1 and $-1\,mA$. The last montage is placed at the corners of an icosahedron (iii) and a randomly generated injection pattern with $\|I\|_\infty \leq 1$ was used. The setup and amperages are shown in figure 1.3. Since we don't want to focus on the effect of different values for the contact impedance, we will simply use the default value of Zeffiro, which is $2k\Omega$. Since the potentials aren't unique, we have to choose a reference. In the following all potentials are chosen such that $u(0) = 0$. The location of the point electrode will always be the center of the spherical cap representing the electrode from the CEM. Zeffiro determines the discretized electrode, which consists of surface triangles, based on the euclidean distance between the centroid of the triangle and the center of the spherical cap.
We introduce three different types of global measures in order to compare a potential u with a reference potential u_{ref}. The relative error (RE) is defined by

$$RE(u, u_{\text{ref}}) = \frac{\|u - u_{\text{ref}}\|_{L^2}}{\|u_{\text{ref}}\|_{L^2}}.$$

As the name already implies, it puts the absolute difference in proportion to the norm of the reference potential. The next measure is the Relative Difference Measure (RDM). It focuses on the distribution of the potentials and tries to suppress errors resulting from different magnitudes. It is defined as

$$RDM(u, u_{\text{ref}}) = \left\| \frac{u}{\|u\|_{L^2}} - \frac{u_{\text{ref}}}{\|u_{\text{ref}}\|_{L^2}} \right\|_{L^2}.$$

In contrast the Magnitude Error (MAG) ignores the distribution and measures differences in the magnitude

$$MAG(u, u_{\text{ref}}) = \frac{\|u\|_{L^2}}{\|u_{\text{ref}}\|_{L^2}} - 1.$$

Further we want to introduce a local counterpart to the relative error, namely the local Relative Error (local RE)

$$\textit{local } RE(u, u_{\text{ref}}, x) = \frac{|u(x) - u_{\text{ref}}(x)|}{|u_{\text{ref}}(x)|}.$$

Note that the term *error* can be misleading, because not all differences we will measure are automatically errors. The L^2-norm was approximated by using a four point quadrature on each tetrahedron with equal weights and evaluation points at the vertices, i.e.

$$\int_\Omega f(x)^2\,dx \approx \sum_{T \in \mathcal{T}} \frac{|T|}{4} \left[\sum_{v \in \mathcal{V}_T} f(v)^2 \right],$$

where $\mathcal{T}$ denotes the set of tetrahedrons and $\mathcal{V}_T$ the set of vertices of $T \in \mathcal{T}$.

1.6.1. Semi-analytical PEM solution

As stated in section 1.5.2, the solution of the point electrode model can be expressed as a series, which in turn will be approximated by a finite sum. We want to find out what number of summands is appropriate to truncate the series. We will denote the number of summands used by n. Different approximations u_n, with n between 0 and 1000, were calculated on the mesh and compared to the reference potential with $n = 1000$. The results are shown in figure 1.4. We see that the relative errors in skull, CSF and brain rapidly decrease. In the skin they decrease only slowly due to the high irregularity at the electrodes. At least in the interior of the sphere model the series seems to converge, but keep in mind that we aren't using the analytical solution of the PEM as a reference, but only u_{1000}, which is much more regular.

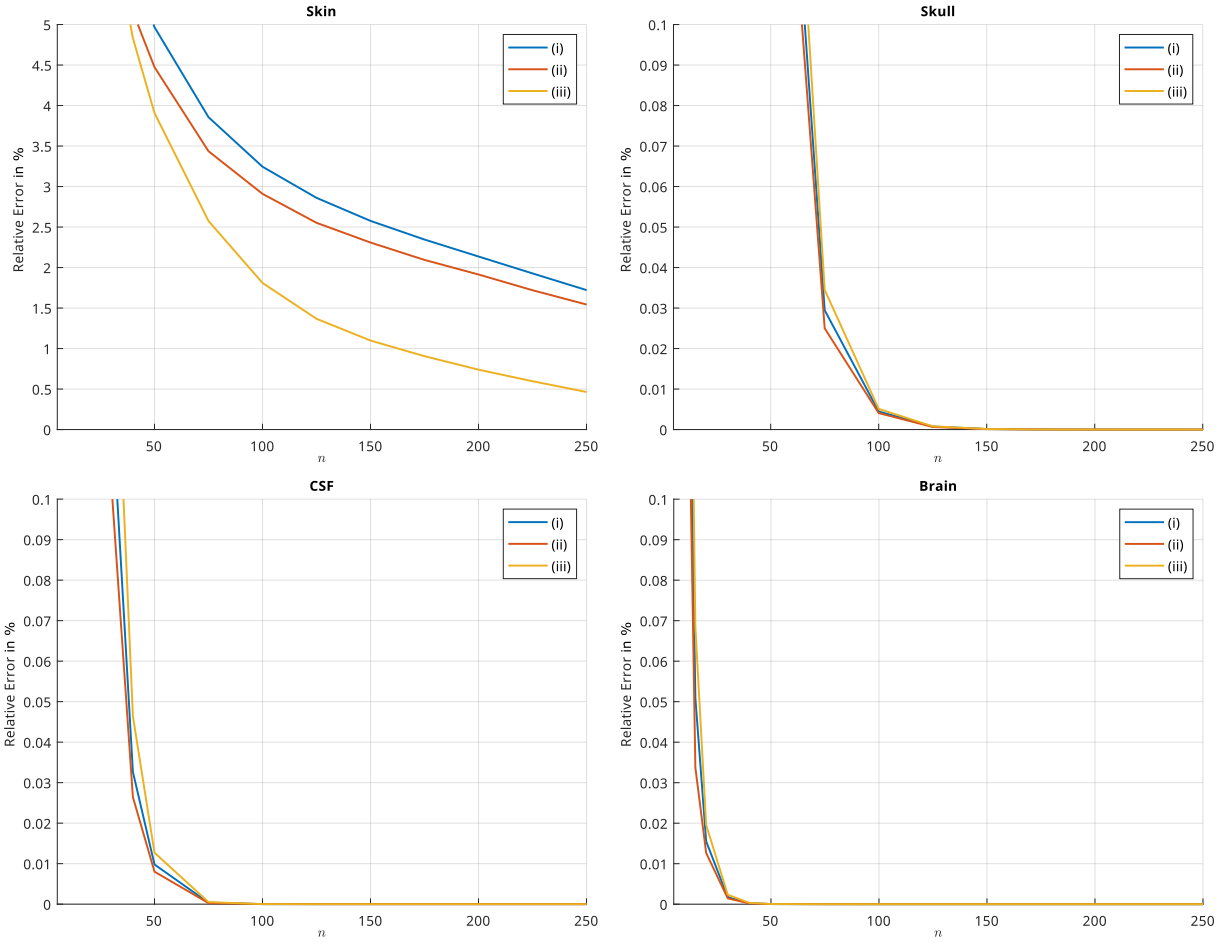

Figure 1.4.: RE of PEM approximations u_n and $u_{\text{ref}} = u_{1000}$

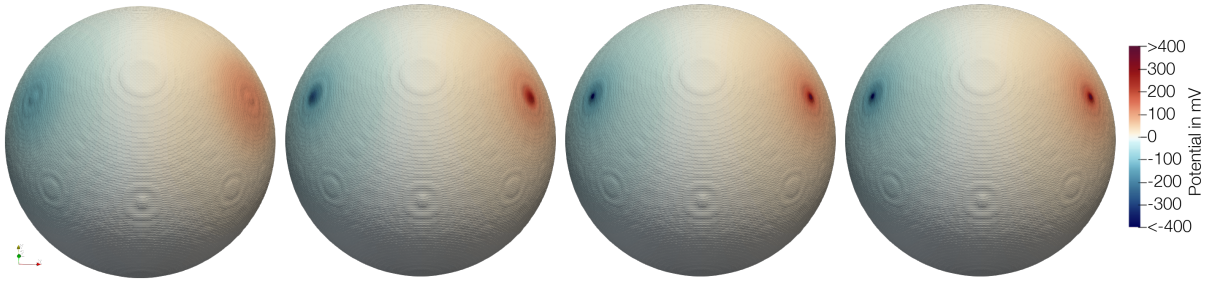

Figure 1.5.: Potential of setup (i) for $n = 10, 50, 250, 1000$ (left to right)

Figure 1.5 shows that the potential only becomes more singular at the electrode positions with increasing n, but does not change much further away. MAG errors rapidly converge to zero in all cases and compartments and thus RDM errors behave similar to the relative errors. Since we are mainly interested in the potential in the brain $n = 250$ will be by far sufficient for our further analysis. Figure 1.6 shows that in this case the local relative error is mostly far below one percent. High errors mainly arise at the zero potential line, because of dividing by zero, and at the injection electrodes, which is due to the previously mentioned high irregularity of the boundary conditions. Therefore we will fix $n = 250$ for further analysis regarding the point electrode model. Note that the errors around the zero potential line will occur in all future cases and hence we won't further mention them.

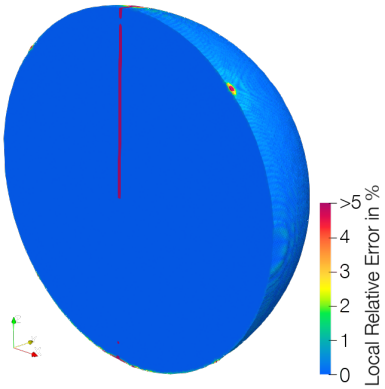

Figure 1.6.: Local RE of u_{250}

1.6.2. Semi-analytical CEM solution

We will repeat the previous analysis for the complete electrode model. Therefore we consider the same electrode setups with a radius of $1cm$. Due to higher computational costs it was only possible to use $n = 250$ as a reference. The two most interesting compartments are the brain and the skin. The brain obviously as the subject of neurological interest and the skin due to its proximity to the electrodes. The results for these compartments are shown in figure 1.7. Note

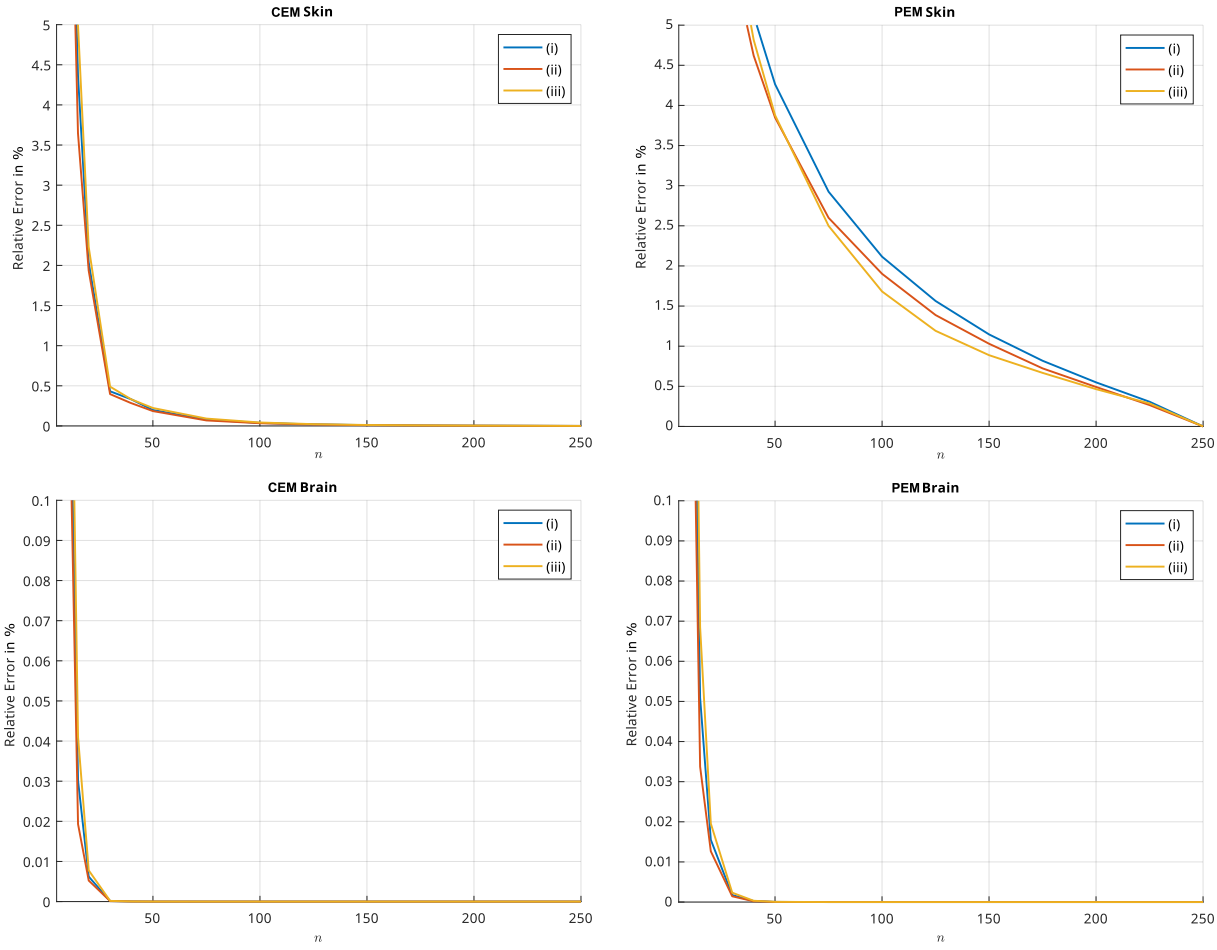

Figure 1.7.: RE of CEM and PEM approximations u_n and $u_{\text{ref}} = u_{250}$

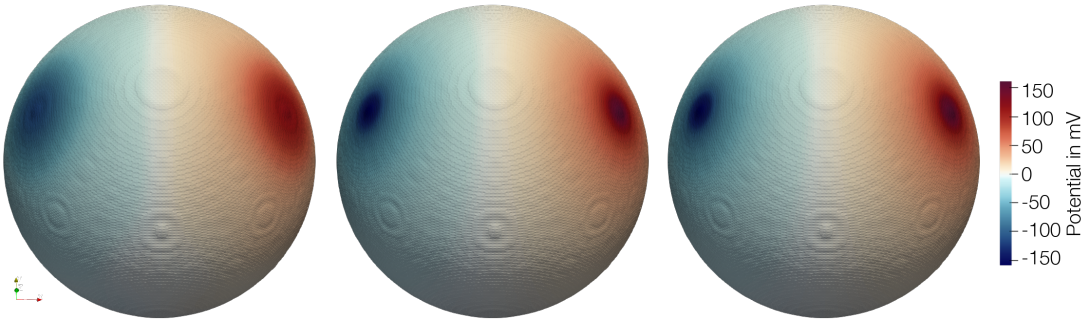

Figure 1.8.: Potential of setup (i) for $n = 10, 50, 250$ (l. to r.)

that the results for the PEM with reference $n = 250$ are also included in order to make the results comparable. We can clearly see that the solution of the CEM converges faster in the skin, whereas there is no significant difference in the brain. The solutions for $n = 10, 50, 250$ are shown in figure 1.8. On the surface they converge and the potential concentrates around the two electrodes, but due to the spatial extent of the electrodes it does not become singular. In particular, figure 1.9 can be seen as a proof of concept for section 1.5.1 as the topography of the potential looks plausible and fits perfectly to the electrode. As before we will use $n = 250$ for our analysis.

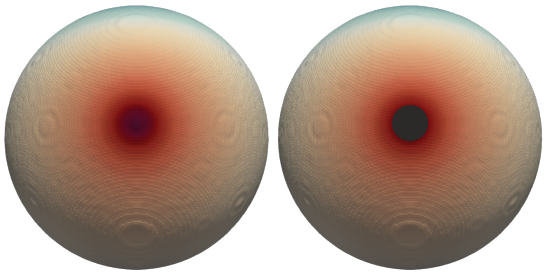

Figure 1.9.: Position of electrode (black)

One major difference of the CEM is that current can shunt through the electrode, hence an inactive electrode also influences the potential. To see these effects an additional inactive electrode is placed between the already existing electrodes of setup (i) (figure 1.10(a)). In order to investigate the differences caused, the resulting potential is compared with the potential of (i) only consisting of the two active electrodes. In table 1.2 and figure 1.10(b)-(c) the new potential with the additional electrode was used as reference potential. In (b) one can clearly see that the additional electrode influences the potential, as you can already infer the position from the error. Further the effect is mainly limited to the outer compartment. Moreover, they are extremely small resulting in local relative errors below 2.5×10^{-6}. The global errors in table 1.2 are even smaller.

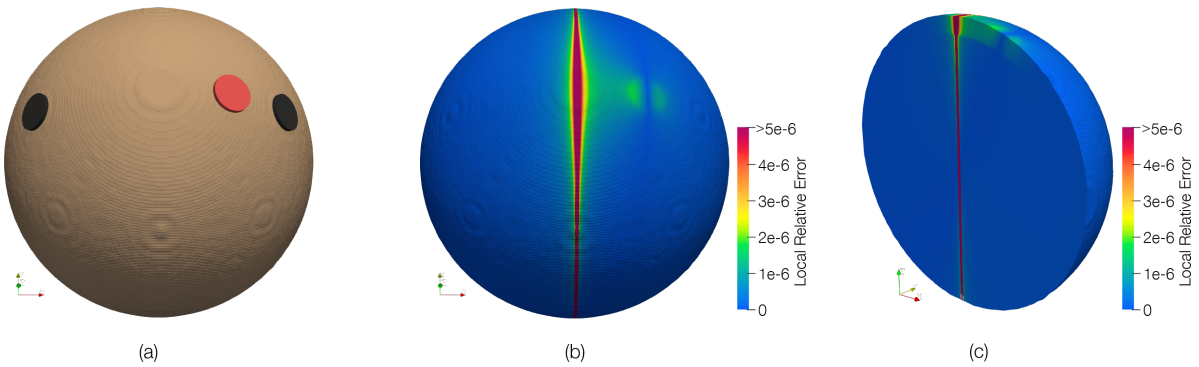

Figure 1.10.: (a) Position of inactive electrode (red), (b)&(c) Local RE to potential of setup (i)

	Total	Skin	Skull	CSF	Brain
RE	1.05×10^{-7}	1.10×10^{-7}	9.74×10^{-8}	5.56×10^{-8}	5.05×10^{-8}
MAG	4.67×10^{-8}	4.68×10^{-8}	4.67×10^{-8}	4.39×10^{-8}	4.35×10^{-8}
RDM	9.42×10^{-8}	9.95×10^{-8}	8.55×10^{-8}	3.42×10^{-8}	2.58×10^{-8}

Table 1.2.: Differences of potentials with and without inactive electrode

1.6.3. Comparison of semi-analytical solutions for PEM and CEM

We want to compare the solution of the complete electrode model with the one obtained from the point electrode model. Even though it would be interesting to compare the current densities, as these are essential for electrical brain stimulation, we haven't derived expressions therefore and must restrict ourselves to the potentials. Alternatively we could use the potential and differentiate numerically, but we will omit this comparison here and only carry it out for the numerical solutions later.

The differences between the potentials for all three electrode setups are shown in table 1.3, where the CEM was chosen as reference. As expected large differences occur in the skin and skull compartments. Those are damped by the skull resulting in only small differences in the CSF and brain layer. In all cases the (average) relative error in the brain is below 0.6 percent and RDM and MAG errors are even lower. The usage of twelve electrodes increases the discrepancies between CEM and PEM only slightly compared to the setup (ii) consisting of only two electrodes. Interestingly differences decrease when the electrodes move further apart. Looking at the potentials in figure 1.11(b) one can clearly see that the point electrode causes a much higher and singular magnitude at the electrode, whereas the potential of the CEM is more spread out, since the shape of the electrode is considered as well. This is also evident from the ring pattern around the electrode in figure 1.11(a). The cross section in figure 1.11(a) shows that the topographies don't change much. If one looks closely, one can see that the outer most isolines of the PEM are shifted slightly inwards, meaning that the potential in the brain area directly underneath the electrode has a slightly higher magnitude. This results in a local relative error of 1 to 2.3 percent, as seen in figure 1.12(b). Hence it is reasonable to assume that there is a relevant effect on the stimulation of superficial targets in the brain. We will analyze this more deeply in chapter 2.

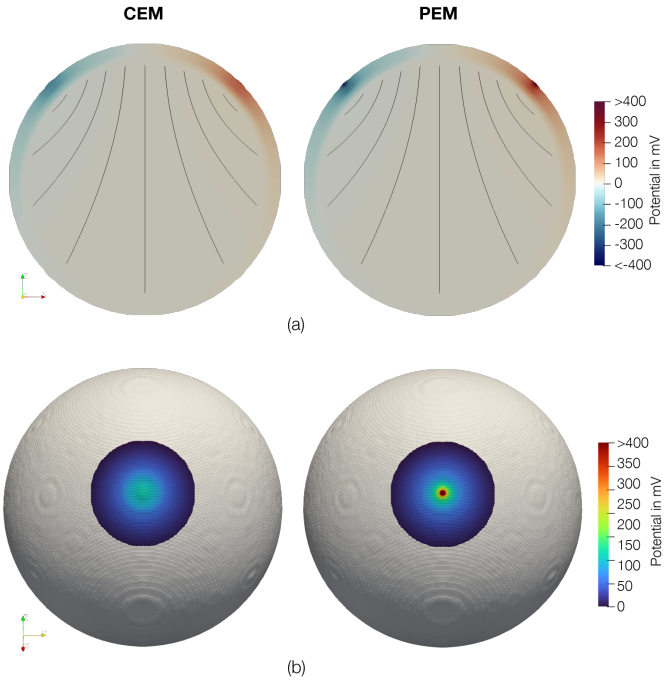

Figure 1.11.: (a) Cross section of potential (b) Potential near electrode

Setup	Measure	Total	Skin	Skull	CSF	Brain
(i)	RE%	8.16	9.42	4.41	0.90	0.48
	MAG%	1.90	2.15	1.44	0.44	0.38
	RDM%	7.86	9.07	4.14	0.79	0.29
(ii)	RE%	7.19	8.39	3.87	0.70	0.37
	MAG%	1.48	1.71	1.12	0.34	0.32
	RDM%	6.98	8.14	3.68	0.60	0.20
(iii)	RE%	8.50	9.65	5.03	1.20	0.58
	MAG%	2.29	2.54	1.81	0.57	0.44
	RDM%	8.10	9.20	4.65	1.05	0.39

Table 1.3.: Differences of PEM and CEM (reference) solutions

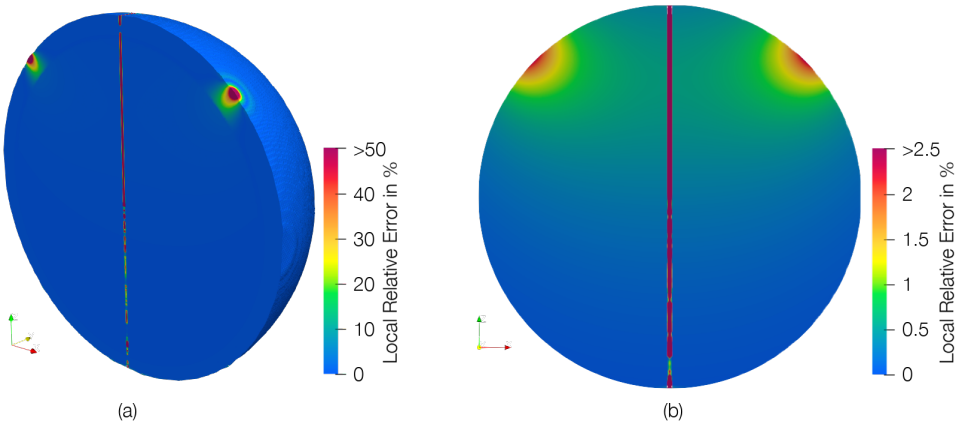

Figure 1.12.: Cross section of local RE in head (a) and brain (b)

1.6.4. Comparison for PEM between semi-analytical and numerical solutions

A numerical solution for the PEM was calculated for every electrode setup, using the finite element method and the toolbox Zeffiro Interface (2022), which was already mentioned earlier. The code was slightly modified since Zeffiro does not output the potential by default, only the current density. Looking at the local relative error between the numerical and semi-analytical solutions in figure 1.13, the large errors in the CSF and skull compartments are immediately noticeable. Table 1.4 shows that the relative errors in these layers are up to 30 percent for each electrode setup. Note that MAG and RDM errors are both large, meaning that the distribution of the potentials and their magnitude are both affected.

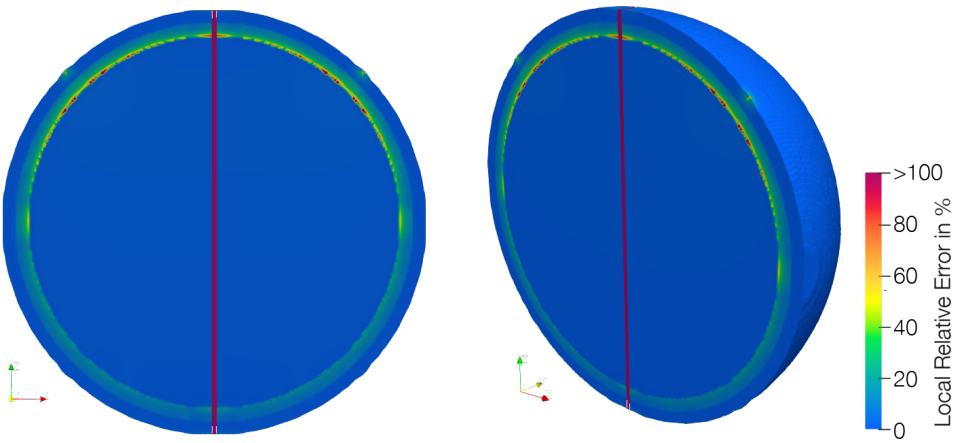

Figure 1.13.: Local RE of numerical and semi-analytical (reference) solutions

Setup	Measure	Total	Skin	Skull	CSF	Brain
(i)	RE%	10.01	4.75	17.28	30.22	1.86
	MAG%	5.56	1.57	15.16	17.29	1.82
	RDM%	8.20	4.45	7.72	22.88	0.36
(ii)	RE%	9.62	4.31	16.56	25.35	1.75
	MAG%	5.35	1.44	14.63	14.13	1.73
	RDM%	7.79	4.03	7.25	19.70	0.24
(iii)	RE%	10.55	5.85	17.50	34.12	2.05
	MAG%	5.60	1.66	15.30	20.12	1.96
	RDM%	8.70	5.57	7.90	25.14	0.62

Table 1.4.: Errors between numerical and analytical (reference) solution for PEM

There are three likely sources of error here: semi-analytical PEM implementation, mesh and FEM solver. Therefore we first compare the Zeffiro solution with the DUNEuro solution, using the mesh generated by Zeffiro. DUNEuro is a free open-source C++ software toolbox for the numerical computation of forward solutions in bioelectromagnetism (Schrader et al., 2021). To be precise the code from Erdbrügger (2021) was used. The differences for setup (i) are shown in table 1.5. We see that the differences are marginal and therefore it is save to say that the FEM solver is working properly.

	Total	Skin	Skull	CSF	Brain
RE	6.18×10^{-6}	3.35×10^{-6}	4.53×10^{-6}	2.26×10^{-5}	2.89×10^{-5}
MAG	-8.36×10^{-7}	-7.57×10^{-7}	-9.33×10^{-7}	-1.87×10^{-6}	-1.37×10^{-6}
RDM	6.12×10^{-6}	3.26×10^{-6}	4.43×10^{-6}	2.25×10^{-5}	2.88×10^{-5}

Table 1.5.: Errors between Zeffiro and DUNEuro (reference) solutions

Next a mesh from Lunkenheimer (2021) was used in order to compare the solution of the semi-analytical PEM implementation and the DUNEuro solution. Note that we use DUNEuro instead of Zeffiro, because it isn't possible to use external volume meshes with Zeffiro. The new mesh was coarser, namely consisting of 555289 nodes and 3194545 tetrahedrons with an average edge length of $1.63mm$, but was adapted to the geometry of the compartments. Therefore the surfaces in figure 1.14 look much smoother. The resulting errors shown in table 1.6 are far smaller than in table 1.4. The relative error in the skull decreased from 17.28 to 1.32 percent and in the CSF even from 30.22 to 0.62. This can also be seen in figure 1.15(a) where the ring-shaped error has disappeared. Notice the wavy pattern on the surface is due to the (truncated) series expansion used for the potential. With the DUNEuro solution and the geometry adapting mesh we obtain local relative errors of about 1 percent in the brain and in the brain areas underneath the electrodes even close to zero (1.15(b)).

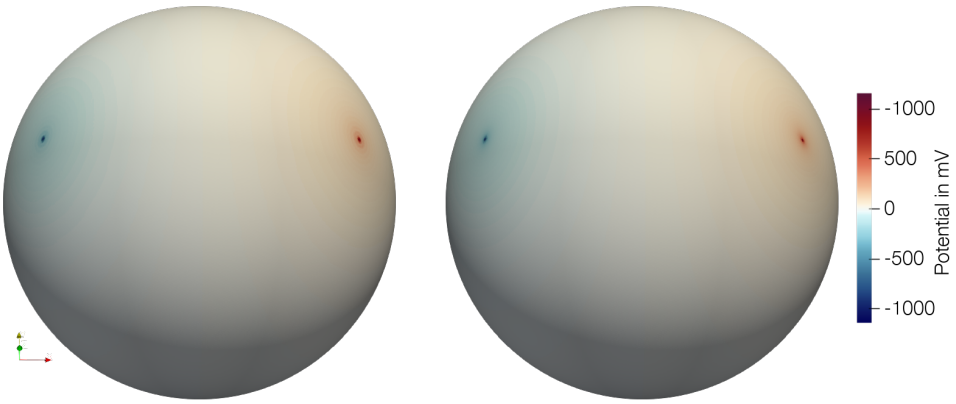

Figure 1.14.: Semi-analytical solution (l.), DUNEuro solution (r.).

	Total	Skin	Skull	CSF	Brain
RE%	3.76	4.34	1.32	0.62	0.60
MAG%	0.17	0.16	0.18	0.50	0.53
RDM%	3.75	4.33	1.31	0.37	0.29

Table 1.6.: Differences between DUNEuro and semi-analytical (reference) solution

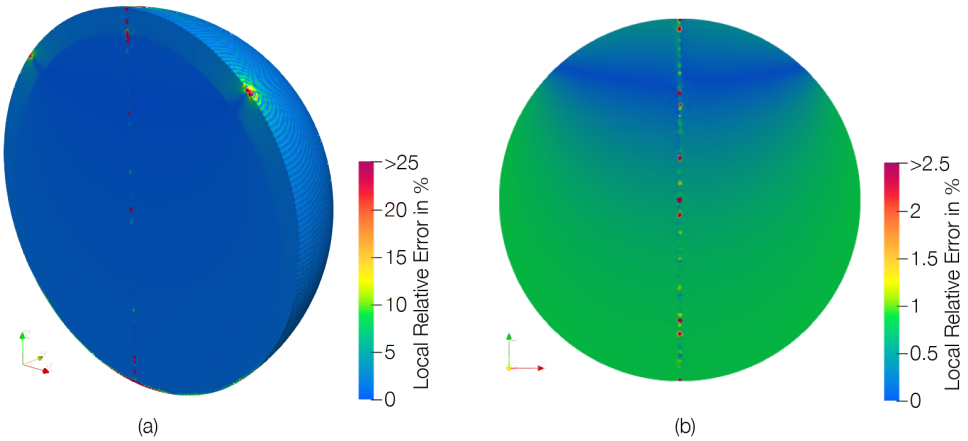

Figure 1.15.: Local RE of DUNEuro and semi-analytical (ref.) solutions in head (a) & brain (b)

We can conclude that the source of error is probably the mesh. This is supported by figure 1.16. The layers of the mesh are offset inward by up to 1 mm, which leads to these distortions. We could compensate this phenomenon by slightly inflating the sphere model. Since in our further analysis we will only use finite element solutions, which were all obtained from this shrunken model, we will assume the mesh to be correct and ignore this variational crime.

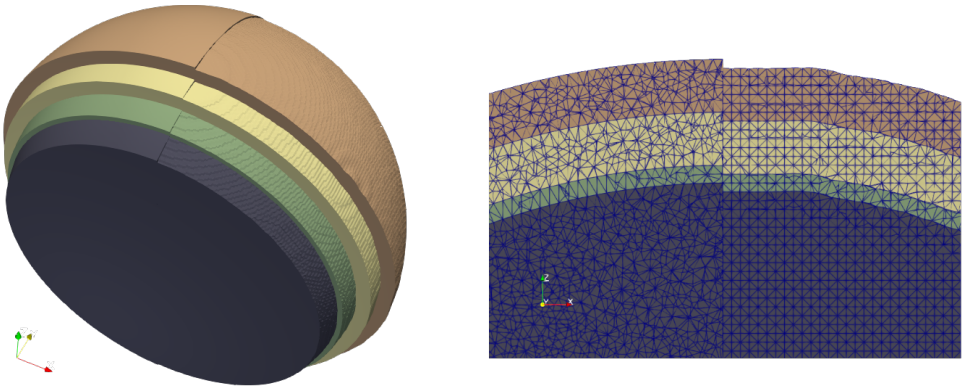

Figure 1.16.: Mesh from Lunkenheimer (2021) (l.) and Zeffiro (r.) side by side in (a) and (b)

1.6.5. Comparison for CEM between semi-analytical and numerical solutions

Unfortunately, the previous problem also occurs in the case of CEM. The values for CSF and skull layer in table 1.7 are nearly identical with table 1.4. The same is true for figures 1.17 and 1.13. This supports the hypothesis that the errors are due to the meshing.

Setup	Measures	Total	Skin	Skull	CSF	Brain
(i)	RE%	9.41	1.94	17.18	29.92	1.85
	MAG%	5.26	1.10	15.07	17.14	1.81
	RDM%	7.61	1.59	7.69	22.65	0.35
(ii)	RE%	9.06	1.86	16.47	25.14	1.74
	MAG%	5.12	1.07	14.56	14.04	1.72
	RDM%	7.29	1.52	7.21	19.52	0.23
(iii)	RE%	9.48	2.05	17.39	33.74	1.96
	MAG%	5.28	1.16	15.21	19.85	1.90
	RDM%	7.67	1.68	7.86	24.92	0.49

Table 1.7.: Errors of numerical and semi-analytical (ref.) CEM solutions

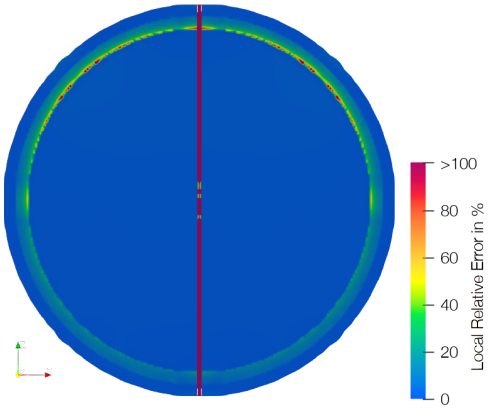

Figure 1.17.: Local RE for numerical & semi-analytical (ref.) CEM solutions

1.6.6. Comparison of numerical solutions for PEM and CEM

We want to investigate how the numerical solutions of the two models differ and in particular the current densities. As mentioned earlier, we consider the numerical solutions and the mesh separately from the initial problem. Hence we won't longer use the radii from table 1.1, but rather the mesh itself to delimit the tissues. Table 1.8 shows the differences between the potentials. Surprisingly, the values for the brain compartment are very similar to the analytical case (cf. table 1.3), even though there is this deviation in the domain and the conductivities. In the other interior compartments the situation is unambiguous, while the errors are lower in the CSF compartment, they're higher in the skull layer. Looking at figure 1.18 we see a familiar picture. The local relative error looks similar to the one of the analytic case 1.13. Again the solution for the PEM, but this time the numerical one, has higher magnitudes in the brain areas underneath the electrodes compared to the numerical CEM.

Setup	Measure	Total	Skin	Skull	CSF	Brain
(i)	RE%	10.28	11.81	4.58	0.61	0.50
	MAG%	2.19	2.50	1.50	0.43	0.39
	RDM %	9.94	11.40	4.29	0.43	0.30
(ii)	RE%	9.07	10.52	4.01	0.47	0.38
	MAG%	1.71	1.99	1.16	0.34	0.32
	RDM%	8.83	10.23	3.82	0.32	0.21
(iii)	RE%	11.03	12.54	5.16	0.80	0.65
	MAG%	2.60	2.91	1.87	0.55	0.49
	RDM%	10.58	12.03	4.76	0.58	0.42

Table 1.8.: Differences between numerical solution of PEM and CEM (ref.)

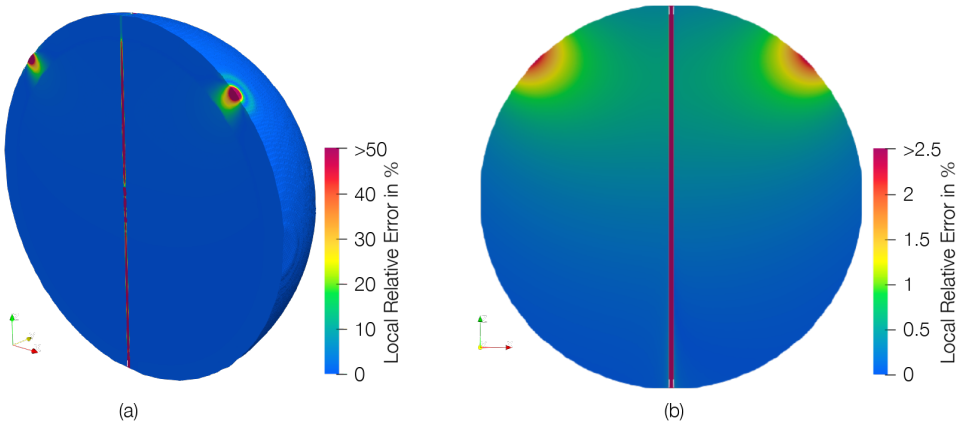

Figure 1.18.: Local RE for numerical PEM and CEM (ref.) solutions in head (a) and brain (b)

So far we only considered the different potentials, next we want to focus on the current density generated by the point and the complete electrode model. Figure 1.19 shows the current density for setup (i) of both models in a cross section. We see that the majority of the current flows through the skin and because of the low conductivity, only little passes through the skull. High magnitudes arise in the CSF due to the high conductivity. Comparing PEM and CEM, the significant differences only occur at the electrodes and the areas underneath. As one would expect the inflowing normal current density at the CEM electrode is spread out, while it is punctual for the point electrode (figure 1.20). Recall that we only derived the discretization for the PEM by formally applying the divergence theorem, hence this shows that the approach is

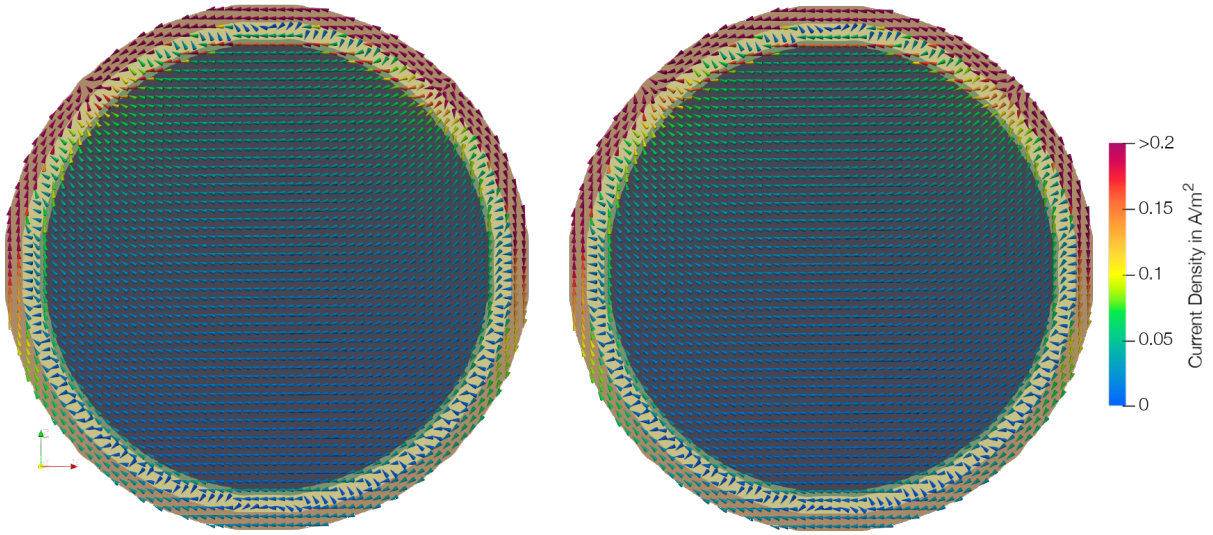

Figure 1.19.: Current density of PEM (l.) and CEM (r.)

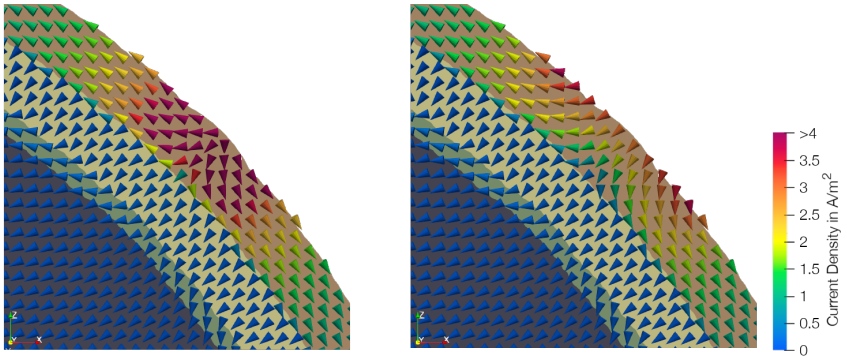

Figure 1.20.: Current density near an electrode for PEM (l.) and CEM (r.)

plausible. The point electrode causes high magnitudes in the underlying skin area, with values off the scale. These strongly decrease at the skull-skin interface. In the introduction of the complete electrode model, it was mentioned that high currents arise at the boundary of the electrodes. One can clearly see this phenomenon in figure 1.20, where magnitudes of $4A/m^2$ and above occur at the boundary and only of $2.5A/m^2$ in the center. This transfers to the underlying skin areas, hence high magnitudes arise in the skin at the boundary of the electrode and relative low ones under the center. This is a strong contrast to the PEM, where the highest values occur directly underneath. In both models, the current density decreases as it enters the skull. Nevertheless, the PEM still generates larger magnitudes as we see in figure 1.21. Looking closely, this also applies to the brain areas underneath.

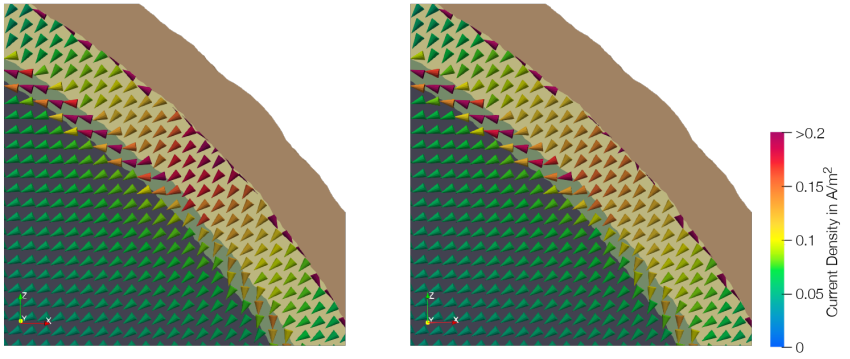

Figure 1.21.: Current density in the interior layers for PEM (l.) and CEM (r.)

To specify this more precisely we can introduce similar error resp. difference measures to the ones used before, by adapting them to vector valued functions. The corresponding values for PEM and CEM are shown in table 1.9. The distribution of the values behaves similar to what we saw for the potentials already. Note that we have omitted the skin layer in this table, because the difference are very large as expected. What could previously only be seen when looking closely, becomes clear in figure 1.22. The local relative error mainly arise at the brain areas underneath the electrodes. From figure 1.21 it seems like the orientation for PEM and CEM is very similar, which suggests that the current density of the PEM has a higher magnitude. That would mean with the PEM one could achieve higher intensities during stimulation.

Setup	Measure	Skull	CSF	Brain
(i)	RE%	7.83	2.06	1.07
	MAG%	2.30	0.89	0.59
	RDM%	7.40	1.85	0.88
(ii)	RE%	7.19	1.76	0.87
	MAG%	1.93	0.67	0.44
	RDM%	6.86	1.62	0.74
(iii)	RE%	8.47	2.40	1.34
	MAG%	2.74	1.16	0.78
	RDM%	7.91	2.09	1.08

Table 1.9.: Difference of current density for PEM and CEM (ref.)

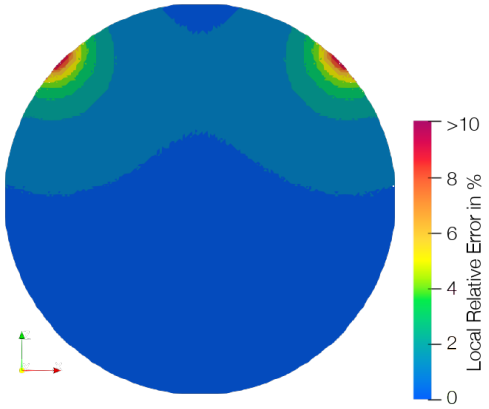

Figure 1.22.: Local RE for current density of PEM and CEM (ref.) in the brain

1.6.7. Convergence of CEM towards PEM for small electrodes

Until now we only considered electrodes with a radius of $1cm$. In section 1.3.3 we showed that under certain assumptions the potential of the CEM converges towards the potential of the PEM on relative compact subsets, when the electrodes decrease in size. Looking at figure 1.23 this clearly seems to be the case for the discretizations as well. The graphs show the relative error in the brain between the potential resp. the current density of the point electrode model and the complete electrode model corresponding to a certain electrode size. Only the setups (i) and (ii) were calculated and the PEM was chosen as a reference. When shrinking the electrodes, the potentials seem to converge in the H^1-norm. Note that the L^2-norm of the current density is equivalent to $\|\nabla u\|_{L^2}$, as the conductivity is piecewise constant and strictly positive. Moreover one can recognize the convergence rate h^2 from the graphs.

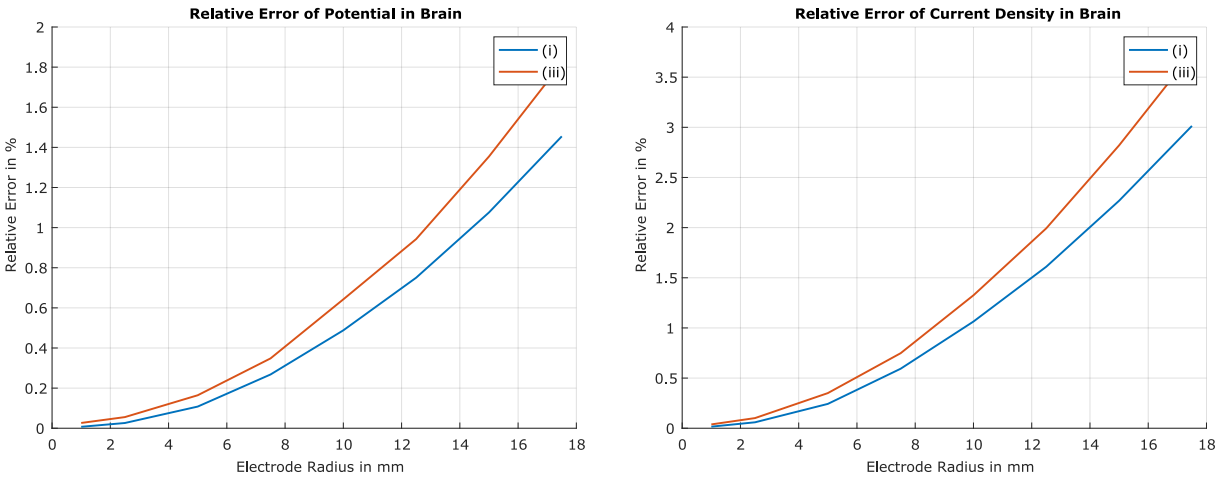

Figure 1.23.: RE between potential and current density of the PEM and the CEM for different electrode sizes

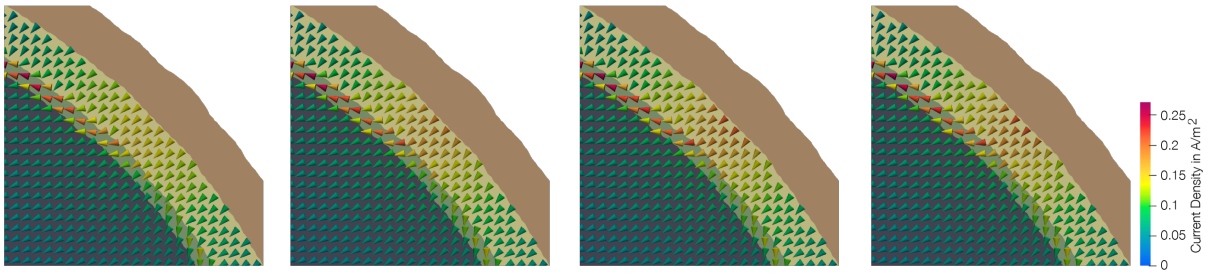

Figure 1.24.: Current density in the interior compartments for CEM with electrode size 10, 5, 1 mm and for the PEM (l. to r.)

From figure 1.24 we see that smaller electrodes (with the same current injection) produce a current density in the skull which is more concentrated and with higher magnitudes resulting in a higher current density in the underlying brain area.

We can conclude that there are small but noticeable differences between the potentials generated by PEM and CEM in both the analytical and numerical cases. For the numerical case, we have also seen that similar differences occur with the current density. These differences were mainly located underneath the electrode and mainly effected the corresponding superficial areas of the brain. Therefore, this could be important for stimulation of superficial targets. It appears that the point electrode model may cause higher intensities in deeper regions because the current density is more concentrated. By using smaller electrodes in CEM, the resulting (discretized) potentials and current densities approach the (discretized) solutions of the point electrode model, which means that smaller electrodes can also cause higher intensities in the brain regions mentioned above.

2. The Optimization Problem

The conventional way to apply electric currents on the scalp (mostly $\leq 2\,mA$) is by using a pair of two large patch-like sponge electrodes. For somato-motor applications one electrode is placed over the primary motor or somatosensory cortex and the other one over the supraorbital area. Anodal stimulation right over the target enhances cortical excitability, whereas cathodal stimulation inhibits it (Nitsche and Paulus, 2000). This simple approach neglects some important aspects of the stimulation. The neurobiological effects of tDCS depend on the magnitude of the electric field and it's direction with respect of the stimulated neuronal structure in the target area. Hence not taking into account individual anatomies can lead to suboptimal results. Besides focusing on the location of the target, it is further important to consider it's orientation (Creutzfeldt et al., 1962). Additionally, the individual anatomical features of head tissues lead to variations of the created electric field. Therefore an accurate volume head model is essential in improving individual tDCS efficacy. Dmochowski et al. (2011) used a multi-channel array consisting of 64 fixed electrode locations to calculate optimized stimulation montages for presumed target regions. Compared with conventional electrode, montages their optimization approach achieved electric fields, which exhibit simultaneously greater focality and target intensity at cortical targets using the same total current. In short, optimal targeting should not only try to maximize the injected current in the target region in the brain (intensity) and minimize it in other areas (focality), but also generate it as parallel (excitation) or anti-parallel (inhibition) to the target direction (directionality) as possible. Hence we obtain an optimal control problem, which in its most general form can probably be stated as follows

$$\min_{(u,y)\in U\times Y} J(u,y) \quad \text{subject to} \quad e(u,y)=0,\ c(u,y)\in K,\ (u,y)\in C,$$

where $J : U \times Y \to \bar{\mathbb{R}} = \mathbb{R} \cup \infty$ is the objective function, $e : U \times Y \to Z$ and $c : U \times Y \to R$ are operators, U, Y, Z, R real Banachspaces, $K \subset R$ a closed convex cone and $C \subseteq U \times Y$ a closed convex set. Herein $e(u, y)$ describes the boundary value problem, i.e. the relation between the state of the system u and the boundary control y. Using the CM as an example we derive $U = H^1(\Omega),\ Y = H^{-\frac{1}{2}}(\Gamma),\ Z = U \times Y$ with $e(u, y) = (\operatorname{div} \sigma\nabla u, \sigma\nabla u \cdot \nu - y)$. Recall that all three boundary value problems, we discussed in chapter 1, were linear and well-posed. Hence for every control y there exists a unique state u with $e(u, y) = 0$ and $y \mapsto u = y(u)$ is linear and continuous. Therefore the problem is only dependent on the control variable y. We can rewrite

$$\min_{y\in Y} J(y) \quad \text{subject to} \quad c(y)\in K,\ (u(y),y)\in C \tag{2.1}$$

for modified J and c. The condition $c(u, y) \in K$ can be interpreted as an abstract inequality constraint and could model safety conditions. The set C will model Kirchhoff's law $\langle y, 1\rangle = 0$ and could further model safety constraints as well. We will be able to formulate our constraints in the form of $(u, y) \in C$ and hence we will omit the other condition involving the convex cone. The objective function strongly depends on the treatment goal and could range from maximum intensity to maximal focality. Notice that we can easily translate a maximization problem into a minimization problem by considering $-J$ instead.

Definition 20. We call $y \in Y$ a feasible control if y satisfies all conditions of (2.1). Further y is an optimal control of (2.1) if it is feasible and $J(y) \leq J(\tilde{y})$ for all other feasible $\tilde{y} \in Y$.

When using the point electrode model or the complete electrode model it is plausible to assume that the electrode positions are fixed e.g. due to given positions in the electrode cap. Therefore the problem reduces to a finite dimensional optimization problem. We will impose two safety constraints during this chapter. We limit the total current injected, i.e. $\|I\|_1 \leq C_1$ and the maximal current injected per electrode, i.e. $\|I\|_\infty \leq C_2$, where $I \in \mathbb{R}^L$. To satisfy Kirchhoff's law we further impose $\sum_{m=1}^{L} I_m = 0$, i.e. $I \in \mathbb{R}^L_\diamond$. In our cases the objective function is linear or convex and we obtain a convex optimization problem. Therefore we will give a brief recap of convex optimization.

2.1. Mathematical Basics

A function $f : \mathbb{R}^n \to \bar{\mathbb{R}}$ is convex if for all $\lambda \in (0,1),\ x, y \in \mathbb{R}^n$

$$f(\lambda x + (1-\lambda)y) \leq \lambda f(x) + (1-\lambda) f(y)$$

and strictly convex if the inequality is strict. A subset $C \subseteq \mathbb{R}^n$ is convex, if

$$\lambda x + (1-\lambda)y \in C \quad \forall \lambda \in (0,1)\ x, y \in C.$$

We call $z \in C$ extreme point of C if z does not lie between points of C, i.e.

$$z = \lambda x + (1-\lambda)y \text{ for } \lambda \in (0,1),\ x, y \in C \quad \Rightarrow \quad x = y = z.$$

We denote the convex hull of a set $S \subseteq \mathbb{R}^n$ by $\operatorname{conv} S$. It is defined as the unique minimal convex set containing S. The theorem of Minkowski states that a non-empty compact convex set $K \subset \mathbb{R}^n$ is the convex hull of its extreme points, i.e. $\operatorname{conv}(\operatorname{ext} K) = K$ (Brøndsted, 2012, Thm 5.10). Notice that this is also true in general Hausdorff locally convex topological vector spaces, if we replace the convex hull by its closure (Rudin, 1991, Thm. 3.23).
The epigraph of a convex function is given by

$$\operatorname{epi} f = \{(x,t) \in \mathbb{R}^n \times \mathbb{R} : f(x) \leq t\}.$$

Note that f is convex if and only if $\operatorname{epi} f$ is convex as well and that f is lower semi continuous if and only if $\operatorname{epi} f$ is closed. The domain of a function $f : \mathbb{R}^n \to \bar{\mathbb{R}}$ is the set

$$\operatorname{dom} f = \{x \in \mathbb{R}^n : f(x) < \infty\}.$$

The standard form of a (finite dimensional) convex optimization problem is

$$\begin{aligned} \min_{x \in \mathbb{R}^n} f_0(x) \quad & \text{subject to} \quad c_E(x) = 0,\ c_I(x) \leq 0 \\ & c_I = (f_1, \ldots, f_m)^T : \mathbb{R}^n \to \bar{\mathbb{R}}^m \\ & c_E = (h_1, \ldots, h_p)^T : \mathbb{R}^n \to \bar{\mathbb{R}}^p, \end{aligned} \tag{2.2}$$

where $f_0, f_1, \ldots, f_m$ are convex and $h_1, \ldots h_p$ are affine. $c_I(x) \leq 0$ has to be understood component wise. The domain of the problem is

$$\mathcal{D} = \bigcap_{i=0}^{m} \operatorname{dom}\ f_i \cap \bigcap_{i=1}^{p} \operatorname{dom}\ h_i.$$

A problem, which is equivalent to a convex problem, can also be considered as a convex optimization problem. A point $x \in \mathcal{D}$ is called feasible if it satisfies all constraints and strictly feasible when $c_I(x) < 0$. We denote the set of feasible points by $\mathcal{C}$. Moreover the problem is called feasible if there exists a feasible point and otherwise infeasible. The optimal value of the

problem is $p^* = \inf\{f_0(x) : x \in \mathcal{C}\}$. For an infeasible problem we have $p^* = \infty$. If $p^* = -\infty$ we say that the problem is unbounded (from below). As a special case of the above definition $x \in \mathcal{C}$ is called optimal when $f_0(x) \leq f_0(\tilde{x})$ for all $\tilde{x} \in \mathcal{C}$, i.e. $f(x) = p^*$. Furthermore $x \in \mathcal{C}$ is called locally optimal, if it is optimal in a small neighborhood. Assuming f_0 is convex, then locally optimal points are globally optimal. Moreover, if f_0 is strictly convex, then optimal points are unique. To see this first notice that the feasible domain is convex. Now assume that J is convex and x is locally optimal but not globally, i.e. it exists $y \in \mathcal{C}$ with $J(y) < J(x)$. But $z_\lambda = \lambda x + (1-\lambda)y \in \mathcal{C}$ for $\lambda \in (0,1)$ and $f(z_y) \leq \lambda f(x) + (1-\lambda)f(y) < f(x)$. Then we see that x can't be locally optimal by choosing λ small enough. For the other claim assume f_0 is strictly convex and $x \neq y$ are optimal. Then $f_0(\frac{1}{2}x + \frac{1}{2}y) < \frac{1}{2}f_0(x) + \frac{1}{2}f_0(y)$, which contradicts the optimality and hence $x = y$.
The Lagrange function to the above minimization problem $\mathcal{L} : \mathbb{R}^n \times \mathbb{R}^m \times \mathbb{R}^p \to \bar{\mathbb{R}}$ is defined

$$\mathcal{L}(x, \mu, \lambda) = f_0(x) + \mu^T c_I(x) + \lambda^T c_E(x), \quad \text{dom } \mathcal{L} = \mathcal{D} \times \mathbb{R}^m \times \mathbb{R}^p.$$

The variables μ, λ are called dual variables and

$$g : \mathbb{R}^m \times \mathbb{R}^p \to \mathbb{R}, \quad g(\mu, \lambda) = \inf_{x \in \mathcal{D}} \mathcal{L}(x, \mu, \lambda)$$

is the (Lagrange-) dual function. It is concave, so. $-g$ is convex. To see this, first note that $\mathcal{L}$ is linear resp. convex in the dual variables and $-g = \sup_{x \in \mathcal{D}} \mathcal{L}(x, \cdot, \cdot)$. With the help of the epigraph one can show that the pointwise supremum of convex functions is again convex. The dual functions yields a lower bound for the optimal value p^*. Let $\mu \geq 0$, $\lambda \in \mathbb{R}^p$ and $x \in \mathcal{C}$. Then we have

$$g(\mu, \lambda) \leq L(x, \mu, \lambda) = f_0(x) + \mu^T c_I(x) + \lambda^T c_E(x) \leq f_0(x).$$

Thus we obtian $g(\mu, \lambda) \leq \inf_{x \in \mathbb{C}} f_0(x) = p^*$. Therefore the dual problem is defined as

$$\max_{\substack{\mu \in \mathbb{R}^m, \lambda \in \mathbb{R}^p \\ \mu \geq 0}} g(\mu, \lambda),$$

where in this case dom $g = \{(\mu, \lambda) \in \mathbb{R}^m \times \mathbb{R}^p : g(\mu, \lambda) > -\infty\}$. The pair (μ, λ) is called dual feasible if $(\mu, \lambda) \in$ dom g and $\mu \geq 0$ and dual-optimal when it solves the dual problem. Notice that the dual problem is a convex problem. This is even true, if the initial problem isn't convex.We denote the optimal value of the dual problem by d^*, then we get $d^* \leq p^*$. This property is called weak duality. In the case of $d^* = p^*$ one speaks of strong duality.
Let $f : W \times Z \subseteq \mathbb{R}^n \times \mathbb{R}^m \to \mathbb{R}$. A point $(\bar{w}, \bar{z}) \in W \times Z$ is called saddle point for f, W and Z if $f(\bar{w}, z) \leq f(\bar{w}, \bar{z}) \leq f(w, \bar{z})$ for all $(w, z) \in W \times Z$, i.e.

$$f(\bar{w}, \bar{z}) = \inf_{w \in W} f(w, \bar{z}) = \sup_{z \in Z} f(\bar{w}, z).$$

In general the max-min inequality holds

$$\sup_{z \in Z} \inf_{w \in W} f(w, z) \leq \inf_{w \in W} \sup_{z \in Z} f(w, z).$$

We say that f, W, Z have the strong max-min or saddle point property, if equality holds in the above inequality. When a saddle point exists, then the saddle point property holds. Notice that strong duality is equivalent to $\mathcal{L}$ having the saddle point property on $\mathcal{D} \times \mathbb{R}^m_{\geq 0} \times \mathbb{R}^p$. Furthermore if μ^*, λ^* are dual optimal and x^* (primal) optimal and strong duality holds, then they form a saddle point for the Lagrangian. Conversely, when $(x, \mu, \lambda) \in \mathcal{D} \times \mathbb{R}^m_{\geq 0} \times \mathbb{R}^p$ is a saddle point of the Lagrangian, then they are primal resp. dual optimal.

We define the affine hull of a set $C \subseteq \mathbb{R}^n$ to be the smallest affine set in $\mathbb{R}^n$ that contains C and denote it $\operatorname{aff} C$. The affine dimension of a set is defined as the dimension of its affine hull. We can define the relative interior of set C by

$$\operatorname{relint} C = \{x \in C : B(x, r) \cap \operatorname{aff} C \subseteq C \text{ for some } r > 0\},$$

with $B(x, r)$ being the ball with radius r centered at x.
Slater's condition is a sufficient condition for strong duality to hold for a convex optimization problem (2.2). Assume that $f_0, \ldots, f_k$ are convex and $f_{k+1}, \cdots, f_m$ affine. If the problem is bounded from below and there exists a feasible point $x \in \operatorname{relint} \mathcal{D}$, which is strictly feasible for $f_0, \ldots, f_k$, then strong duality holds and furthermore there exists dual optimal variables μ^*, λ^* (Rockafellar, 1970, Thm. 28.2). We refer to Boyd and Vandenberghe (2004) for more information on convex optimization.

2.2. Optimization Approaches

We want to focus on different maximum intensity approaches (cf. Dmochowski et al., 2011; Fernández-Corazza et al., 2020; Khan et al., 2022). The primary goal is to generate the strongest possible current density in a target area along a specific direction. This is achieved by the objective function

$$\int_\Omega \langle AI, e\rangle \, dx,$$

where $e \in L^2(\Omega, \mathbb{R}^3)$, specifies the target direction and $A : I \mapsto \sigma\nabla u$ is the forward model obtained from CEM or PEM, respectively. For each of the electrode models we assume that the conditions of the section (1.3.2) resp. (1.3.1) hold. In order to be well defined in the PEM case, we assume that e is zero near the boundary, i.e. there exists $\Omega_0 \Subset \Omega$ with $\operatorname{supp} e \subset \Omega_0$. Note that since we are only interested in ∇u, it does not matter which representative of u is chosen. For the CEM it follows from theorem 14

$$\|\nabla u\|_{L^2(\Omega)} \leq C\|I\|_2.$$

Similar to the end of the proof of theorem 18, we can derive for the PEM the existence of $C > 0$ with

$$\|u\|_{H^1(\Omega_0)/\mathbb{R}} \leq C\|I\|_2$$

and thus $\|\nabla u\|_{L^2(\Omega_0)} \leq C\|I\|_2$. In both cases we obtain

$$\Big| \int_\Omega \langle AI, e\rangle \, dx \Big| \leq \|AI\|_{L^2(\Omega_0)}\|e\|_{L^2(\Omega_0)} \leq C\|\sigma\|_{L^\infty(\Omega)}\|\nabla u\|_{L^2(\Omega_0)}\|e\|_{L^2(\Omega_0)} \leq C\|I\|_2.$$

For $I \notin \mathbb{R}^L_\diamond$ we define the objective function to be ∞. The basic maximum intensity approach (MI) reads as follows

$$\max_{I \in \mathbb{R}^L} \int_\Omega \langle AI, e\rangle \, dx \quad \text{subject to} \quad \|I\|_1 \leq C_1, \ \sum_{m=1}^{L} I_m = 0.$$

Since the feasible domain is compact and the objective function is continuous, this problem admits a solution. The next corollary follows directly from Minkowski's theorem.

Corollary 21. Let $f : K \to \mathbb{R}$ be convex and $K \subset \mathbb{R}^m$ convex and compact. Then

$$\max_K f = \max_{\operatorname{ext} K} f.$$

Proof. The inequality $\geq$ is obvious. For the converse assume $z \notin \operatorname{ext} K$ to be optimal. According to the theorems mentioned above, we can find $\lambda \in (0,1)$ and $x \neq y \neq z$ with $z = \lambda x + (1-\lambda)y$. Thus

$$f(z) \leq \lambda f(x) + (1-\lambda) f(y) \leq \max_{\operatorname{ext} K} f.$$

□

Since the objective function of the MI is linear, the previous corollary tells us that the set of maximizers will be a face of the convex polytope formed by the side constraints. Note that we'll always find an optimal x at one of the vertices. This fact is exploited by algorithms for linear problems.

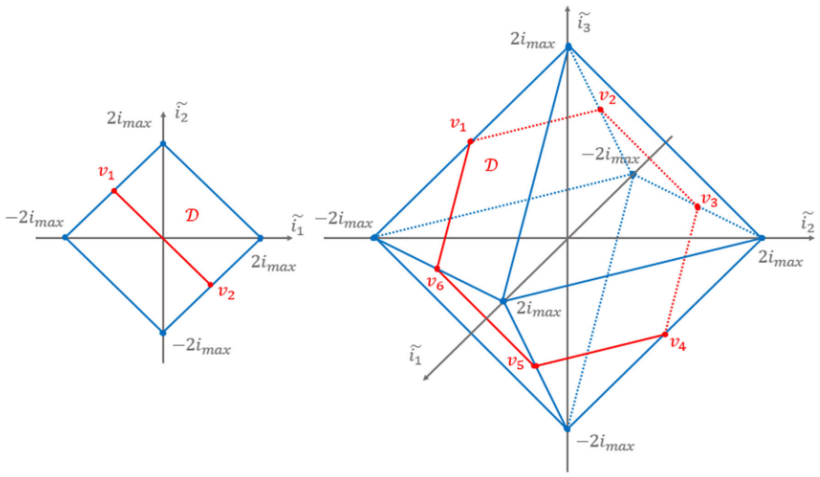

Figure 2.1.: Feasible domain of MI for 2 (l.) and 3 (r.) electrodes with $C_1 = 2i_{\max}$ is given by the convex hull of the points v_i (Fernández-Corazza et al., 2020)

In the case of $\|I\|_1 \leq C_1$ and $\sum_{m=1}^{L} I_m = 0$ the vertices are of the form $\frac{C_1}{2}(e_j - e_i)$ for $i \neq j$, where e_i, e_j denote the standard unit vectors in $\mathbb{R}^L$ (Fernández-Corazza et al., 2020, B.1). Since it is likely that the face of optimizers will only be a vertex or that the algorithm will pick the vertex, the currents will be injected only through two electrodes, which can cause discomfort and pain at the skin due to the relatively high amperage. In order to prevent this, one can further impose an injection limit per electrode, i.e. $\|I\|_\infty \leq C_2$. This approach is called Constraint Maximum Intensity (CMI). Since the feasible domain remains compact, a solution to the problem exists and moreover the set of optimal points will be a face again. As shown by Fernández-Corazza et al. (2020), if the restriction by the new constraint isn't strong enough the solution will remain sparse. To gain more control one could introduce weights $\|wI\|_\infty \leq C_2$, which is equivalent to limiting each electrode individually. This would mean extra effort and require additional information for the user. Furthermore uniqueness of the optimizer isn't guaranteed.
A more user friendly approach is the Distributed Constraint Maximum Intensity approach (DCMI). It is stated as

$$\max_{I \in \mathbb{R}^n} \int_\Omega \langle AI, e \rangle \, dx - \lambda \|I\|_2^2 \quad \text{subject to} \quad \|I\|_1 \leq C_1, \|I\|_\infty \leq C_2, \ \sum_{m=1}^{L} I_m = 0$$

for $\lambda > 0$. We will reformulate the problem into an equivalent minimization problem

$$\min_{I \in \mathbb{R}^n} \int_\Omega \langle AI, -e \rangle \, dx + \lambda \|I\|_2^2 \quad \text{subject to} \quad \|I\|_1 \leq C_1, \|I\|_\infty \leq C_2, \ \sum_{m=1}^{L} I_m = 0.$$

Using the same reasoning as before, this approach obviously has an optimizer. This time it is unique, because adding $\lambda \| \cdot \|^2$ to the objective function makes it strictly convex. Note that

$I = 0$ can't be optimal, unless $A = 0$, $e = 0$, $C_1 = 0$ or $C_2 = 0$. We will exclude all of these trivial cases. To see how the additional penalty term works and why this approach deserves its name, we need the following lemma from Kloft et al. (2011).

Lemma 22. Let $f, g : C \to \mathbb{R}$ be convex and $C \subset \mathbb{R}^n$ a convex set. We can consider the two convex optimization problems

$$\min_{x \in C} f(x) + \sigma g(x) \tag{2.3}$$

and

$$\min_{x \in C} f(x) \quad \text{subject to} \quad g(x) \leq \tau. \tag{2.4}$$

If $x^* \in C$ is optimal for the first problem with $\sigma \geq 0$, then we can find $\tau \in \mathbb{R}$, such that x^* is optimal for the second problem, e.g. $\tau = g(x^*)$. Conversly if Slater's conditions holds for (2.4) and $x^* \in C$ is optimal, then we can find $\sigma \geq 0$ such that x^* is optimal for the first problem. Furthermore we have $\sigma > 0$, if the condition $g(x^*) \leq \tau$ is binding in the sense that

$$\min_{x \in C} f(x) < \min_{x \in C, g(x) \leq \tau} f(x).$$

Proof. Fix $\sigma \geq 0$ and let $x^* \in C$ be optimal for the first problem. We set $\tau = g(x^*)$ and assume that x^* isn't optimal for the resulting second problem. Hence we can find $\tilde{x} \in C$ with $g(\tilde{x}) \leq \tau$ and $f(\tilde{x}) < f(x^*)$. Therefore

$$f(\tilde{x}) + \sigma g(\tilde{x}) < f(x^*) + \sigma g(x^*),$$

which is a contradiction. Thus x^* is optimal for (2.4). Now let $\tau \in \mathbb{R}$ be given and x^* optimal for the second problem. The Lagrangian reads

$$\mathcal{L}(x, \sigma) = f(x) + \sigma(g(x) - \tau), \quad x \in C, \sigma \geq 0.$$

Since Slater's conditions is satisfied, strong duality holds and there exists a dual optimal variable $\sigma^* \geq 0$. We know that (x^*, σ^*) is a saddle point of $\mathcal{L}$. Therefore $\mathcal{L}(x^*, \sigma^*) = \min_{x \in C} L(x, \sigma^*)$ or

$$f(x^*) + \sigma^*(g(x^*) - \tau) = \min_{x \in C} f(x) + \sigma^*(g(x) - \tau). \tag{2.5}$$

Removing the constant term $\sigma^* \tau$ yields $f(x^*) + \sigma^* g(x^*) = \min_{x \in C} f(x) + \sigma^* g(x)$. Now assume that the condition is binding. Then x^* does not minimize f over C. Looking at (2.5), we see that therefore $\sigma^* > 0$, otherwise we would obtain a contradiction. □

We can apply this to the DCMI approach with

$$C = \{x \in \mathbb{R}^L : \|x\|_1 \leq C_1,\ \|x\|_\infty \leq C_2,\ \sum_{m=1}^{L} I_m = 0\}$$

$$f(x) = \int_\Omega \langle AI, e \rangle \, dx \quad \text{and} \quad g(x) = \|x\|_2^2.$$

Obviously (2.3) is our DCMI formulation. Since $I = 0$ can't be a minimizer, we get $\tau > 0$. Therefore $0 \in \operatorname{relint} C$ is strictly feasible and (2.4) satisfies Slater's condition. By the above lemma, we know that there exists $C_3 > 0$ such that we can equivalently formulate the DCMI approach as

$$\min_{I \in \mathbb{R}^n} \int_\Omega \langle AI, -e \rangle \, dx \quad \text{subject to} \quad \|I\|_1 \leq C_1, \|I\|_\infty \leq C_2,\ \sum_{m=1}^{L} I_m = 0,\ \|I\|_2 \leq C_3.$$

We further know that $C_3 = \|I_\lambda^*\|_2$ is a suitable choice, where I_λ^* is the minimizer of the initial problem. Without knowledge of this minimizer, the constant $C_3 > 0$ is unknown as well, but

the mere existence of such a constant is sufficient. For the MI and CMI approach, the optimal point can and probably will be found at a vertex of the feasible domain, which is some sort of polytope. The additional condition $\|I\|_2 \leq C_3$ intersects the feasible domain with a ball of radius C_3. The boundary of the ball is exactly the set of it's extreme points. Heuristically, by adding this condition, one tries to restrict the feasible range in a way that increases the number of extreme points and the probability that the optimal point is no longer sparse. So far it might be possible that C_3 is too large, so it doesn't restrict the feasible domain. But by increasing λ we can enforce this, as the next two lemmas show.

Lemma 23. Let $f, g : C \to \mathbb{R}$ be convex and $C \subset \mathbb{R}^n$ a convex set. Now let $\sigma^* < \tilde{\sigma}$ and denote the corresponding optimal solutions of problem (2.4) by x^* and $\tilde{x}$. Then $g(\tilde{x}) \leq g(x^*)$.

Proof. Assume otherwise $g(x^*) < g(\tilde{x})$. Obviously we can derive

$$f(x^*) + \sigma^* g(x^*) \leq f(\tilde{x}) + \sigma^* g(\tilde{x}) \quad \text{and} \quad f(\tilde{x}) + \tilde{\sigma} g(\tilde{x}) \leq f(x^*) + \tilde{\sigma} g(x^*).$$

Combining these two yields

$$f(\tilde{x}) + \tilde{\sigma} g(\tilde{x}) \leq f(\tilde{x}) + \sigma^* g(\tilde{x}) - \sigma^* g(x^*) + \tilde{\sigma} g(x^*)$$

and therefore

$$0 \leq (\sigma^* - \tilde{\sigma}) g(\tilde{x}) + (\tilde{\sigma} - \sigma^*) g(x^*) < (\sigma^* - \tilde{\sigma}) g(\tilde{x}) + (\tilde{\sigma} - \sigma^*) g(\tilde{x}) = 0.$$

□

Lemma 24. Let $f, g : C \to \mathbb{R}$ be convex and $C \subset \mathbb{R}^n$ a convex set. Further assume f to be bounded from below. Let $\sigma_k \geq 0$ and $\sigma_k \to \infty$. Denote the corresponding optimal point for (2.4) by $x_k \in C$. Then it follows $g(x_k) \to \inf_{x \in C} g(x)$.

Proof. The previous lemma shows that $g(x_k)$ is monoton decreasing. Therefore we get

$$\inf_{k \in \mathbb{N}} g(x_k) = \lim_{k \to \infty} g(x_k). \tag{2.6}$$

Now assume that $\inf_{k \in \mathbb{N}} g(x_k) > \inf_{x \in C} g(x)$. We can choose $\varepsilon > 0$ and $x^* \in C$ with $\inf_{k \in \mathbb{N}} g(x_k) > g(x^*) + \varepsilon$. From the definition we know

$$f(x_k) + \sigma_k g(x_k) \leq f(x) + \sigma_k g(x) \quad \forall x \in C,\ k \in \mathbb{N}.$$

We can write

$$f(x_k) + \sigma_k g(x_k) = f(x^*) + \sigma_k g(x^*) + f(x_k) - f(x^*) + \sigma_k (g(x_k) - g(x^*)). \tag{2.7}$$

Note that $g(x_k) - g(x^*) > \varepsilon$, hence

$$f(x_k) + \sigma_k g(x_k) > f(x^*) + \sigma_k g(x^*) + f(x_k) - f(x^*) + \sigma_k \varepsilon.$$

Since f is bounded from below, there exists $C > 0$ with $f(x_k) - f(x^*) > -C$ for all $k \in \mathbb{N}$. Thus we get

$$f(x_k) + \sigma_k g(x_k) > f(x^*) + \sigma_k g(x^*) - C + \sigma_k \varepsilon.$$

Notice that $\varepsilon > 0$ and x^* are independent of k, hence for large $k \in \mathbb{N}$ we get $-C + \sigma_k \varepsilon > 0$ and therefore

$$f(x_k) + \sigma_k g(x_k) > f(x^*) + \sigma_k g(x^*).$$

But this is a contradiction to (2.6). □

Coming back to the DCMI approach, this means that if we increase λ, then C_3 will decrease and converge to 0. Hence at some point the additional constraint will be binding and the optimum will be an extreme point of $B_{C_3}(0)$. Note that there are a few cases in which the minimizer will stay sparse and an increase in λ will only reduce it's norm, but this is also the case in the CMI approach. Obviously there are weights, such that the optimizer of the DCMI is also an optimizer of the weighted CMI, namely $w_i = \frac{C_2}{|I_i^*|}$ if $I_i^* \neq 0$ and $w_i = \infty$ otherwise, but in general the optimizer remains ambiguous. In practical application the DCMI approach further has the benefit, that there is only one parameter to control, instead of a weight for each electrode.

2.3. Convergence of CEM towards PEM optimizers for small electrodes

In section 1.3.3 we proved that (under mainly geometrical assumptions) the potential of the CEM converges towards the potential of the PEM in the $H^1/\mathbb{R}$ on relative compact subsets, when the electrodes shrink. To be more precise we showed that for $\Omega_0 \Subset \Omega$ there exists $C > 0$ independent of h with

$$\|u - u^h\|_{H^1(\Omega_0)/\mathbb{R}} \leq Ch^2\|I\|_2$$

for $I \in \mathbb{R}^L_\diamond$ and small h. We can use this result and prove that the optimizers for the CEM (or at least a subsequence) converge towards the optimizer of the PEM as well. Therefore impose the same assumptions as in section 1.3.3. Recall that e from our optimization approach vanishes near the boundary, i.e. supp $e \subset \Omega_0 \Subset \Omega$. Using the Cauchy-Schwarz inequality we get

$$\Big| \int_\Omega \langle \sigma \nabla u, e\rangle \, dx - \int_\Omega \langle \sigma \nabla u^h, e\rangle \, dx \Big| = \int_{\Omega_0} \langle \sigma \nabla (u^h - u), e\rangle \, dx \leq \|\sigma\|_{L^\infty(\Omega)} \|\nabla(u^h - u)\|_{L^2(\Omega_0)} \|e\|_{L^2(\Omega)}$$

thus

$$\Big| \int_\Omega \langle \sigma \nabla u, e\rangle \, dx - \int_\Omega \langle \sigma \nabla u^h, e\rangle \, dx \Big| \leq Ch^2 \|e\|_{L^2(\Omega)} \|I\|_2. \tag{2.8}$$

Hence if the feasible domain is bounded, then the objective function of the CEM converges uniformly to the objective function belonging to the PEM.

Definition 25. Let X be a first countable topological space. We say that a sequence of functions $f_j : X \to \bar{\mathbb{R}}$ Γ-converges in X to $f : X \to \bar{\mathbb{R}}$, if for all $x \in X$ we have

1. $\forall (x_j)_j \subset X$ with $x_j \to x : f(x) \leq \liminf\limits_{j\to\infty} f_j(x_j)$
2. $\exists (x_j)_j \subset X$ with $x_j \to x : f(x) \geq \limsup\limits_{j\to\infty} f_j(x_j)$.

The functions $(f_j)_j$ are called equicoercive if there exists a sequentially compact set $C \subseteq X$ with $\arg\min f_j \subseteq C$ for all $j \in \mathbb{N}$.

Corollary 26. If $(f_j)_j$ Γ-converges to f and $(f_j)_j$ are equicoercive, then any sequence of minimizers $x_j \in \arg\min f_j$ contains a subsequence converging towards a minimizer of f.

Proof. Since $(f_j)_j$ are equicoercive, there exists a subsequence of $(x_j)_j$, denoted by $(x_j)_j$ as well, which converges to $x^* \in C$. Let $x \in X$ be arbitray. Because $(f_j)_j$ Γ-converges to f, there exists a sequence $(\tilde{x}_j)_j \in X$ with $\tilde{x}_j \to x$ and

$$f(x) \geq \limsup_{j\to\infty} f_j(\tilde{x}_j) \geq \limsup_{j\to\infty} f_j(x_j) \geq \liminf_{j\to\infty} f_j(x_j) \geq f(x^*).$$

□

We have already shown that the objective functions of MI, CMI and DCMI for CEM uniformly converge to the respective objective function of the PEM on the corresponding feasible domain $\mathcal{C} \subset \mathbb{R}^L$. Therefore we have Γ-convergence on $\mathcal{C}$ (with respect to the 2-norm). To see this denote the objective functions by f_h and f, respectively . For $x \in \mathcal{C}$ we can choose the constant sequence given by $x_h = x$ to satisfy the second condition and if $(x_h)_h$ is a sequence in $\mathcal{C}$ converging to x, then we can write

$$\liminf_{h\to 0} f_h(x_h) \geq \lim_{h\to 0}(f_h(x_h) - f(x_h)) + \liminf_{h\to 0} f(x_h) \geq f(x).$$

Notice that lower semi continuity of f is enough. Since $\mathcal{C}$ is compact in all of the approaches we derive one of the main result:

Corollary 27. For $h \to 0$ every sequence of optimizers $(I_h)_h$ of the MI, CMI resp. DCMI approach, obtained with the CEM and electrodes size h, has a subsequence that converges to a minimizer of the respective approach used together with the PEM. In the case of DCMI the sequence itself converges.

For the DCMI we can further strengthen this and obtain convergence rates:

Theorem 28. Let $I_h \in \mathbb{R}^L$ be the optimizer for the CEM-DCMI approach with electrodes of size h. Further let I be the optimizer of the PEM-DCMI approach. Then there exists $h_0 > 0$ and $C > 0$ such that for all $h \in (0, h_0)$ it holds

$$\|I_h - I\|_2 \leq Ch^2.$$

Proof. We denote the forward operator for the CEM by A_h and for the PEM by A_0. We will use the subscript 0 for all vectors and functions corresponding to the PEM. We first define the operator $P : \mathbb{R}^L \to \mathbb{R}^L_\diamond$ by

$$(x_1, \ldots, x_L) \mapsto \Big(x_1, \ldots, x_{L-1}, -\sum_{i=1}^{L-1} x_i\Big).$$

Obviously P is the identity on $\mathbb{R}^L_\diamond$. Further note $\mathcal{C} \subset \mathbb{R}^L_\diamond$. Let e_i be the ith standard unit vector of $\mathbb{R}^L$. We define $v_h \in \mathbb{R}^L$ by

$$v_h^i = \int_\Omega \langle A_h P e_i, e\rangle \, dx.$$

From (2.8) we see that $\|v_h - v_0\|_2 \leq Ch^2$ holds when h is small enough. The minimizers I_h satisfies

$$0 \leq (v_h + 2\lambda I_h)^T (y - I_h) \quad \forall y \in \mathcal{C}.$$

To see this, first note

$$0 \leq \frac{f_h(I_h + \alpha(y - I_h)) - f_h(I_h)}{\alpha}, \quad \forall 0 < \alpha \leq 1,$$

where we abbreviated the objective function by f_h. The right hand side is equal to

$$\begin{aligned}&\frac{1}{\alpha}\left(v_h^T(I_h + \alpha(y - I_h)) + \lambda\|I_h + \alpha(y - I_h)\|_2^2 - v_h^T I_h - \lambda\|I_h\|_2^2\right)\\ &= v_h^T(y - I_h) + \frac{\lambda}{\alpha}\left(\|I_h + \alpha(y - I_h)\|_2^2 - \|I_h\|_2^2\right).\end{aligned}$$

Taking $\alpha \searrow 0$ yields $0 \leq v_h^T(y - I_h) + 2\lambda I_h^T(y - I_h)$. Therefore we can obtain two inequalities

$$0 \leq (v_0 + 2\lambda I_0)(I_h - I_0) \quad \text{and} \quad 0 \leq (v_h + 2\lambda I_h)(I_0 - I_h).$$

Adding those together yields

$$0 \leq 2\lambda(I_0 - I_h)^T(I_h - I_0) + (I_0 - I_h)^T(v_h - v_0)$$

or equivalent

$$2\lambda\|I_0 - I_h\|_2^2 \leq (I_0 - I_h)^T(v_h - v_0).$$

By the Cauchy-Schwarz inequality we see $(I_0 - I_h)^T(v_h - v_0) \leq \|I_0 - I_h\|_2\|v_h - v_0\|_2$. Hence we conclude that it exists $h_0 > 0$ and $C > 0$ such that

$$\|I_0 - I_h\|_2 \leq \frac{C}{\lambda}h^2 \quad \forall\ 0 < h < h_0.$$

□

2.4. Numerical Evaluations

In this section we will investigate the effects of forward modeling on the optimal tDCS montages. For this purpose, we will use the already known multilayer sphere model and a realistic head model. We focus on the MI, CMI and further on the DCMI with two different penalty parameters $\lambda = 10$ and 20. For the CEM we will uses electrodes with a radius of $10mm$. As done in Khan et al. (2022), we set $C_1 = 2 \cdot 2mA = 4mA$ and $C_2 = 1.5mA$. The Matlab toolbox CVX (Grant and Boyd, 2014, 2008), a package for specifying and solving convex programs, was used to solve the optimization problems numerically. Therein the solver SDPT3 was selected (Tütüncü et al., 2003). We use four different measures in order to specify the goodness of an approach and the corresponding optimizers (Wagner et al., 2016). The desired properties are intensity, focality and directionality. Hence we define the (average) current intensity in the target area (IT) as

$$\frac{1}{|\Omega_t|} \int_{\Omega_t} |AI| \, dx,$$

where Ω_t denotes the target area. To measure the focality we analogously define the (average) current intensity in the non-target area (INT) with the non-target area being the brain without target area. The last criteria, directionality (DIR), can be measured by

$$\frac{1}{|\Omega_t|} \int_{\Omega_t} \langle AI, e \rangle \, dx.$$

It is plausible to assume $\Omega_t = \operatorname{supp} e$. We want to further define a fourth measure, which provides information on how efficient an approach is (PAR) by the proportion of DIR to IT. It measures how parallel the current density is to the desired orientation. The first three measures IT, INT and DIR are measured in mA/m^2 and PAR in percent.
If I is an optimizer for the MI, CMI or DCMI approach, then $-I$ is optimal for the opposite target direction, namely $-e$. Hence for our tests it is not important whether the targets point inward or outward, for example.

2.4.1. Multilayer Sphere Model

First we want to analyze the case of the multilayer sphere model already introduced in section 1.6. This time we use a setup of 70 more or less evenly distributed electrodes. For the CEM electrodes we again assume a radiues of $1cm$. Further we consider three fixed targets, two superficial ones with an radial and tangential orientation and a deeper one (figure 2.2).

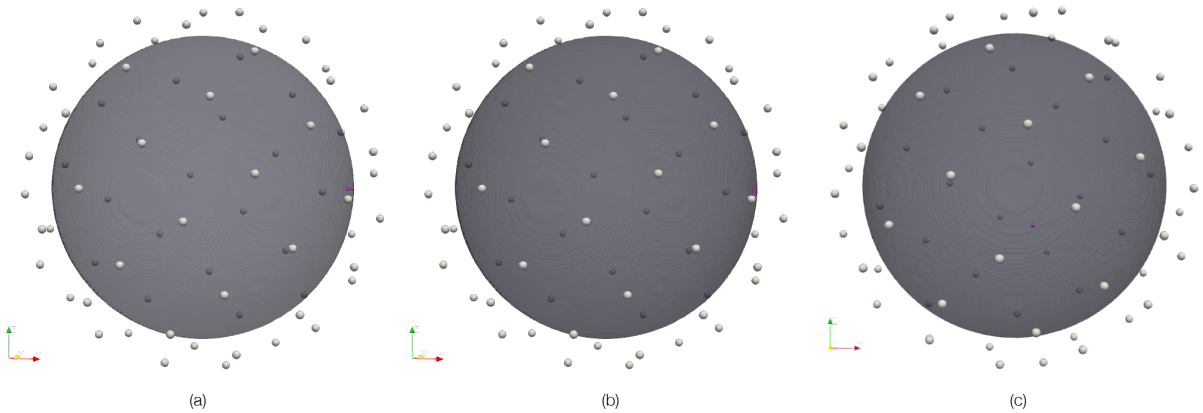

Figure 2.2.: Radial (a), tangential (b) and deep (c) target

	PEM				CEM			
Approach	IT	INT	DIR	PAR	IT	INT	DIR	PAR
MI	141.26	66.85	130.67	92.50	137.64	66.52	128.38	93.28
CMI	127.24	66.01	122.76	96.48	124.79	65.70	120.90	96.89
DCMI $\lambda = 10$	126.48	60.84	122.11	96.55	124.03	60.56	120.26	96.96
DCMI $\lambda = 20$	126.03	58.67	121.75	96.60	123.58	58.40	119.89	97.01

Table 2.1.: Radial target: Measures for different approaches

Radial Target

We start with the radial target. In figure 2.3 the optimal current pattern and the resulting current density on the brain surface is shown for each approach used with the CEM. As already predicted, the MI setup only consists of two electrodes, one directly over the target and the other one located on the opposite side of the head. As we can see in table 2.1 this combination generates the highest intensity in the target area ($137.64 mA/m^2$) compared to the other approaches (with CEM), but is also the least focal one. The generated current density shows the highest magnitudes of all approaches, directly situated under the stimulating electrodes. Continuing with the CMI, we see some slight changes. The optimal montage now consists of four electrodes, two anodal and two cathodal ones. The two main stimulation electrodes are the same as in the MI, but for each electrode, a portion of the current was redistributed to an adjacent electrode. Therefore the magnitudes on the brain surface decrease. However, this results in a loss of intensity ($124.79 mA/m^2$). For the DCMI, the cathodal side remains unchanged, whereas the anodal currents are spread across several electrodes, for $\lambda = 20$ more than for $\lambda = 10$. We clearly see the magnitudes of the current density on the anodal side further decrease. The loss in intensity is small (less than $1.5 mA/m^2$ compared to the CMI), but the intensity in the non target can be decreased by roughly 10 percent. While the MI approach achieves a directionality of $128.38 mA/m^2$, we can only observe values of approximately $120 - 121 mA/m^2$ in the other cases. Surprisingly these approaches show a higher efficiency regarding PAR.
Using the point electrode model instead of the complete electrode model, we can observe a very similar behavior among the different approaches. As the corresponding values of table 2.1 show, the MI can achieves the highest intensity and directionalty but the lowest focality and parallelity. The other three approaches obtain a similar intensity and directionality, with the DCMI $\lambda = 20$ being the most focal one.
Comparing the measures of the CEM with the ones obtained for the PEM, we see that the intensity is stronger for PEM. This was expected as we already saw in the numerical tests of section 1.6, that the current density of the PEM penetrates the head deeper. Interestingly, not all INT values are higher than for CEM. Note that not only the intensity increases, but also the directionality. However, the proportion nearly stays identical. Looking at figure 2.4 we don't see much changes to 2.3, except that the magnitudes on the brain surface are slightly increased. In particular the optimal montages seem to be very similar for both models.

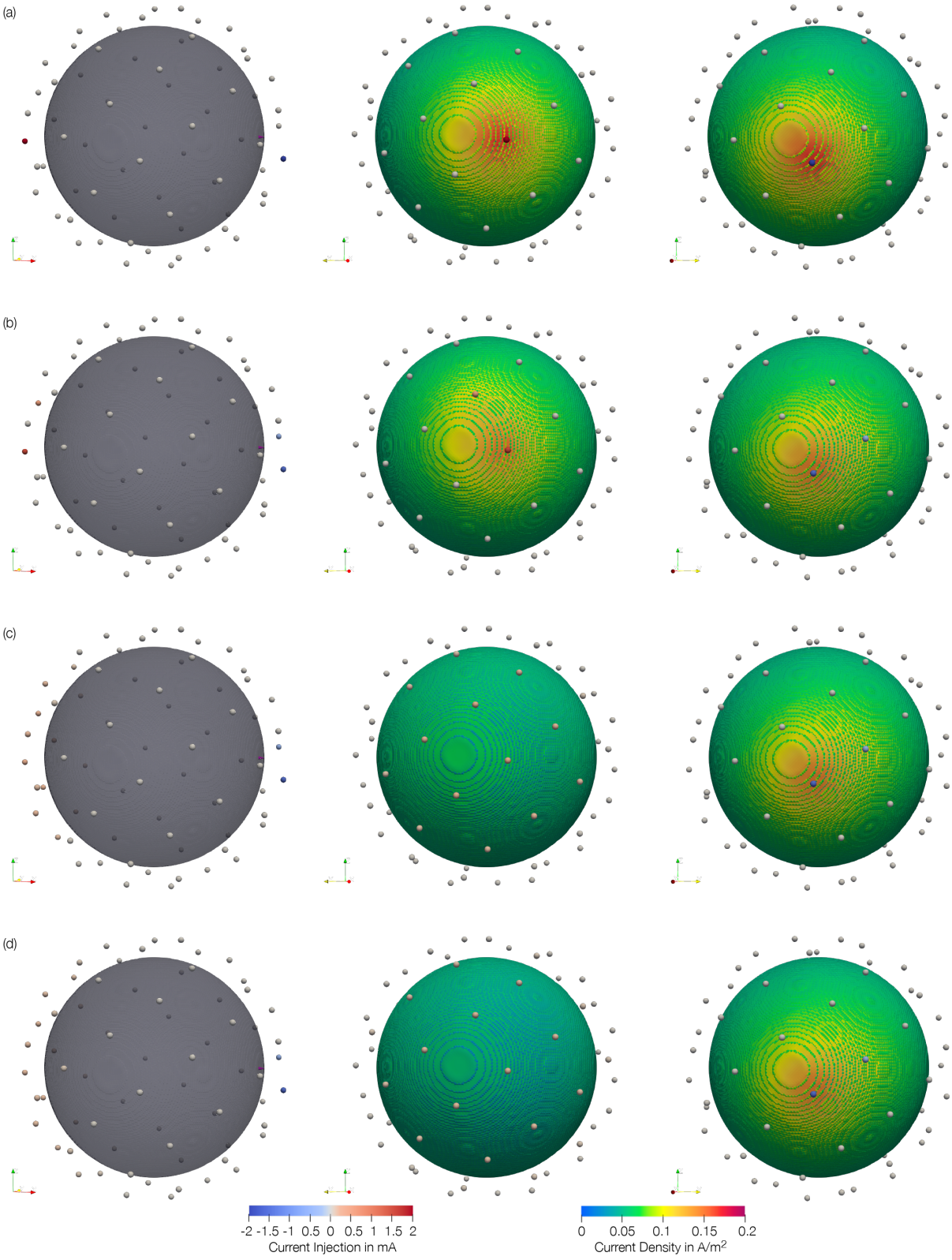

Figure 2.3.: Radial target, CEM: MI (a), CMI (b), DCMI $\lambda = 10$ (c), DCMI $\lambda = 20$ (d), left: montage and target, middle and right: montage and current density on brain surface with view from anodal side (m.) and cathodal side (r.)

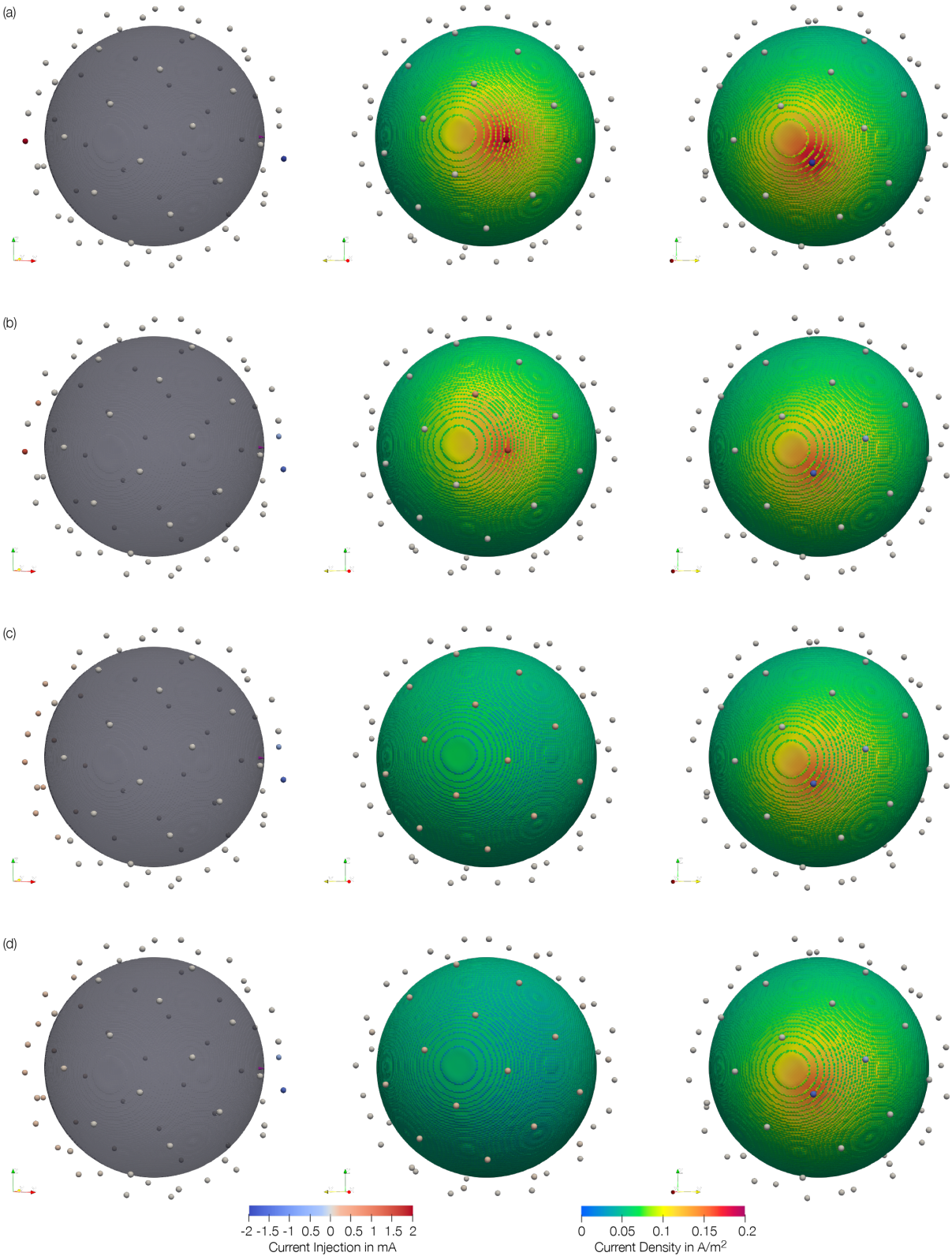

Figure 2.4.: Radial target, PEM: MI (a), CMI (b), DCMI $\lambda = 10$ (c), DCMI $\lambda = 20$ (d), left: montage and target, middle and right: montage and current density on brain surface with view from anodal side (m.) and cathodal side (r.)

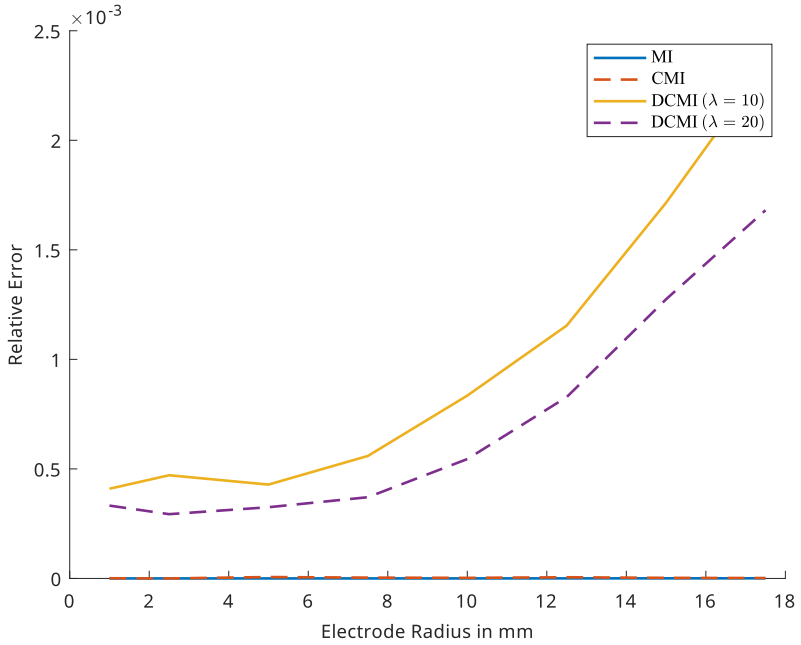

Figure 2.5.: Radial target: Distance between optimizer for PEM and CEM for different electrode sizes

We proved convergence of the optimizers (up to choosing a subsequence) for all approaches in section 2.3. To measure the distance between two montages we define in the style of the relative error

$$\frac{\|I - I_{\text{ref}}\|_2}{\|I_{\text{ref}}\|_2}.$$

When we investigate the behavior of the solutions while decreasing the electrode size, we will always choose the PEM as a reference. Looking at figure 2.5 we can clearly observe the aforementioned convergence. The impression is given that the distance between the optimizers stagnates below a certain size. Note, however, that these values are already very small and accordingly a small scale (0 to 2.5×10^{-3}) was used for the representation, whereas we will use a much larger one (0 to 0.35) for the still following targets. Note the small distance for $10mm$, therefore we could not identify any differences between the montages in figures 2.3 and 2.4.

Tangential Target

We want to continue with the tangential target. The corresponding measures are shown in table 2.2. Again, the MI produces the highest intensities, but the difference to CMI and DCMI $\lambda = 10$ is smaller than in the radial case. It is remarkable that an increase in λ has a much stronger decreasing effect on the intensity and directionality (roughly $-9mA/m^2$) as in the case before. This time the intensity in the non-target area increases when $\lambda \cdot$ increases, even if only slightly. Hence the parameter choice must be well considered. All approaches show high parallelity of nearly 99 to 100 percent. These observations hold for the PEM and CEM equally. The optimizer of the CMI approach stands out. For both electrode models, the intensity of the CMI is similar to DCMI with $\lambda = 10$ and the intensity difference to the MI stays nearly equal. However, for PEM, CMI is the appraoch with the lowest intensity in the non-target area, while for CEM it is the one with the highest. Looking at figure 2.7(b) we can clearly see a difference in the setups. In the PEM, the anodal electrodes are located further above the target, while in the CEM they are located slightly further away.
In the radial case only one or two electrodes active electrodes are positioned directly above the target and the other active ones are located on the opposite side, where their number is

Approach	PEM				CEM			
	IT	INT	DIR	PAR	IT	INT	DIR	PAR
MI	119.43	36.90	118.44	99.17	118.00	36.65	117.00	99.16
CMI	113.50	35.09	112.46	99.08	111.15	40.00	110.56	99.47
DCMI $\lambda = 10$	112.17	36.16	111.41	99.33	110.11	37.91	110.08	99.98
DCMI $\lambda = 20$	104.53	37.37	103.03	98.56	101.58	38.23	100.80	99.23

Table 2.2.: Tangential target: Measures for different approaches

depending on how much regularization is imposed. For tangential targets this changes. Figure 2.7 shows that the anodal electrodes are positioned diagonally above and behind the target, while the cathodal electrodes are located diagonally above and in front. The position and amperage of the two electrodes for the MI are identical for both electrode models. As before, the CMI additionally activates one further electrode in the neighborhood of the MI electrodes, distributing the current. The setup for PEM and CEM differ, as mentioned before. Looking that the DCMI, there are no obvious differences between the montages for PEM and CEM noticeable. An increase in the parameter λ leads to a further distribution of the current to more electrodes on the anodal and on the cathodal side, in contrast to the radial target. As in every simulation so far, the PEM generates higher magnitudes on the brain surface than the CEM does.
When decreasing the size of the electrodes, the optimizers for all approaches seem to converge. The jump for the CMI approach from 7.5 to 10mm strikes out (figure 2.6). At this point the optimal current pattern changes from the one seen in figure 2.7(b) for the CEM to the current pattern shown for the PEM. Between these sizes, the levelsets of the objective functions change enough, such that the optimizer jumps from one vertex to another. This happens so abrupt, because the set of extreme points for the feasible domain of the CMI is always discrete.

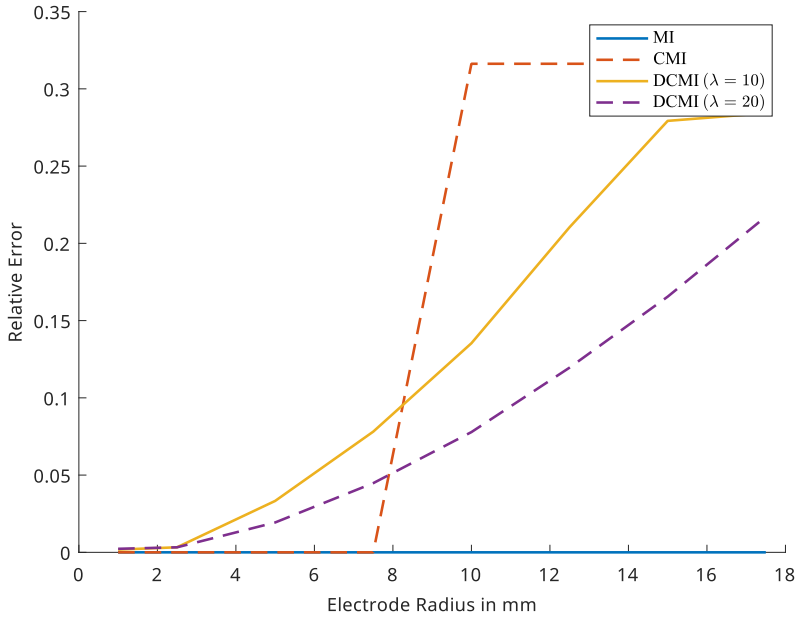

Figure 2.6.: Tangential target: Distance between optimizer for PEM and CEM for different electrode sizes

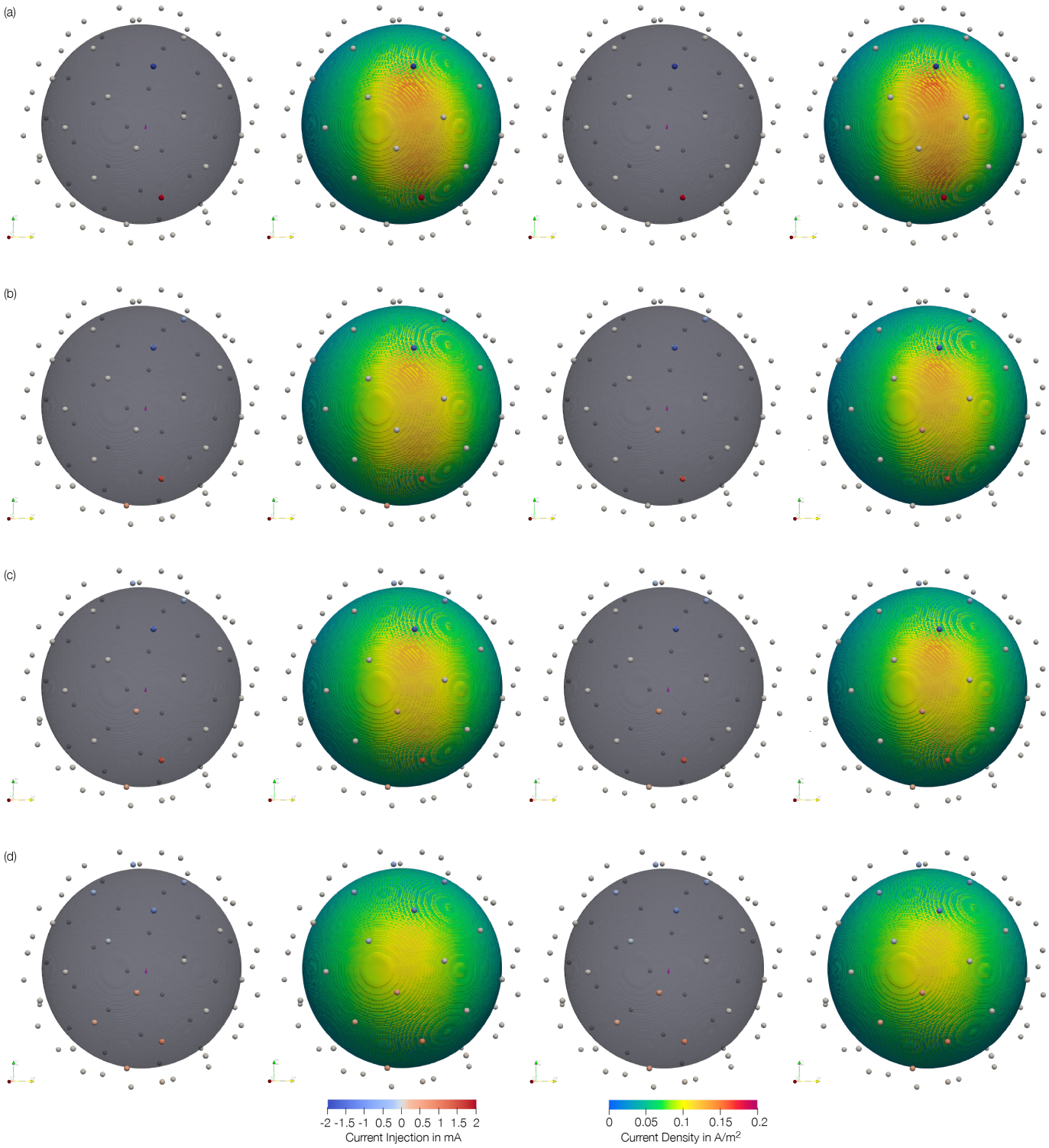

Figure 2.7.: Tangential target, CEM (1.-2. column) & PEM (3.-4. col.): MI (a), CMI (b), DCMI $\lambda = 10$ (c), DCMI $\lambda = 20$ (d), 1.&3. col.: montage and target, 2.&4. col.: montage and current density on brain surface

Deep Target

We just want to briefly discuss the situation of a deep target. The position of the anodal and cathodal electrodes corresponds to those of the radial case. But if additional constraints of the CMI and DCMI are imposed resp. strengthened, then on both sides the current is distributed across multiple electrodes, similar to the case of a tangential target. This can be seen in figure 2.8. Note that the current patterns for PEM and CEM are nearly identical, therefore only the PEM case is shown. Table 2.3 shows that stronger constraints lower the achieved intensity in the target area, but also the intensity in the non-target area. It is remarkable, that in all cases very high PAR values close to 100 percent are achieved. Even though the PEM can generate higher intensities, the differences for the deep target are smaller than in the superficial cases. This fits to the result from the previous chapter, that the differences in the potential and current density don't reach deep. When decreasing the size of the electrodes, the optimizers of all approaches converge. Similar to before, there occurs a jump in the case of CMI.

	PEM				CEM			
Approach	IT	INT	DIR	PAR	IT	INT	DIR	PAR
MI	70.06	64.65	69.76	99.56	69.73	64.33	69.42	99.57
CMI	68.92	61.59	68.86	99.91	68.57	61.29	68.51	99.91
DCMI $\lambda = 10$	65.04	59.20	65.03	99.99	64.70	58.96	64.70	99.99
DCMI $\lambda = 20$	60.80	56.06	60.79	99.97	60.46	55.81	60.44	99.97

Table 2.3.: Deep target: Measures for different approaches

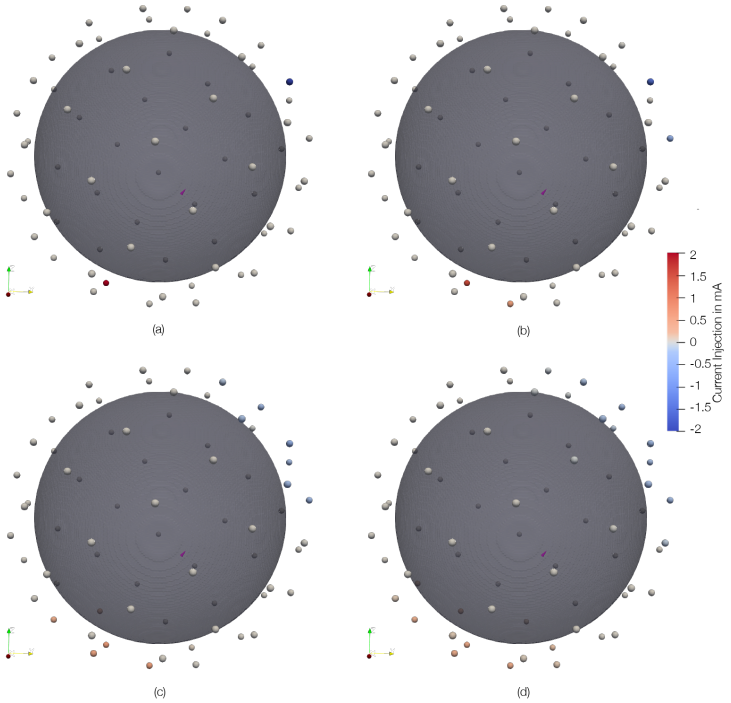

Figure 2.8.: Deep target, PEM montages: MI (a), CMI (b), DCMI $\lambda = 10$ (c), DCMI $\lambda = 20$ (d)

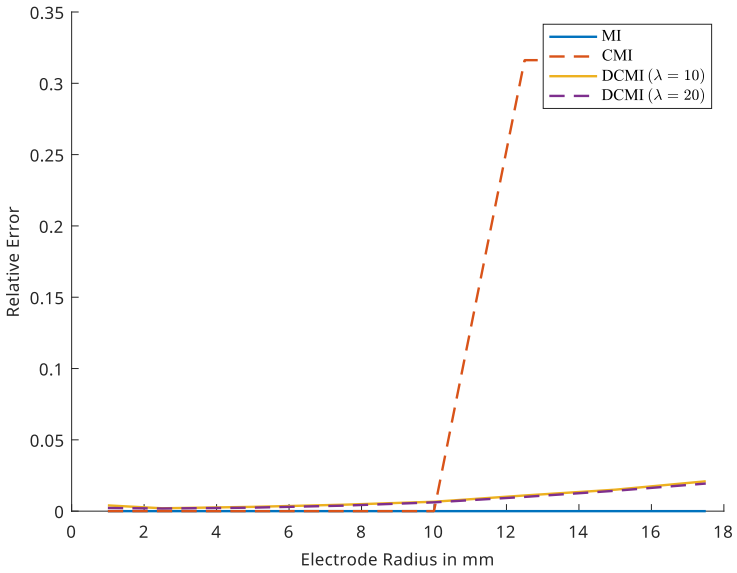

Figure 2.9.: Deep target: Distance between optimizer for PEM and CEM for different electrode sizes

PEM-optimal current pattern used with CEM

So far we used the point electrode model as if it would be applicable in practice, but this clearly isn't the case. Our finite element formulation for the PEM is easier to solve than for the CEM. Therefore, it is conceivable to use the PEM only to simplify the calculations, even though one uses electrodes of $1cm$ radius. We want to investigate, how much the current density obtained by a PEM-optimal current pattern together with the CEM forward model, deviates from the CEM-optimal current density. We will use electrodes with $1cm$ radius again. The resulting measures are shown in table 2.4. Since in the case of the radial target the optimizers for PEM and CEM were very similar, the current densities are (almost) identical and hence the measures are equal as well. For the tangential target, there was clearly a difference for the CMI. Using the PEM optimizer with the CEM forward model, we achieve a nearly identical intensity in the target area, namely 111.40 instead of $111.15 mA/m^2$ and a nearly identical directionality, 110.42 instead of $110.56 mA/m^2$, but the intensity in the non-target area decreses from 40 to $34.87 mA/m^2$. This is possible, because focality has no influence on the maximum intensity formulations presented here. For the deep target the optimal currents don't differ much, hence the corresponding values in table 2.4 are equal to the CEM optimal ones.

Approach	IT	INT	DIR	PAR
MI	137.64	66.52	128.38	93.28
CMI	124.79	65.70	120.90	96.89
DCMI $\lambda = 10$	124.03	60.55	120.25	96.96
DCMI $\lambda = 20$	123.58	58.39	119.89	97.01
MI	118.00	36.65	117.00	99.16
CMI	111.40	34.87	110.42	99.12
DCMI $\lambda = 10$	110.14	35.94	109.45	99.37
DCMI $\lambda = 20$	102.64	37.16	101.23	98.62
MI	69.73	64.33	69.42	99.57
CMI	68.57	61.29	68.51	99.91
DCMI $\lambda = 10$	64.71	58.93	64.71	99.99
DCMI $\lambda = 20$	60.50	55.80	60.48	99.97

Table 2.4.: PEM optimized current patterns used with CEM forward model for radial, tangential, deep targets (top to bottom)

Effect of λ in DCMI Approach

Until now we fixed the parameter λ in the DCMI approach to 10 and 20. We briefly want to discuss and visualize how different choices effect the stimulation results. Figure 2.10 illustrates these effects. The diagram in the lower right corner shows the number of active electrodes. As expected, the number increases with higher λ. We already analyzed, how the current patterns of CMI and DCMI with $\lambda = 10, 20$ differ. The other three diagrams show how these setups continuously merge into each other with increasing λ. Each line represents the injection current of at least one electrode, meaning that several lines could overlap. In the case of the radial target we can clearly see the asymmetry. The two cathodal electrodes are too important for a high intensity, thus λ will only effect these for very high values. Otherwise it will only spread the current on the anodal side as much as possible. In strong contrast, the figure for the tangential target is much more symmetric, meaning that currents on anodal and cathodal side will be spread equally. Starting with the CMI, we can see that the two electrodes, which are already active in the MI, maintain their amperage for quite a long time, whereas the amperage of the other two electrodes decreases for much lower values of λ. In the case of the deep target, it seems as there are no electrodes of such special importance, because the individual amperages rapidly decrease at the beginning.

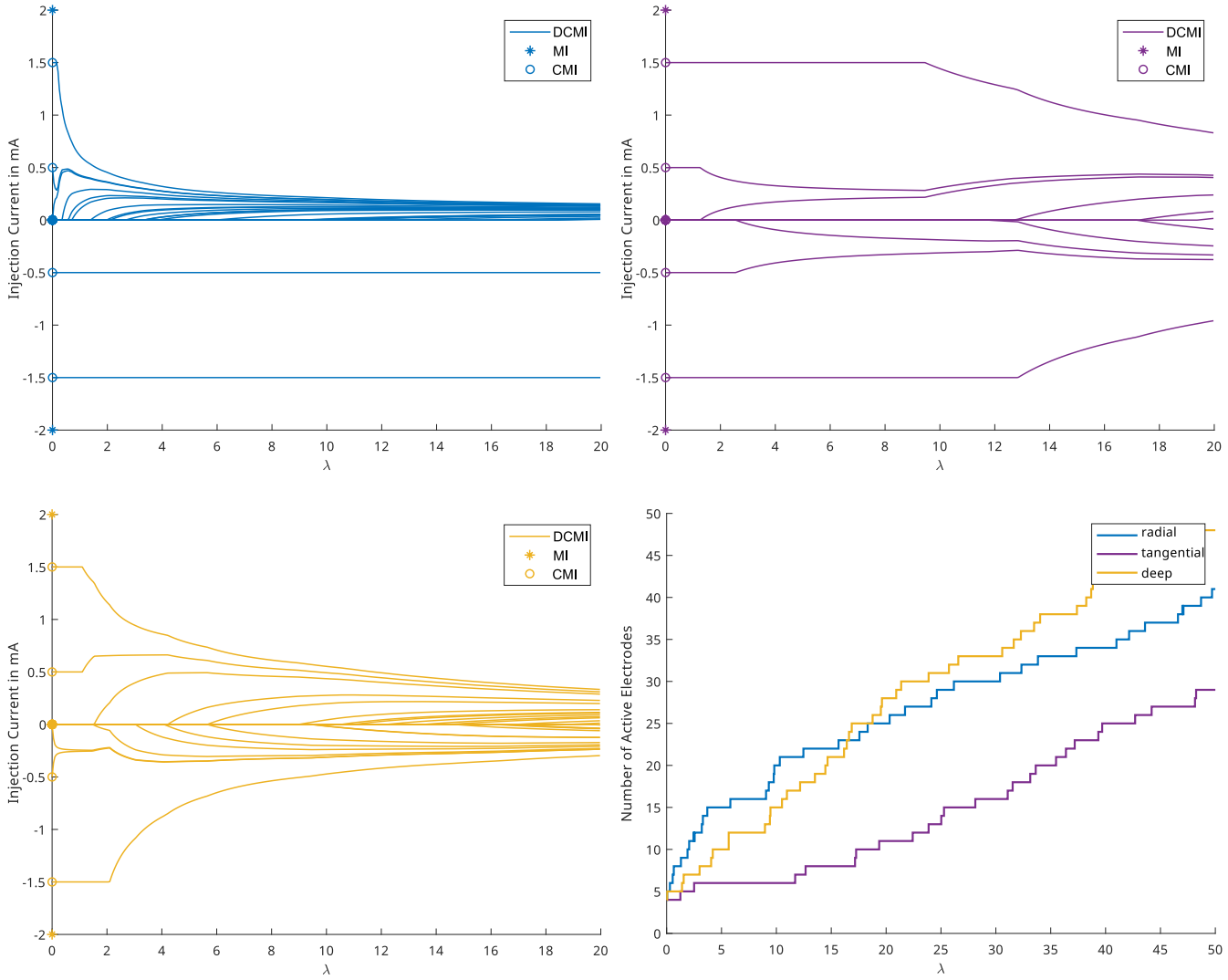

Figure 2.10.: Individual amperage of electrodes for radial (upper left), tangential (upper right) and deep (lower left) targets and number of active electrodes (lower right)

We already saw that an increase in λ has an unambiguous effect on the intensity in the non-target area. This becomes obvious in figure 2.11. For the radial and deep target an increase mainly reduced the INT. The same is true for the tangential target and small values of λ, but at some point the INT increases and becomes worse than for the CMI. It seems like an increase in λ reduces the intensity in the target area and the directionality for all targets. How fast they decrease clearly depends on the target and it's orientation.

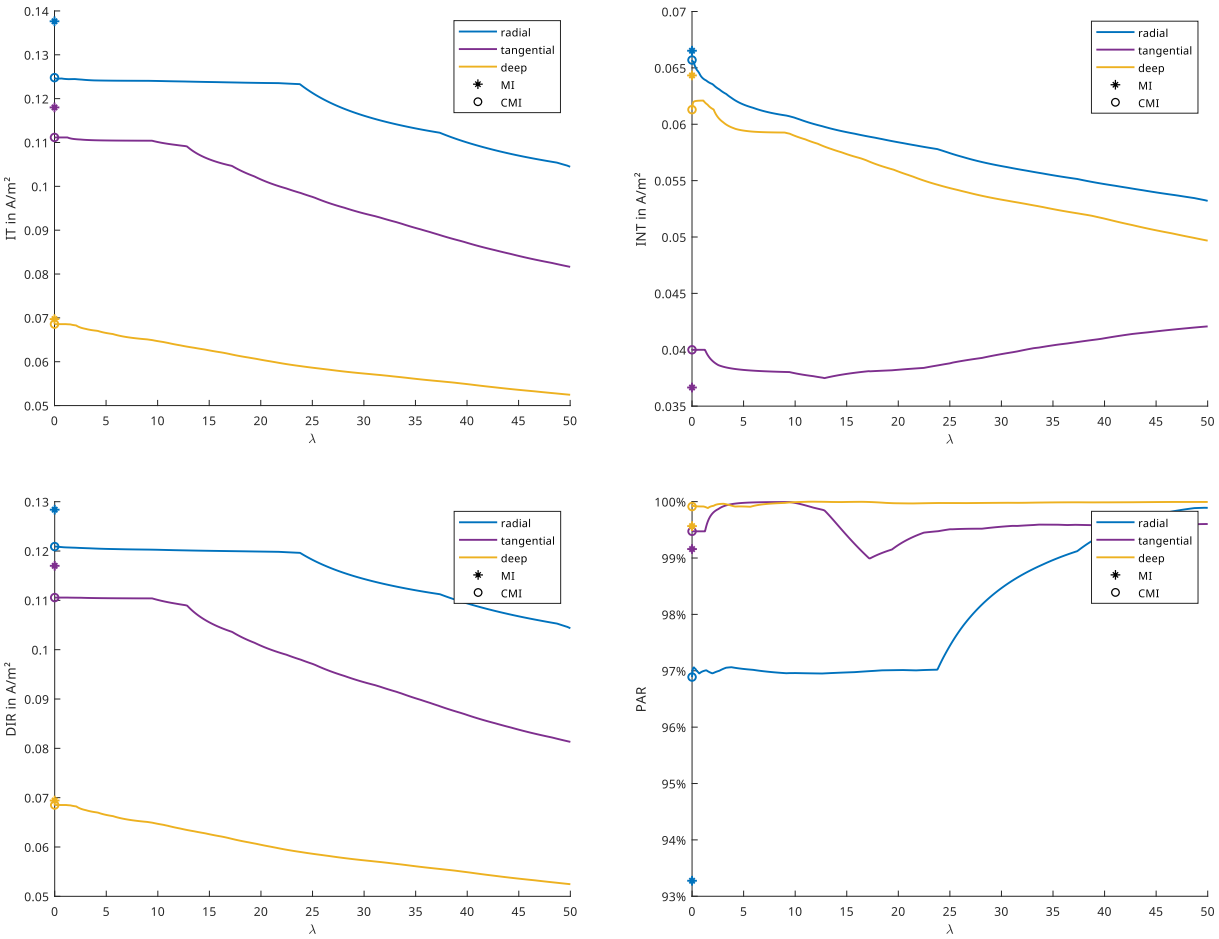

Figure 2.11.: Measures depending on λ: IT (upper left), INT (upper right), DIR (lower left), PAR (lower right)

2.4.2. Realistic Head Model

In this final section, we will consider the problem in the scenario of a more realistic six compartment head model. The levelsets from Piastra et al. (2020) were used to a create surface mesh for each compartment in MATLAB (2020). Based on these meshes a volume mesh with $1mm$ width was generated using Zeffiro Interface (2022). The resulting volume mesh consisted of 4641993 nodes and 22647545 tetrahedrons. This time no smoothing was applied. The different compartments are shown in figure 2.12 and the conductivities can be seen in table 2.5 (Wagner et al., 2013; Dannhauer et al., 2011). A set of 74 electrodes belonging to the head model were taken from Schrader et al. (2021) and are shown in figure 2.13. In this section we will only investigate one target. It is located in the gray matter and can be seen in figure 2.14. As before we will use the MI, CMI and DCMI ($\lambda = 10, 20$) approaches, together with the point electrode model and the complete electrode model.

Tissue	Conductivity (S/m)
Skin	0.43
Skull compacta	0.0064
Skull spongiosa	0.02865
CSF	1.79
Gray Matter	0.33
White Matter	0.14

Table 2.5.: Six compartment head model

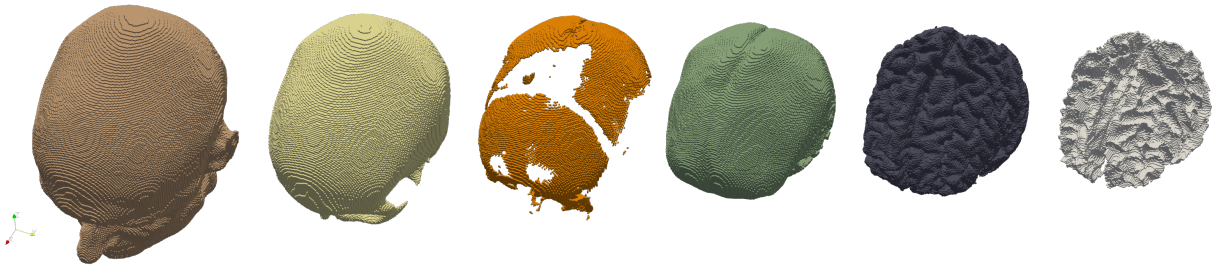

Figure 2.12.: Compartments of head model: Skin, skull compacta & spongiosa, CSF, gray & white matter (left to right)

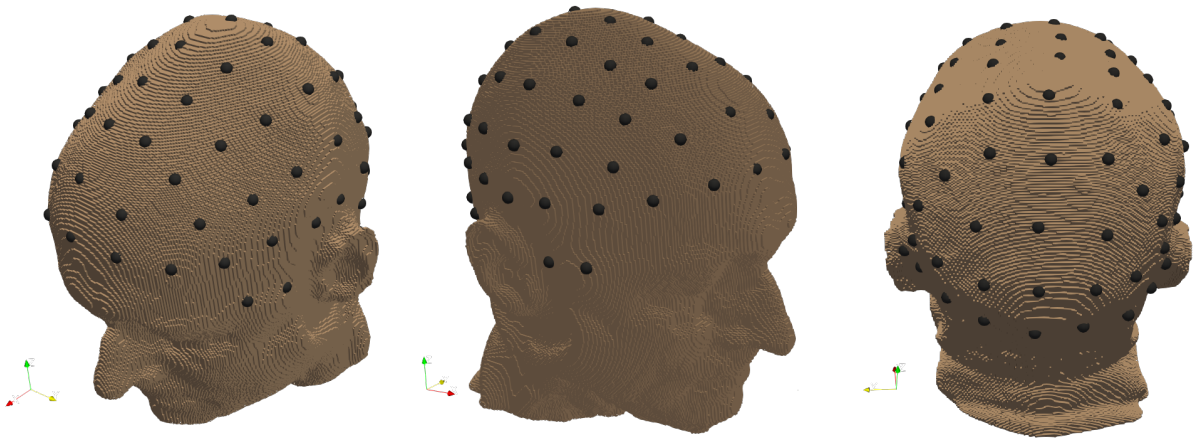

Figure 2.13.: Electrode positions

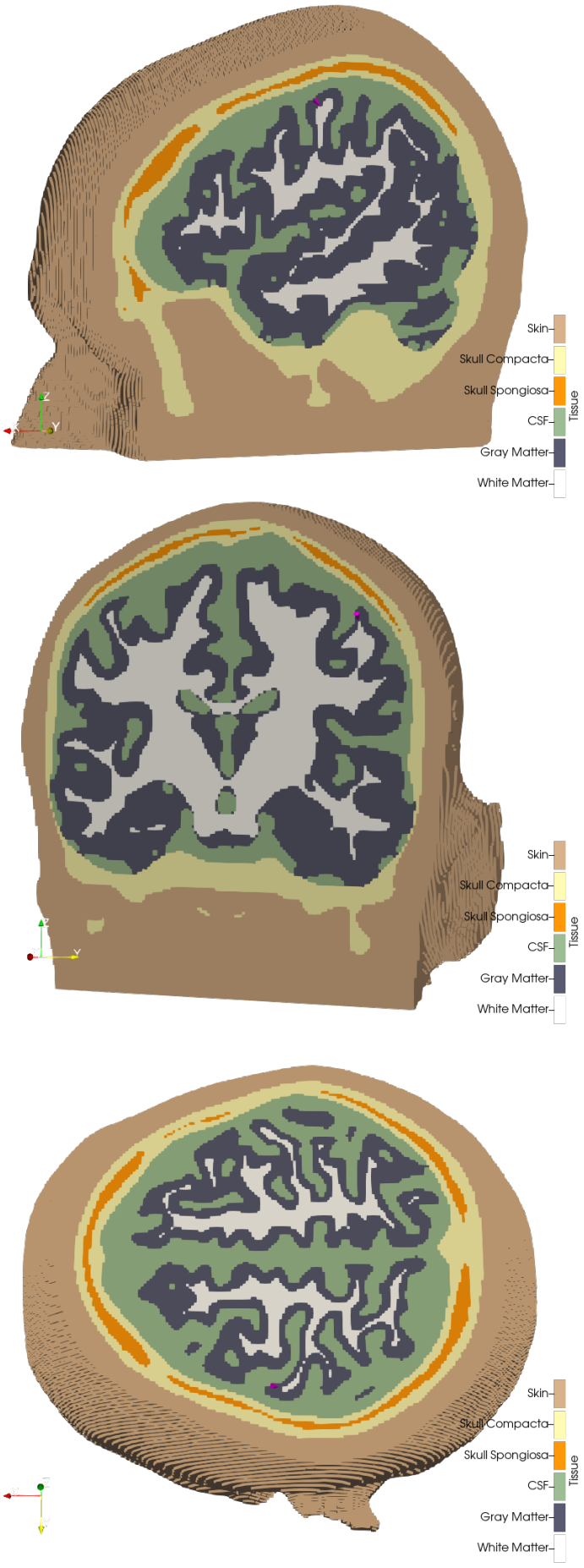

Figure 2.14.: Target location and orientation

	PEM				CEM			
Approach	IT	INT	DIR	PAR	IT	INT	DIR	PAR
MI	83.23	27.00	78.45	94.26	110.54	38.00	72.65	65.72
CMI	80.83	31.81	76.98	95.24	92.73	36.72	72.35	78.02
DCMI $\lambda = 10$	79.55	33.01	74.36	93.48	80.16	34.53	69.55	86.76
DCMI $\lambda = 20$	79.63	37.21	69.35	87.09	79.45	38.37	64.87	81.64

Table 2.6.: Measures for realistic head model

In figure 2.15 the optimal current patterns are shown. For the realistic head model, the differences between PEM and CEM are more obvious than for the multilayer sphere model. Looking at the MI approach, we see that the anodal electrodes are arranged differently. This is in contrast to the multilayer sphere model, where the optimizers of the MI were always identical. In the optimal setup of the PEM, the anodal electrode is located closer over the target. Similar to the sphere model, the CMI emerges from the MI and redistributes part of the current to a neighboring electrode. Interestingly, the anodal electrodes are interchanged in the optimal current pattern of PEM and CEM. Using point electrodes, the stronger one is located closer to the target, whereas for the CEM it is the opposite. The differences between PEM and CEM are smaller for the DCMI approaches, but still noticeable. For both values of λ the anodal electrodes are more concentrated over the target in the case of PEM. Table 2.6 shows the measures for all approaches. Surprisingly, the PEM produces much lower intensities than the CEM in the MI and CMI approaches. Nevertheless, it achieves a higher directionality. Looking at the proportions, we see that the current density in the target area is much more parallel to the target orientation in the PEM than in the CEM. This can also be seen from the figures in appendix A.2. They show the current density near the target in two different cross sections. Considering the DCMI, the intensities in the target areas are identical for CEM and PEM. But for the later model the directionality is larger. Overall the PEM is able to archive higher directionality with less or equal intensity in the target area and furthermore with less intensity in the non-target area.
Table 2.7 shows the measures obtained by using the PEM-optimal current pattern with the CEM forward model. Surprisingly, the achieved directionality for MI and CMI are nearly identical to the optimal values (of the CEM), but with far lower intensity in the target area, non-target area and higher parallelity. In the case of DCMI the diractionality of this hybrid approach is even higher than for the CEM. However, since the values obtained exclusively with CEM are optimal, the 2-norm of the PEM optimizers must be lower to compensate for this.

Approach	IT	INT	DIR	PAR
MI	76.87	26.74	72.61	94.46
CMI	76.33	31.46	72.33	94.76
DCMI $\lambda = 10$	76.11	32.67	70.44	92.55
DCMI $\lambda = 20$	77.33	36.92	66.46	85.95

Table 2.7.: PEM optimized current patterns used with CEM forward model

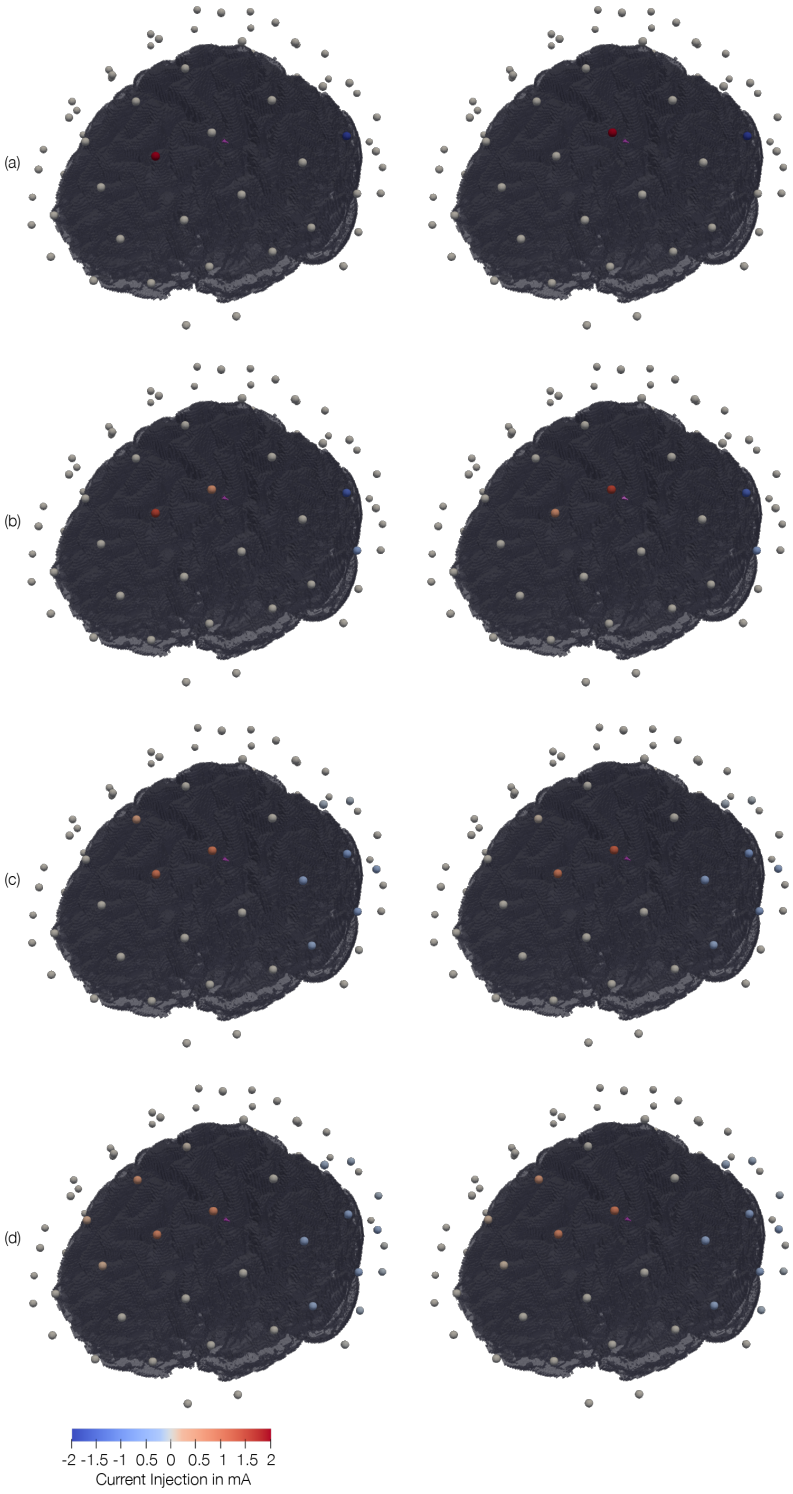

Figure 2.15.: Optimal current pattern for MI (a), CMI (b), DCMI $\lambda = 10$ (c), DCMI $\lambda = 20$ with CEM (l.) and PEM (r.)

As a last result of this section, we want to consider the behavior of the optimal current patterns when we shrink the electrode size. Looking at figure 2.16, we see that all approaches seem to convergence. This time both MI and CMI show a sudden jump. From 10 to 7.5mm the optimal current pattern change to the ones of the PEM. Hence for the CMI the currents of the two anodal electrodes switch and with the MI approach the active anodal electrode moves from its location in 2.15(a) to the position of the anodal electrode in the PEM-optimal current pattern.

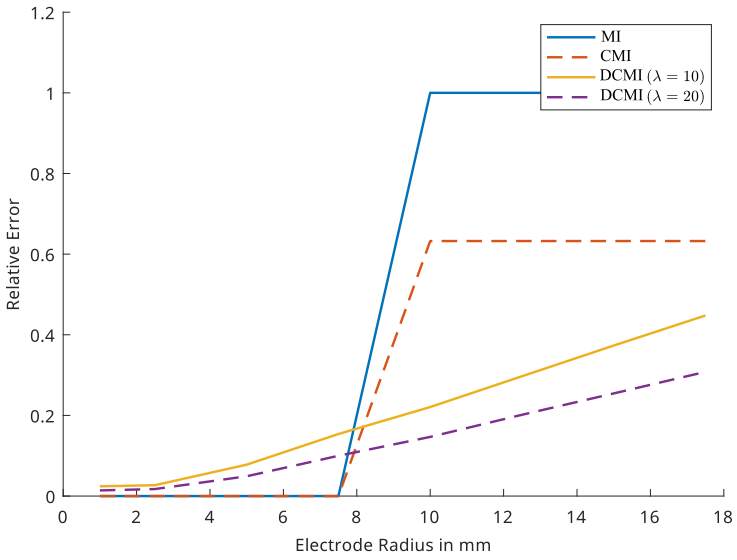

Figure 2.16.: Realistic head model: Distance between optimizer for PEM and CEM for different electrode sizes

So far we assumed fixed positions for the electrodes, e.g. due to the usage of electrode caps. In practice one might not have as many stimulation electrodes as there are positions in the cap, e.g K positions but only $L < K$ electrodes. A heuristic approach could be to first optimize with all positions as degrees of freedom, then select the most important ones (probably based on their current strength) and perform the optimization with only these positions. And indeed, consider the PEM and assume that $x_1, \dots, x_K$ are electrode positions. We denote the initial problem by (P). If $I \in \mathbb{R}^K_\diamond$ is an optimizer with $I_l = 0$, then we can remove the electrode x_l from the PEM boundary value problem and the solution won't change. Denote the resulting current pattern by $\tilde{I} \in \mathbb{R}^{K-1}_\diamond$. Considering the objective functions used in this thesis, we see that $\tilde{I}$ achieves the same optimal value as I for (P). Consequently, I remains optimal if we add the condition $\#\{I_j \neq 0\} \leq K-1$ to the initial problem (P) . Hence, if a solution I for the PEM and MI, CMI or DCMI approach only has L non-zero components, then this current pattern is also optimal for (P) with the additional constraint $\#\{I_j \neq 0\} \leq L$. Further one does not even have to reoptimize with these positions, as the optimizer will be the same.
For the complete electrode model this isn't the case, as inactive electrodes also influence the potential. But we saw in the numerical evaluations of chapter 1 that the influence is very small, especially in the brain. Hence, this is also an plausible heuristic approach for the CEM.

Conclusion

We introduced the point and the complete electrode model and further showed that for both resulting boundary conditions solutions exist. These solutions are only unique up to a constant which represents the fact that the electric potential can only be measured with respect to a reference point. Under assumptions on the regularity of the conductivity and on the deformation of electrodes, we could rigorously prove that for decreasing electrode size, the solutions of the CEM converge towards the PEM solution in the H^1 sense on relative compact subsets. Further it was possible to obtain convergence rates of order two. We focused on a simple multilayer sphere model and tried to derive analytical solutions, so we could compare them to FEM approximations. Therefore we proved that the CEM can be expressed as a series, converging in the H^1 sense. With a sort of Garlerkin method we could approximate this expression. The difference between the semi-analytical solutions for PEM and CEM are mainly located near the electrodes and in the areas underneath. The potential of the PEM achieves higher magnitudes in the underlying brain areas. When comparing these semi-analytical solutions with the FEM solutions, we noticed that the used mesh deviates quite strongly from the actual domain, leading to large errors. Therefore, we could unfortunately not make a detailed comparison of the numerical and semi-analytical solutions. Since the finite element solutions of both models are obtained from the identical mesh, they are still comparable. Nevertheless, the difference in the brain compartment between PEM and CEM behaves similar to the analytical case. For the numerical solutions, the current density was analyzed in addition. Again the point electrode model generates higher magnitudes in the brain areas underneath the electrodes.
In the second part of the thesis we introduced three different optimization approaches which primarily focus on the directional intensity in the target area. These are the MI, CMI and DCMI approach. We proved existence of optimizers for all of them and further gave an alternative formulation of the DCMI. With the help of the convergence results from the first chapter, it was possible to show that every sequence of optimizers for the CEM with decreasing electrode sizes, has a subsequence converging to an optimizer of the PEM. Since optimizers of the DCMI are unique, the sequence itself converges and moreover we could derive convergence rates of order two. This result was also evident in the numerical evaluations with the multilayer sphere model and the realistic head model. We used three targets (radial, tangetial, deep) for the sphere model and one for the head model in order to illustrate the effects of PEM and CEM. In case of the sphere model, the effects were rather small. Differences in the current density mainly arise directly from the fact that the PEM generates higher magnitudes underneath the electrode, but not from strongly differing optimal current patterns. This becomes especially clear when using the PEM optimal montage with the CEM forward model, only in one case there is noticeable difference but this only affects the intensity in the non-target area. For the complex head model, the results changed. The PEM and CEM montages differ much more significant. In the case of the PEM, the anodal electrodes are placed closer to the target. Since the PEM current density can better penetrate the head, it can achieve high directionality. In contrast, the electrodes in the CEM are placed slightly further away in order to still reach the target. Therfore the directionality worsens. Interestingly, when using the PEM-optimized current pattern with the CEM, one can achieve a directionality close to the optimal value, but with lower intensity in the target and non-target area.
In summary, for small electrodes, no significant effect of the electrode modeling on the optimal montages could be seen. This suggests that the simpler point electrode model is a reasonable alternative for the application. For larger ones, this does not hold in general.

A. Appendix

A.1. Supplementary Material for the Analytic Solution of the CEM

The antiderivatives are given by:
$m < 0, s < 0$

$$\int \sin(|m|\varphi)\sin(|s|\varphi) = \frac{1}{2}\begin{cases} \frac{1}{|m|-|s|}\sin((|m|-|s|)\varphi) - \frac{1}{|m|+|s|}\sin((|m|+|s|)\varphi), & \text{if } m \neq s \\ \varphi - \frac{1}{2|m|}\sin(2|m|\varphi), & \text{if } m = s \end{cases}$$

$m = 0, s < 0$

$$\int \sin(|s|\varphi) = -\frac{1}{|s|}\cos(|s|\varphi)$$

$m > 0, s < 0$:

$$\int \cos(m\varphi)\sin(|s|\varphi) = \frac{1}{2}\begin{cases} \frac{1}{m-|s|}\cos((m-|s|)\varphi) - \frac{1}{m+|s|}\cos((m+|s|)\varphi), & \text{if } m \neq s \\ -\frac{1}{2m}\cos(2m\varphi), & \text{if } m = s \end{cases}$$

$m = 0, s = 0$:

$$\int 1 = \varphi$$

$m > 0, s = 0$:

$$\int \cos(m\varphi) = \frac{1}{m}\sin(m\varphi)$$

$m > 0, s > 0$:

$$\int \cos(m\varphi)\cos(s\varphi) = \frac{1}{2}\begin{cases} \frac{1}{m-s}\sin((m-s)\varphi) + \frac{1}{m+s}\sin((m+s)\varphi), & \text{if } m \neq s \\ \varphi + \frac{1}{2m}\sin(2m\varphi), & \text{if } m = s \end{cases}$$

For the other cases one can interchange s and m.

A.2. Supplementary Figures for the Realistic Head Model

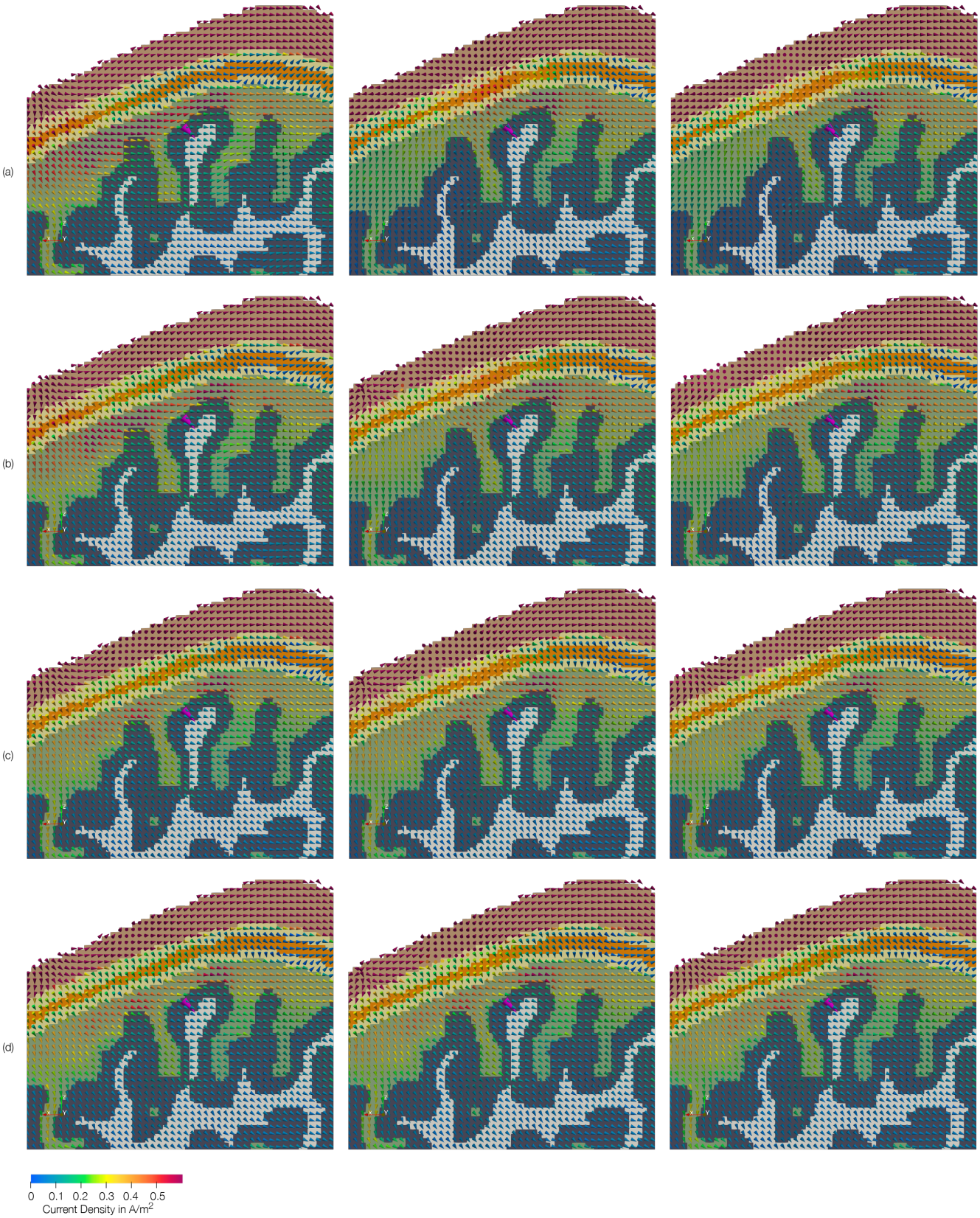

Figure A.1.: Realistic head model: Current density near target (side view): MI (a), CMI (b), DCMI $\lambda = 10$ (c), DCMI $\lambda = 20$ (d), left: CEM , middle: PEM, right: PEM-optimal pattern in CEM

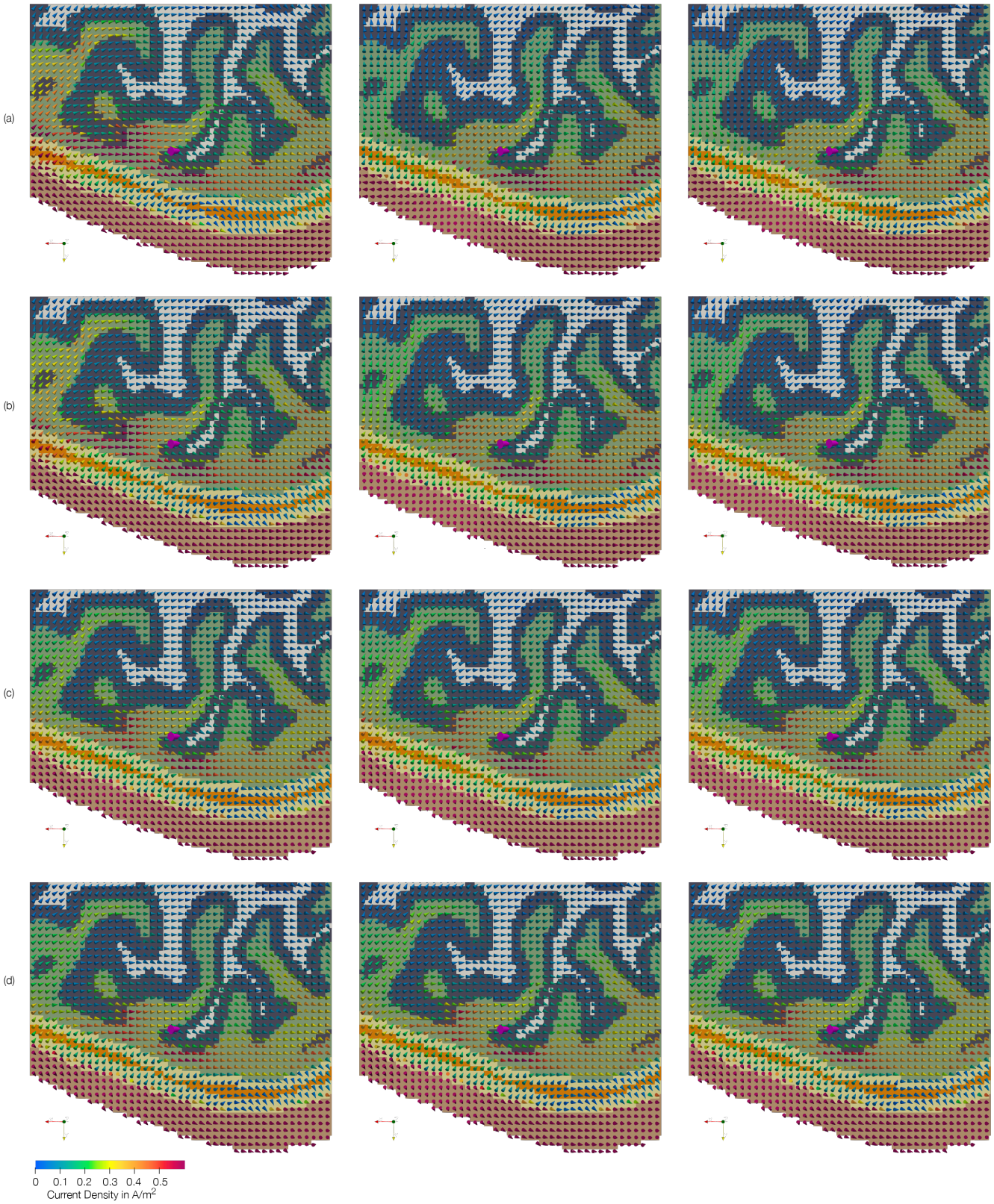

Figure A.2.: Realistic head model: Current density near target (top view): MI (a), CMI (b), DCMI $\lambda = 10$ (c), DCMI $\lambda = 20$ (d), left: CEM , middle: PEM, right: PEM-optimal pattern in CEM

List of Figures

List of Tables

Bibliography

Atkinson, K. and Han, W. (2012). Spherical Harmonics and Approximations on the Unit Sphere: An Introduction. Lecture Notes in Mathematics. Springer Berlin Heidelberg, Berlin, Heidelberg, 2012 edition.

Baumann, S. B., Wozny, D. R., Kelly, S. K., and Meno, F. (1997). The electrical conductivity of human cerebrospinal fluid at body temperature. IEEE Transactions on Biomedical Engineering, 44:220–223.

Berard, P. (1986). Spectral Geometry: Direct and Inverse Problems. Lecture Notes in Mathematics. Springer.

Boggio, P. S., Bermpohl, F., Vergara, A. O., Muniz, A. L., Nahas, F. H., Leme, P. B., Rigonatti, S. P., and Fregni, F. (2007). Go-no-go task performance improvement after anodal transcranial dc stimulation of the left dorsolateral prefrontal cortex in major depression. Journal of Affective Disorders, 101(1):91–98.

Boggio, P. S., Ferrucci, R., Rigonatti, S. P., Covre, P., Nitsche, M., Pascual-Leone, A., and Fregni, F. (2006). Effects of transcranial direct current stimulation on working memory in patients with parkinson's disease. Journal of the Neurological Sciences, 249(1):31–38.

Boyd, S. and Vandenberghe, L. (2004). Convex Optimization. Cambridge University Press.

Braess, D. (2013). Finite Elemente: Theorie, schnelle Löser und Anwendungen in der Elastizitätstheorie. Masterclass. Springer Berlin Heidelberg.

Brenner, S. C. and Scott, L. R. (2008). The mathematical theory of finite element methods. Texts in Applied Mathematics. Springer-Verlag New York, 3 edition.

Brøndsted, A. (2012). An Introduction to Convex Polytopes. Graduate Texts in Mathematics. Springer New York.

Cheng, K.-S., Isaacson, D., Newell, J., and Gisser, D. (1989). Electrode models for electric current computed tomography. IEEE Transactions on Biomedical Engineering, 36(9):918–924.

Ciarlet, P. G. (2002). The finite element method for elliptic problems. Classics in applied mathematics 40. Society for Industrial and Applied Mathematics, 2nd edition.

Crabb, M. G. (2017). Convergence study of 2d forward problem of electrical impedance tomography with high-order finite elements. Inverse Problems in Science and Engineering, 25(10):1397–1422.

Creutzfeldt, O. D., Fromm, G. H., and Kapp, H. (1962). Influence of transcortical d-c currents on cortical neuronal activity. Experimental Neurology, 5(6):436–452.

Dannhauer, M., Lanfer, B., Wolters, C., and Knösche, T. (2011). Modeling of the human skull in eeg source analysis. Human brain mapping, 32:1383–99.

Dardé, J. and Staboulis, S. (2016). Electrode modelling: The effect of contact impedance. ESAIM: M2AN, 50(2):415–431.

Dmochowski, J. P., Datta, A., Bikson, M., Su, Y., and Parra, L. C. (2011). Optimized multi-electrode stimulation increases focality and intensity at target. Journal of neural engineering, 8 4:046011.

Drelichman, I. and Durán, R. G. (2018). Improved poincaré inequalities in fractional sobolev spaces. Annales Academiae Scientiarum Fennicae Mathematica.

Erdbrügger, T.-R. (2021). Cutfem forward modeling for geometries with touching surfaces in bioelectromagnetism. Master's thesis, University of Münster.

Fernández-Corazza, M., Turovets, S., and Muravchik, C. H. (2020). Unification of optimal targeting methods in transcranial electrical stimulation. NeuroImage, 209:116403.

Ferree, T., Eriksen, K., and Tucker, D. (2000). Regional head tissue conductivity estimation for improved eeg analysis. IEEE Transactions on Biomedical Engineering, 47(12):1584–1592.

Ferree, T., Eriksen, K., and Tucker, D. (2001). Correction to "regional head tissue conductivity estimation for improved eeg analysis". IEEE Transactions on Biomedical Engineering, 48(6).

Ferrucci, R., Mameli, F., Guidi, I., Mrakic-Sposta, S., Vergari, M., Marceglia, S., Cogiamanian, F., Barbieri, S., Scarpini, E., and Priori, A. (2008). Transcranial direct current stimulation improves recognition memory in alzheimer disease. Neurology, 71(7):493–498.

Fregni, F., Thome-Souza, S., Nitsche, M. A., Freedman, S. D., Valente, K. D., and Pascual-Leone, A. (2006). A controlled clinical trial of cathodal dc polarization in patients with refractory epilepsy. Epilepsia, 47(2):335–342.

Gellert, W., Küstner, H., Hellwich, M., and Kästner, H. (1975). The VNR Concise Encyclopedia of Mathematics. Springer US, 1 edition.

Gilbarg, D. and Trudinger, N. S. (2001). Elliptic Partial Differential Equations of Second Order. Classics in Mathematics №224. Springer-Verlag Berlin Heidelberg, 2 edition.

Girault, V. and Raviart, P.-A. (1986). Finite Element Methods for Navier-Stokes Equations: Theory and Algorithms (Springer Series in Computational Mathematics). Springer-Verlag.

Grant, M. and Boyd, S. (2008). Graph implementations for nonsmooth convex programs. In Blondel, V., Boyd, S., and Kimura, H., editors, Recent Advances in Learning and Control, Lecture Notes in Control and Information Sciences, pages 95–110. Springer-Verlag Limited.

Grant, M. and Boyd, S. (2014). CVX: Matlab software for disciplined convex programming, version 2.1. `http://cvxr.com/cvx`.

Grisvard (1985). Elliptic Problems in Nonsmooth Domains. Monographs and studies in mathematics 24. Pitman Advanced Pub. Program.

Hanke, M., Harrach, B., and Hyvönen, N. (2011a). Justification of point electrode models in electrical impedance tomography. Mathematical Models and Methods in Applied Sciences, 21:13951413.

Hanke, M., Hyvönen, N., and Reusswig, S. (2011b). Convex backscattering support in electric impedance tomography. Numerische Mathematik, 117(2):373–396.

Hesse, K. and Womersley, R. S. (2012). Numerical integration with polynomial exactness over a spherical cap. Adv. Comput. Math., 36(3):451–483.

Holder, D. S. (2004). Electrical Impedance Tomography: Methods, History and Applications (Series in Medical Physics and Biomedical Engineering). Series in Medical Physics and Biomedical Engineering. Taylor and Francis, 1 edition.

Höltershinken, M. B. (2021). Efficient computation of transfer matrices using the block conjugate gradient method. Master's thesis, University of Münster.

Karabanov, A. N., Saturnino, G. B., Thielscher, A., and Siebner, H. R. (2019). Can transcranial electrical stimulation localize brain function? Frontiers in Psychology, 10.

Khan, A., Antonakakis, M., Vogenauer, N., Haueisen, J., and Wolters, C. H. (2022). Individually optimized multi-channel tdcs for targeting somatosensory cortex. Clinical Neurophysiology, 134:9–26.

Khor, C. and Rodrigo, J. L. (2020). On sharp fronts and almost-sharp fronts for singular sqg.

Kloft, M., Brefeld, U., Sonnenburg, S., and Zien, A. (2011). l_p-norm multiple kernel learning. Journal of Machine Learning Research, 12(26):953–997.

Korn, G. A. and Korn, T. M. (1968). Mathematical handbook for scientists and engineers; definitions, theorems, and formulas for reference and review. McGraw-Hill handbooks. New York, McGraw-Hill, 2d, enl. and rev. ed edition.

Königsberger, K. (2000). Analysis 2. Springer-Lehrbuch. Springer Berlin Heidelberg, 3., überarb. aufl. edition.

Lee, J. M. (2012). Introduction to Smooth Manifolds. Graduate Texts in Mathematics №218. Springer-Verlag New York, 2 edition.

Leoni, G. (2009). A First Course in Sobolev Spaces. Graduate Studies in Mathematics. American Mathematical Society.

Lions, J. L. and Magenes, E. (1972). Non-Homogeneous Boundary Value Problems and Applications: Vol. 1. Grundlehren der mathematischen Wissenschaften №181. Springer-Verlag Berlin Heidelberg, 1 edition.

Lunkenheimer, P. (2021). Comparison of boundary element fast multipole and finite element methods for the solution of the eeg forward problem. Master's thesis, University of Münster.

MATLAB (2020). Version 9.9.0 (R2020b). The MathWorks Inc., Natick, Massachusetts.

Nitsche, M. A. and Paulus, W. (2000). Excitability changes induced in the human motor cortex by weak transcranial direct current stimulation. The Journal of Physiology, 527(3):633–639.

Nolting, W. (2001). Grundkurs Theoretische Physik 3: Elektrodynamik. Springer-Lehrbuch German Edition. Springer, 7. aufl. edition.

Piastra, M. C., Schrader, S., Nüßing, A., Antonakakis, M., Medani, T., Wollbrink, A., Engwer, C., and Wolters, C. H. (2020). The WWU DUNEuro reference data set for combined EEG/MEG source analysis. Zenodo.

Pidcock, M., Kuzuoglu, M., and Leblebicioglu, K. (1995a). Analytic and semi-analytic solutions in electrical impedance tomography: I.two-dimensional problems. Physiological measurement, 16:77–90.

Pidcock, M. K., Kuzuoglu, M., and Leblebicioglu, K. (1995b). Analytic and semi-analytic solutions in electrical impedance tomography. II. three-dimensional problems. Physiological Measurement, 16(2):91–110.

Plonsey, R. and Heppner, D. B. (1967). Considerations of quasi-stationarity in electrophysiological systems. The Bulletin of mathematical biophysics, 29 4:657–64.

Purves, D., Augustine, G. J., Fitzpatrick, D., Hall, W. C., Lamantia, A.-S., McNamara, J. O., and Williams, S. M. (2004). Neuroscience. Sinauer Associates, 3rd edition.

Rockafellar, R. T. (1970). Convex Analysis. Princeton Landmarks in Mathematics and Physics, 36. Princeton University Press.

Rudin, W. (1991). Functional Analysis. International series in pure and applied mathematics. McGraw-Hill, 2nd ed edition.

Schrader, S., Westhoff, A., Piastra, M. C., Miinalainen, T., Pursiainen, S., Vorwerk, J., Brinck, H., Wolters, C. H., and Engwer, C. (2021). Duneuro—a software toolbox for forward modeling in bioelectromagnetism. PLOS ONE, 16:1–21.

Shubin, M. (2001). Pseudodifferential Operators and Spectral Theory. Pseudodifferential Operators and Spectral Theory. Springer Berlin Heidelberg.

Somersalo, E., Cheney, M., and Isaacson, D. (1992). Existence and uniqueness for electrode models for electric current computed tomography. Siam Journal on Applied Mathematics, 52:1023–1040.

Trefethen, L. N. (2008). Is gauss quadrature better than clenshaw–curtis? SIAM Review, 50(1):67–87.

Tütüncü, R. H., chuan Toh, K., and Todd, M. J. (2003). Solving semidefinite-quadratic-linear programs using sdpt3. Mathematical Programming, 95:189–217.

Wagner, S., Burger, M., and Wolters, C. H. (2016). An optimization approach for well-targeted transcranial direct current stimulation. SIAM Journal on Applied Mathematics, 76(6):2154–2174.

Wagner, S., Rampersad, S. M., Aydin, Ü., Vorwerk, J., Oostendorp, T. F., Neuling, T., Herrmann, C. S., Stegeman, D. F., and Wolters, C. H. (2013). Investigation of tDCS volume conduction effects in a highly realistic head model. Journal of Neural Engineering, 11(1):016002.

Wloka, J. (1987). Partial Differential Equations. Cambridge University Press.

Yosida, K. (1995). Functional Analysis. Classics in Mathematics 123. Springer, Berlin, Heidelberg, 6 edition.

Zeffiro Interface (2022). Version January 2022. Mathematics and Statistics, Faculty of Information Technology and Communication Sciences, Tampere University, Tampere, Finland.

Ziemer, W. P. (1989). Weakly Differentiable Functions: Sobolev Spaces and Functions of Bounded Variation. Graduate Texts in Mathematics №120. Springer-Verlag New York, 1 edition.

Declaration of Academic Integrity

I hereby confirm that this thesis on "Sensitivity of Optimization in Transcranial Direct Current Stimulation to Electrode Modeling" is solely my own work and that I have used no sources or aids other than the ones stated. All passages in my thesis for which other sources, including electronic media, have been used, be it direct quotes or content references, have been acknowledged as such and the sources cited.

_____

I agree to have my thesis checked in order to rule out potential similarities with other works and to have my thesis stored in a database for this purpose.

_____